THE ORGANISATION OF CONFINED WATER IN SELF-ASSEMBLED LIPID NANOSTRUCTURES

Gerome Lahiru Vancuylenberg

Submitted in accordance with the requirements for the degree of

Doctor of Philosophy

The University of Leeds

School of Food Science and Nutrition

March 2024

The candidate confirms that the work submitted is his own, except where work has formed part of jointly authored publications. The candidate confirms that appropriate credit has been given within the thesis where reference has been made to the work of others. Details of the jointly-authored publications and the contributions of each author are outlined on the pages iii and iv.

Details of Jointly Authored Publications and Corresponding Thesis Chapters

Chapter 3

Vancuylenberg, G., Sadeghpour, A., Tyler, A.I.I. and Rappolt, M. Planar confined water organisation in lipid bilayer stacks of phosphatidylcholine and phosphatidyl-ethanolamine. Soft Matter. 2023, 19(27), pp.5179-5192.

Chapter 4

Vancuylenberg, G., Sadeghpour, A., Tyler, A.I.I. and Rappolt, M. From angular to round: in depth interfacial analysis of binary phosphatidylethanolamine mixtures in the inverse hexagonal phase. Soft Matter. 2023, 19, 8519–8530.

Chapter 5

Vancuylenberg, G., Sadeghpour, A., Tyler, A.I.I. and Rappolt, M. Membrane Dynamics and Confined Water Layer Classification in the Presence of Ion-Rich Solutions. Manuscript prepared for submission.

Details of Authorship Contributions

Planar confined water organisation in lipid bilayer stacks of phosphatidylcholine and phosphatidylethanolamine.

Gerome Vancuylenberg designed the experimental work with the support of his supervisors Michael Rappolt and Arwen Tyler. Gerome conducted the experimental work. Gerome analysed all data, while Michael Rappolt and Amin Sadeghpour supported Gerome on data analysis strategy. Gerome Vancuylenberg prepared the manuscript, which was commented and revised by all authors and finally published in 2023 in Soft Matter (1).

From angular to round: in depth interfacial analysis of binary phosphatidyl-ethanolamine mixtures in the inverse hexagonal phase.

Gerome Vancuylenberg designed the experimental data analysis strategy with the support of his supervisors Michael Rappolt and Arwen Tyler (note, due to the COVID lockdown situation, the unpublished experimental data set was provided by Michael Rappolt). Gerome further wrote a programme code in MATLAB for the fine-structural analysis of the inverse hexagonal phase. Gerome analysed all data, while Michael Rappolt and Amin Sadeghpour supported Gerome on data analysis strategy. Gerome Vancuylenberg prepared the manuscript, which was commented and revised by all authors and finally published in 2023 in Soft Matter (2).

Membrane dynamics and confined water layer classification in the presence of ion-rich solutions.

Gerome Vancuylenberg designed the experimental work with the support of his supervisors Michael Rappolt and Arwen Tyler. The beamtime at the Diamond Leeds SAXS Facility was carried out by Gerome Vancuylenberg and Michael Rappolt. Paul Wady and Thomas Zinn are acknowledged for their help during the offline synchrotron beamtime and its data processing. Gerome analysed all data, while Michael Rappolt and Amin Sadeghpour supported Gerome on data analysis strategy. Gerome Vancuylenberg prepared the manuscript, which was commented and revised by all authors and the presented manuscript will be submitted for publication.

Conference Contributions and Awards

Poster presentations

Vancuylenberg, G., Sadeghpour, A., Tyler, A.I.I. and Rappolt, July 2022. From angular to round: in depth interfacial analysis of binary phosphatidylethanolamine mixtures in the inverse hexagonal phase. SOFI Showcase, Leeds, United Kingdom (poster).

Vancuylenberg, G., Sadeghpour, A., Tyler, A.I.I and Rappolt, February 2023. Planar confined water organisation in lipid bilayer stacks of phosphatidylcholine and phosphatidylethanolamine. Biophysical Society Annual Meeting, San Diego, United States of America (poster).

Vancuylenberg, G., Sadeghpour, A., Tyler, A.I.I and Rappolt, September 2023. Planar confined water organisation in lipid bilayer stacks of phosphatidylcholine and phosphatidylethanolamine. International Soft Matter, Osaka, Japan (poster).

Oral presentations

Vancuylenberg, G., Sadeghpour, A., Tyler, A.I.I and Rappolt, August 2022. From angular to round: in depth interfacial analysis of binary phosphatidylethanolamine mixtures in the inverse hexagonal phase. Inter CDT, Leeds, United Kingdom.

Vancuylenberg, G., Sadeghpour, A., Tyler, A.I.I and Rappolt, January 2023. Taking a Closer Look into Water Organisation in Planar Lipid Bilayer Stacks of Phosphatidylcholine (PC) and Phosphatidylethanolamine (PE). School of Food Science and Nutrition PGR Conference, Leeds, United Kingdom.

Vancuylenberg, G., Sadeghpour, A., Tyler, A.I.I and Rappolt, May 2023. Planar confined water organisation in lipid bilayer stacks of PCs and PEs . Soft Comp, Ancona, Italy.

Vancuylenberg, G., Sadeghpour, A., Tyler, A.I.I and Rappolt, July 2023. The Wet World of Lipids: Classifying Confined Water in and around the Phospholipid Bilayer. SOFI Showcase, Durham, United Kingdom.

Awards

Beamtime grant for experiments at the Diamond Leeds SAXS Facility: Proposal number SM37052 - Membrane Dynamics and Confined Water Layer Classification in the Presence of Ion-Rich Solutions (2023).

Food Science and Nutrition PGR conference (Jan 2023). First prize for an oral presentation.

“This is… a cruel world. And yet… so beautiful…”

Mikasa Ackerman

Acknowledgements

First and forthrightly, I should like to thank my supervisors: Michael Rappolt and Arwen Tyler. The gratitude I feel towards them goes beyond words. I only want them to know it has been a privilege of the highest rarity to learn from them, a privilege to conduct science with them and a privilege to have known them. A special thank you also goes to our long standing collaborator, Amin Sadeghpour. His patience is worthy itself of an in depth study. Thanks also to my colleague, Yoga Pratama, who first taught me what to *do* with the data.

A gracious thank you is deserved by my family. To my Sister and Brother, who are gifts I am only too lucky to have. To my Mother and Father, who are and always will be, my greatest teachers. I have much to thank them for; My Mother for my brain, and my Father for my industriousness. I am dedicating this thesis in its entirety to all my Grandparents. Their bravery and resolve inspires me always. I am only a result of their fractal planes.

I wish to specially thank all the friends I have made during my PhD. My friends at the SOFI CDT, in particular those residents of *Lichless by the Sea*: Jack, Joe, Dan, Eugénia and Charles. For my friends across campus: Anthony, Mae, James and Oisín. For the friends in my department: Julia, Serena, Fran and Meg. All of them are, in their own ways, truly beautiful human beings.

When I was younger, every summer my Mother would ask if we should plant flowers or trees in the garden that year. She always preferred flowers and I always trees. Trees because, by winter the flowers would die, but if we planted a tree, it may very well outlive us. I think science is a lot like that; planting things that will outlive us. My mother has, to date, now planted several trees. I should like to take a brief moment to acknowledge nature, as all science is merely an attempt to understand. There is a beautiful symmetry to the fact that the blue whale, which is the largest animal on earth, survives by eating plankton, which is one of the smallest. Nature's savage elegance, I feel, is beyond our human comprehension. We are reminded constantly of climate change, pollution of the ocean, industrialised farming of trees and the damage all this does to the environment. We, as humans, are killing nature.

I however believe, that nature will never die and so cannot be killed. The trees, the rivers, the *environment* will live on and *the* humans are the ones who will cease to exist. As such, we only destroy ourselves. It is a testament to our arrogance as a species that we do not consider ourselves to be within the scope of the destruction we cause. Therefore, my last and most sincere acknowledgement is for Mother Nature; to whom all things shall one day return.

Abstract

Phospholipid-based liposomes are abundantly studied in biomembrane research and used in numerous medical and biotechnological applications. When dispersed in water, lipids hydrate to form a variety of complex nanostructures. Despite our knowledge of membrane nanostructure and its mechanical properties under various environmental conditions, there is still a lack of understanding on interfacial lipid-water interactions. In this work, we have investigated the nature of the confined water layer for variety of lipids, focusing on the phosphatidylcholine (PC) phosphatidylethanolamine (PE) species. The majority of the studies are conducted in the fluid lamellar phase of multilamellar vesicles with and without the inclusion of ions dissolved in the water phase. Additionally, a binary lipid mixture in the inverse hexagonal (H_{II}) phase was also investigated. We are proposing a new model for describing three different water regions, which have been characterised, using a combination of Small Angle X-ray Scattering (SAXS) and volumetric data. The three regions concern (i) 'the headgroup water', (ii) 'perturbed water' near the membrane interface and (iii) a core layer of 'free water' (unperturbed water). The behaviour of all three layers is discussed as a function of temperature, influences of chain saturation, headgroup type and as a function of ion concentration, influenced by mono- and divalent ions. Under temperature, the overall water layer and perturbed water layer thickness increase, whilst the free water layer displays the opposite trend for PCs and, remarkably, in PEs the free water layer is completely absent. This behaviour in PEs is different when in the inverse hexagonal phase, where a free water region develops and remains relatively unchanged as the micelle packing frustration is alleviated. Most interestingly, the mechanical behaviour of the inverse hexagonal phase is different orientated towards the corners and flat sides of the Wigner Seitz cell. Understandably, the disorder is relatively enhanced within the hexagon's corners (decompression zones), concurrently with the amount of perturbed waters in this region. The influence of ions onto the lamellar phase water layers is heavily dependent on ion valency and also on a specific ions kosmotropic or chaotropic potential. The trend of the cationic Hofmeister series is reflected in the perturbed water layer, increasing from Mg^{2+}, Na^{+} to K^{+}.

Table of Contents

List of Tables

List of Figures

List of Abbreviations

A_L	Area per lipid
A_P	Area at phosphate group
A_W	Area of water core
B	Compression modulus
Ca^{2+}	Calcium ion
$CaCl_2$	Calcium chloride
CARS	Coherent anti-Stokes Raman
Cl^-	Chloride ion
CPP	Critical packing parameter
d	Lattice repeat distance
d_C	Lipid chain length
D_H	Headgroup thickness
d_{HH}	Head-to-head distance
D_{H1}	Partial headgroup thickness
D_{H2}	Gibbs dividing partial headgroup thickness
d_{LZ}	Luzzati bilayer thickness
DMPC	1,2-dimyristoyl-*sn*-glycerol-3-phosphocholine
DMPE	1,2-dimyristoyl-*sn*-glycero-3-phosphoethanolamine
DOPC	1,2-dioleoyl-*sn*-glycero-3-phosphocholine
DPPC	dipalmitoylphosphatidylcholine
DPPE	1,2- dipalmitoyl-sn-glycero-3-phosphoethanolamine
DSC	Differential scanning calorimetry
d_W	Interstitial water thickness

dw^f	Free water layer thickness
dw^σ	Perturbed water layer thickness
EDP	Electron density profile
Egg-PC	L-α-phosphatidylcholine
η	Caillé fluctuation parameter
FWHM	Full width at half maxima
H-Bond	Hydrogen bond
H_{II}	Inverse hexagonal phase
K^+	Potassium ion
KCl	Potassium chloride
K_C	Bending modulus
K_A	Area compression modulus
L_α	Lipid fluid phase
l_{ave}	Average lipid length
L_d	Liquid disordered phase
l_{max}	Maximum lipid length
l_{min}	Minimum lipid length
L_o	Liquid ordered phase
M	Molar
MCT	Modified Caillé theory
MD	Molecular dynamics
Mg^{2+}	Magnesium ion
$MgCl_2$	Magnesium chloride
MLV	Multi lamellar vesicle

mol%	Molar concentration/fraction
N	Nitrogen
Na^+	Sodium ion
NaCl	Sodium chloride
n_L	Number of lipids
NMR	Nuclear magnetic resonance
n_W	Number of water molecules
n_W^f	Number of free water molecules
n_W^H	Number of headgroup water molecules
n_W^σ	Number of perturbed water molecules
P	Phosphate
PC	Phosphatidylcholine
PE	Phosphatidylethanolamine
POPE	1-palmitoyl-2-oleoyl-sn-glycero-3-phosphoethanolamine
PT	Paracrystalline theory
R_{max}	Maximum water core radius
R_{min}	Minimum water core radius
R_P	Radius to phosphate group from water core centre
ρ	Density
ρ_{max}	Density maximum
ρ_{min}	Density minimum
SAXD	Small-angle X-ray diffraction
SAXS	Small-angle X-ray scattering
σ	Fluctuation distance

T_H	Hexagonal phase transition temperature
T_m	Main transition temperature
TR–FTIR	Total reflection Fourier transform infrared
ULV	Uni lamellar vesicle
V_{ave}	Averaged lipid volume
VdW	Van der Waals
V_H	Lipid headgroup volume
V_L	Volume per lipid
V_W	Water volume per lipid
vol%	Volume fraction
WAXS	Wide-angle X-ray scattering
wt%	Weight concentration/fraction

Chapter 1. Introduction and Research Question

1.1 Oil and Water – The Structure of Life

Water is a ubiquitous molecule found across the earth, present within (and often in large quantities) all living creatures. It has been a popular subject of art and literature (3), synonymous with the incomprehensible faculty of nature. Ancient cultures throughout history have recognised water's mystique and worshiped it as a god (4). Its life giving essence has captivated humanity since before recorded history. This essentialness to life cannot be understated; the mysteries of waters' unique and impossible to mimic behaviour has puzzled the scientific community for decades (5).

A fascinating molecule consisting of two hydrogen molecules covalently bonded to an oxygen molecule. There are many puzzling aspects of water which has secured it as one of earth's greatest mysteries. For example, water is densest in its liquid form, in contradiction to most other materials; reaching a density maximum at 4 °C (above its freezing temperature). Generally, most liquids are expected to decrease their isothermal compressibility as the temperature decrease. However, water actually increases its compressibility below 46 °C. Further to this it can be supercooled down to -38 °C (5). By the time it reaches this temperature the compressibility has doubled compared to 46 °C. The specific heat, c_p, of most other liquids is also expected to decrease with decreasing temperature, T, due to the decrease in entropy, S, however waters specific heat (at constant pressure) actually increases slightly below 35 °C (note, $c_p = (T/m)(dS/dT)_p$ where m is the mass). In its solid ice-form, it can tenant numerus crystal structures. Its bond structure is formed of weak dipole interactions between each molecule, which as an ensemble make water a staggeringly robust and resilient material; incidentally is has one of the highest specific heat capacities of any common substance (6).

Waters' unique characteristics are often ascribed to its complex hydrogen bonding (H-bond) structure. This H-bond network is constantly fluctuating with bonds breaking and forming on the picosecond scale (7). Hydrogen bonds are attractive dipole-dipole interactions between hydrogen atoms and a lone pair of electrons in a neighbouring electro-negative atom. Within this interaction a single water molecule can be hydrogen bonded to four other molecules forming a tetrahedral structure. In

ice (solid water), H-bonds orient the water molecules into the preferred tetrahedral shape, with a crystalline structure. In the liquid state, this tetragonality is maintained however, the structure is malleable and thus lacking crystallinity. The bond number decrease slightly to 3.5 per molecule whilst the number of nearest neighbours increases to five (8), causing the liquid state to be denser than the solid state.

Presently and throughout human history, water has been implemented in the invention of the steam locomotive, in the manufacturing of textiles, as a reactant in chemical processes and, of course, it is fundamental to agriculture, to mention just a few key areas of impact. Most interestingly of all, is its presence and vital role within virtually all forms of life.

Equally essential to life are lipids (9, 10). Lipid molecules form the plasma membrane matrix of both prokaryotic and eukaryotic cells. They assist in the meditation of cell function, acting as the primary barrier between the inter- and extra-cellular medium. Also referred to as the 'phospholipid membrane'. Proteins, peptides and ions all must interrelate with the lipid membrane in order for the cell to function and for life to flourish. In a broad sense the lipid membrane is an integral part of cell mitosis (11) as well as cell fusion (12), which has formed the evolutionally basis for all life on earth.

Unsurprisingly, the disposition of lipids and water to each other is observed throughout nature. Lipids appear alongside water across a staggering amount of different species, at a variety of length scales and located in, just about, any conceivable environment. The intricacies of this unique and ubiquitous pairing *may* contain the secrets of life itself; at the very least, the functional interaction of water with any bio-polymeric material (lipid or otherwise) is a mysterious and potentially bountiful field of research. It is through the elucidation of this elusive interaction that we may gift ourselves a glimpse at the frenzied, chaotic and curiously balanced dynamics of the microscopic world, where the very essence of all life, that is, living cells reside.

Lipids are mostly amphiphilic molecules comprising of a molecular headgroup and hydrocarbon tail. The amphiphilic characteristics of lipids allow them to form structures in the presence of water, whereby the polar (hydrophilic) headgroups

aggregates around the water, whilst the apolar (hydrophobic) tail groups aggregate with each other, shielded from the water by the headgroup/water interface (13). Through this mechanism, lipids often form bilayers in water, whereby the tails point inwards and the headgroups form the outer layers in contact with the water. The arrangement into these structures is largely driven by the hydrophobic effect (14), whereby it is entropically more favourable for the hydrophobic hydrocarbon chains to aggregate together. The effect is entropic in nature as the presence of apolar solutes disrupts the water's tetrahedral hydrogen bond structure, which is entropically unfavourable. Water molecules are then expelled back to the bulk phase allowing the overall entropy of the system to increase (15) and the hydrocarbon tails to aggregate together. This behaviour can be considered as an attractive force between the hydrocarbon chains. The arrangement into these nanostructures is also energetically favourable, since the hydrophilic headgroup dipole (discussed below) induces electrostatic interactions with the polar water molecules at the interface. By this effect, lamellar structures form into multilamellar vesicles (MLVs). It is also important to note, that MLVs can be turned into unilamellar vesicles (ULVs) through techniques such as sonication (16).

1.2 The Fluid Mosaic Model of the Biomembrane

Lipids constitute the core matrix of the cell membrane and are therefore an inextensible tool for model membrane research. The 'fluid mosaic model' (17), developed in the early 1970s, best describes the role the phospholipid membrane plays in the wider body of biological functions. Other complex molecules such as proteins and peptides exist in collaboration with the lipid membrane in order to facilitate cell function. Thus, the fluid mosaic model describes the lipid membrane to be in a *fluid* state, somewhat like an ocean, with proteins floating like icebergs in the membrane. Sometimes penetrating into or even piercing the membrane through to the inner-cell wall. Additionally, the extra-cellular medium also contains a diverse ensemble of ions with sodium, potassium, magnesium and calcium being some of the most prevalent. In addition to the salty there is also a sweet variety of sugars such as glucose and sucrose. Throughout nature, several species of plants and amphibians (18) have evolved traits which allow them to survive in some of the harshest

environments on earth. This includes the remarkable ability to undergo a complete freeze and thaw cycle of the entire body, with apparently little damage to the cell's tissue and function; a process known as 'anhydrobiosis' (19). It has been suggested that sugars, such as trehalose, within the amphibians biological make-up assist in membrane preservation during this phenomena. These electrolytes replace the interfacial water at the membrane surface so that when the bulk water within the organism freezes, the membrane is excluded from the damaging freezing effects. Proteins can form ion channels within the membrane as a gateway allowing specific ions to enter and exit the cell, again arbitrating cell function and biological processes (20). Naturally, across all these biological scenarios is the presence of water. Lipids and water are essential components in our understanding of many biological processes, such as membrane solute interactions, protein folding and cell fusion (21-23).

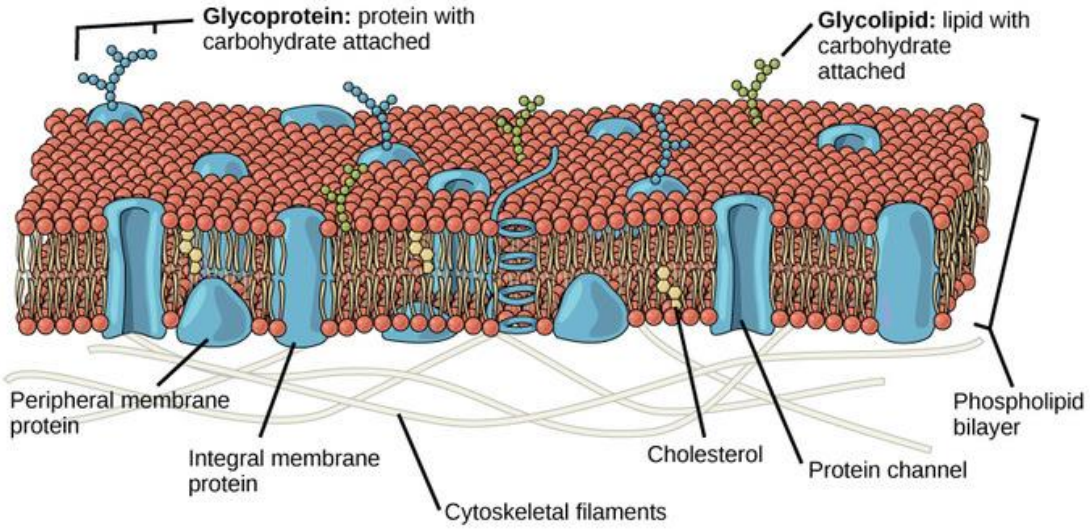

Figure 1.1 Fluid mosaic model, displaying the biomembrane matrix in orange-yellow tones, while integrated membrane proteins are shown in blue. It is important to note that the cytoskeletal structure shown is not in the fluid phase due to its non-zero shear modulus. The scheme has been taken from LibreText (24).

1.3 Lipid Self-Assemblies and Model Membranes

The first evidence of biomolecular lipid structures was observed in 1925 by Gorter and Grendel (25), demonstrating that chromocytes extracted from animal veins were covered in a 'lipoid' layer two molecules thick. This was the first substantial evidence of lipid self-assemblies, which have been studied extensively since the 1950s, owing to the development of advanced experimental scattering techniques. The pioneering work of Vittorio Luzzati (26-28) sought to understand these underlying structures, which eventually led to classification of individual lipid phases.

Planar lipid bilayers in their fluid state, fall under the class of smectic A type liquid crystals. Liquid crystals were first investigated in detail by de Gennes (29), who categorised and developed the underlying physical properties of this unique phase of matter. Smectic A liquid crystals are characterised by a macroscopic one-dimensional layered order, but with a remarkable absence of long-range order within each layer. The ability of lipids (as with most liquid crystal compounds) to display a variety of polymorphs is of great interest, because of their occurrence throughout nature; these polymorphs mostly occur in the presence of water. The most stable of these phases in excess water (therefore the most biologically relevant), are the lamellar phase, the inverse hexagonal phase, the bicontinuous cubic phase and micellar cubic phase (30).

The variety of lipid nanostructures that form are the result of the membranes curvature. As the membrane bends to greater and greater extents, it allows the structure to change from one mesophase to the next. During these transformations, the membranous interface will curve more towards the water, confining it into smaller and smaller compartments. As this mechanism occurs, the geometry of the water confinement changes from planar to tubular to spherical (9, 31). An interfacial curvature towards water is commonly defined as a negative curvature, whereas a positive curvature is characterised by polar/apolar interface curving towards the nonpolar medium (i.e., toward the membrane core). To characterise the possible mesophases in terms of its curvature, it is useful to determine the mean interfacial curvature, which the average of sum of the two principal curvatures, c_1 and c_2. Considering the lipid surface as a pure mathematical object, a point P on the surface will have two principal planes orthogonal to the surface in which the curvatures of the surface intersects. The radii of these intersections are the inverse of the two

principal curvatures c_1 and c_2 (see Figure 1.2). It is also instructive to consider the Gaussian curvature (32), which is the product of the two principal curvatures. The Gaussian curvature indicates the overall geometric shape the curvatures create. For example, spheres will have a positive Gaussian curvature, whilst flat planes or cylinders will have a zero Gaussian curvature. Negative Gaussian curvature indicates a hyperbolic or "saddle-like" geometry (33).

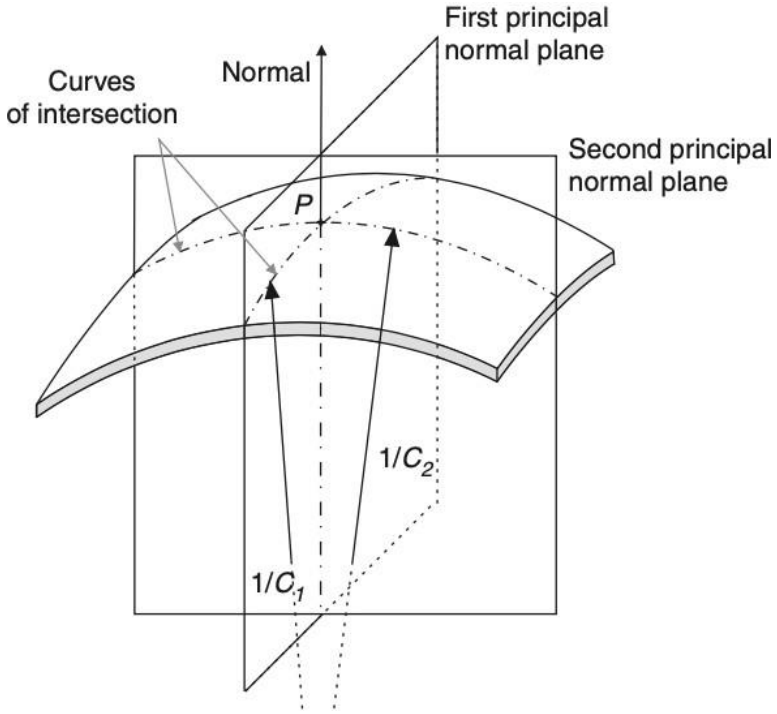

Figure 1.2 A curved surface denoting the point P and the orthogonal planes to the curved surface. The curved surface intersects the orthogonal planes as shown. The two principal radii are equal to the inverse of the two principal curvatures. Image adapted from (32).

As value of the mean interfacial curvature increases, driven by the lipids molecular shape, phase transitions occur. Changing the temperature and pressure will have individual effects on different regions of the lipid molecule, leading to different changes in the interfacial curvature. Through this simple parameter, the phase changes in the system can be understood and the emerging nanostructures are classified. The changing molecular shape is the main driving force behind phase transitions, indeed it also is the primary influence on the mean interfacial curvature. A key parameter which defines the molecular shape of the lipid is the *critical packing parameter*, also known as the shape parameter, *CPP*, first envisioned by Israelachvili

et al. (10). This is a dimensionless quantity, which relates the molecular volume to the volume of the lipid headgroup multiplied the lipid length:

$$CPP = \frac{v}{a_0 l_c} \quad (1.1)$$

where *v* is the volume of the hydrophobic tail region, a_0 is the effective headgroup area and l_C is the effective lipid length. Different values of CPP denote different molecular geometries, thus predicting which mesophase is likely to form (Figure 1.3). Whilst the *CPP* is a useful tool for describing molecular shapes, it does not consider shape anisotropy along an axis normal to the membrane (34). For example, shapes B and D in Figure 1.3 may appear as wedges along one perspective but more akin to cylinders along another. Shape anisotropy is an important concept, when describing how lipids form nanostructures around their relative water cores. For this reason, the local intrinsic curvature(s) around an individual lipid molecule must also be considered. In general, lipids with differing intrinsic curvatures will tend to have anisotropic shapes (32, 34). The signs of these intrinsic curvatures (being positive, negative or zero) as well as the relationship between them, will determine if the lipids shape is a wedge or inverted wedge as well as if the nanostructure is an inverse or regular cylindrical micelle as described by the *CPP* (shapes B and D in Figure 1.3).

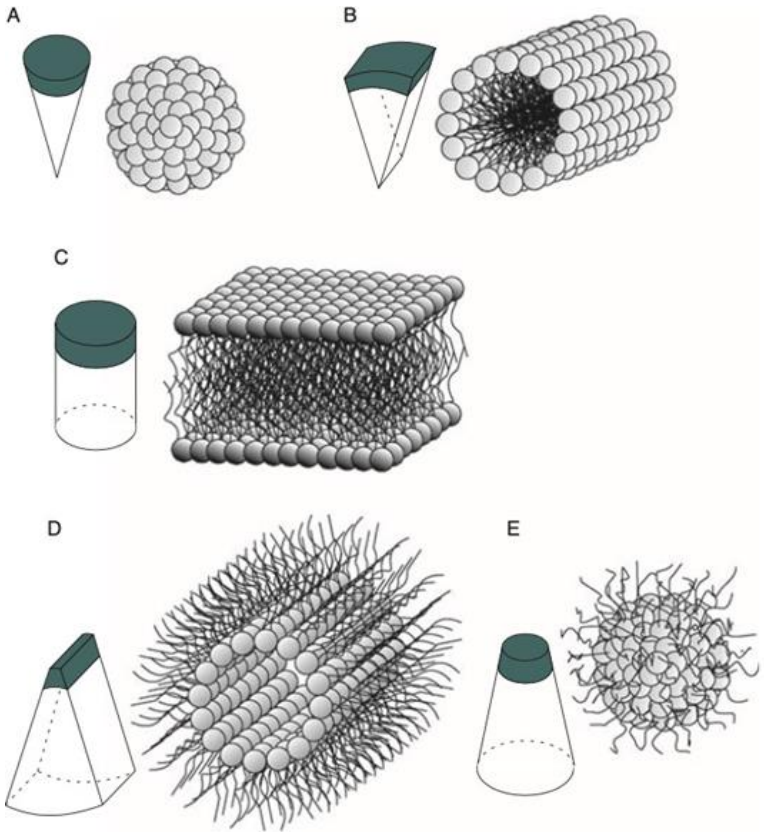

Figure 1.3 The effective geometric shape of the lipid shown with which mesophase each shape is likely to aggregate into. The head group shape/area is highlighted in green. (A) Cone geometry *CPP* < 1/3 forms micelles. (B) Truncated cone or wedge 1/3 < *CPP* < 1/2 forms cylindrical micelles. (C) Cylindrical geometry *CPP* ≈ 1 forms planar bilayer. (D) Inverted wedge *CPP* > 1 forms inverse hexagonal phase. e) Inverted truncated cone *CPP* > 1 forms inverse micelles. Image taken from (32).

There are many different lipid species which constitute the make-up of biological material. Different molecular shapes allows the cell to adopt different curvatures. Complementary to the numerous geometries of lipids and their self-assemblies, there are varieties of molecular compositions, which can produce unique properties of the lipid structure. Lipids chains can be saturated or (poly)unsaturated, influencing the shape parameter, but also influence membrane compressibility and dynamics (35). In addition to the hydrocarbon chain, the lipid headgroup is essential for interactions, which take place at the interface. This includes the reciprocity between water, but also with proteins, peptides and electrolytes. Some lipid headgroups have net charges (36), but more often than not, lipids are zwitterionic (37-40). In other words,

having a net neutral charge. Phosphatidylcholine (PC) and phosphatidylethanolamine (PE) are two such lipid species with an electronegative phosphate (P) arrangement in the headgroup. This phosphate forms a dipole with the nitrogen (N) in the choline or ethanolamine along the P-N vector. This dipole allows the headgroup to interact with other polar entities (such as water) in the vicinity. Across nature PC and PE lipids occur frequently and are a crucial ingredient in mammalian cell membranes (41). For this reason, they have become the focus of the presented studies.

As mentioned above, the fluid lamellar (also known as L_α- phase) is the lyotropic analogue to the smectic A-phase liquid crystal (37, 42). When forming MLVs, the lattice parameter *d* defines the repeat distance in the stacking direction of the bilayers. This *d*-spacing further subdivides into the headgroup-to-headgroup distance, d_{HH}, and the interlamellar water layer thickness d_W (Figure 1.4). There are several other important parameters to consider including the headgroup volume, V_H, the steric bilayer thickness, d_B, the chain length, d_C, and the area per lipid, A_L. For PC and PE lipids there is also the important *partial headgroup thickness*, which defines the distance of the headgroup/chain boundary to the phosphate group. This distance has been well resolved experimentally (43, 44) to a thickness of 0.49 nm (37), denoted as D_{H1}. All these parameters are also applicable to the inverse hexagonal phase (for more details see Chapter 4).

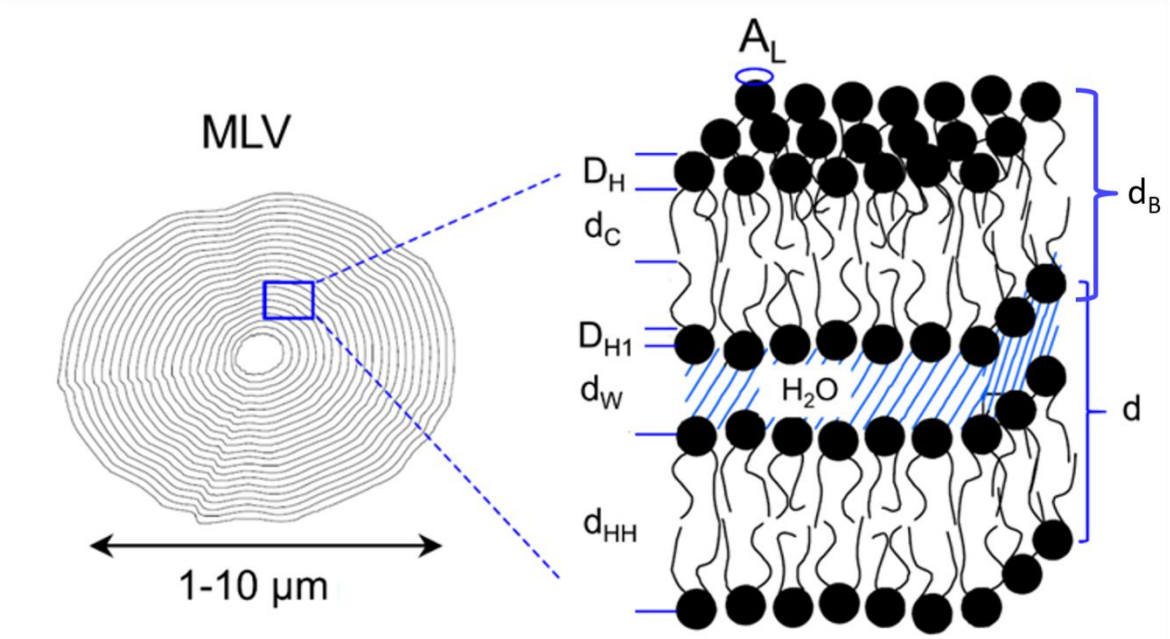

Figure 1.4 A multilamellar vesicle (MLV is shown) on the left. On the right, commonly used structural parameters of phospholipid bilayer stacks are defined: the headgroup extension D_H, the chain length d_C, the phosphate to headgroup/chain boarder distance D_{H1}, the water later thickness d_W, the head-to-headgroup thickness d_{HH}, the steric bilayer thickness d_B, the area per lipid A_L, and the lattice parameter d.

1.4 Intermembrane Forces

Across the confined water layer in lamellar crystals are different forces at work to establish and maintain membrane stacking. The first force to consider is the attractive van der Waals (VdW) force acting between two adjacent membranes. For a membrane of thickness, d_B, at an intermembrane water separation distance, d_W, the VdW force per unit area is (9):

$$f_{VdW} = -\frac{H}{12\pi}\left(\frac{1}{d_w^2} - \frac{2}{(d_w+d_B)^2} + \frac{1}{(d_w+2d_B)^2}\right) \quad (1.2)$$

where H is the Hamaker constant. The Hamaker constant is dependent on the dielectric permittivity of the intermembrane medium (in this case water) and its contrast to the dielectric constant of the lipid headgroup region. Changes in water density and structure can alter H and ultimately affect the attractive binding energy of the VdW force. This force persists over long inter-membrane distances and is balanced by several repulsive forces.

The shortest ranged repulsive force is the steric repulsion between lipid headgroups. The steric repulsion mediates the somewhat incomprehensible scenario that lipid headgroups of opposing leaflets may overlap with one another, therefore experiencing a repulsion which permits it from being so. Coming into play when bilayers are at risk of 'collisions', the steric repulsion is only significant at very small water separations, d_W < 0.4 nm. At slightly larger distances of $d_W \approx$ 0.4-0.8 nm, the repulsive hydration force predominantly opposes the VdW force. Although this force is somewhat poorly understood (45), its existence is apparent in experiments, shown to take the form (9):

$$f_H = P_H \lambda e^{\left(-\frac{d_W}{\lambda}\right)} \tag{1.3}$$

where λ is the decay length of usually 0.1-0.3 nm. The prefatory, P_H, is in the order of 10^8 Jm^{-3}. The final important repulsive force, which acts over very large water separations, d_W > 1 nm, is the Helfrich undulation force (46). This force accounts for the out of plan bilayer fluctuations as the membrane bends. As undulations increase, meaning the membrane deviates from its equilibrium position, the force increases concurrently. The Helfrich force per unit area is given by (9):

$$f_H = \frac{(k_b T)^2}{K_c d_W^2} \tag{1.4}$$

where k_b is the Boltzmann constant, T is the temperature (in Kelvin) and K_c is the membrane bending modulus. All these aforementioned repulsive forces oppose the VdW force in order to keep the system balanced, acting as a function of intermembrane distance, d_W. These forces constitute the intermembrane potential, which determines the free-energy landscape of the lamellar crystal. At a particular distance the summation of these forces reside in an energy minima, which determines the preferential water spacing distance d_W. Factors such as temperature, pressure and membrane hydration may alter at which distance this minima occurs.

The situation is further complicated when electrolytes are incorporated. Charged moieties, such as ions, can be dissolved in the aqueous phase. Charges disperse in the water but may also interact directly with the membrane interface, thus altering the interfacial charge density. Such alterations produce electrostatic repulsions between bilayers, which are mediated by their own decay lengths depending on the ion type, intrinsic charge, but also the ion concentration. The measurement and

stratification of such electrostatic forces is not trivial but they have been shown to take the form (47):

$$f_e \cong \frac{2\sigma_s{}^2\lambda_{DH}}{\varepsilon_0\varepsilon_r} e^{\left(-\frac{d_w}{\lambda_{DH}}\right)} \quad (1.5)$$

where σ_S is the membrane surface charge density, λ_{DH} is the Debye-Hückel screening length and ε_0 and ε_r are the permittivity of free space and relative permittivity of the solution medium (in our case water). Additionally, the dipole moment of the lipid headgroup creates an electrostatic interaction with the headgroup dipole of neighbouring bilayers. The dipole potential is dependent on the headgroup orientation (observed through apparent headgroup thickness D_H). This orientation is strongly influenced by the water content (48) and therefore by the inter-lamellar water spacing, d_w. The dipole of the headgroup will tend to orientate water molecules in the vicinity which also contributes to the surface dipole potential between membranes.

1.5 Research Question

The hypothesis for this research project is that there is an interplay between lipids and the water matrix, which may influence the structure and dynamics of both entities. The behaviour of the lipid assembly influences the structure and dynamics of the water molecules and *vice versa*. Understanding the subtleties of this proposed interaction will form a deeper understanding of lipid self-assemblies as a whole by producing a more holistic model of the water behaviour in conjunction with membranes. There are many open questions surrounding the water-lipid hydration mechanism. Some interesting examples include the phase alignment of cholesterol rich domains. These so-called liquid ordered (L_o) membrane rafts, which align in radial direction of MLVs of supported lipid films, observed as a distinct set of diffraction peaks next to the diffraction peaks of the liquid disordered phase (L_d) (49). A deeper understanding of hydration inhomogeneity across the membrane may offer an explanation. Additionally, the postulation of inter membrane water hydrogen bond bridges (45), may explain the strangely close registry of PE membrane leaflets compared to PC membranes. Whilst the obvious volumetric differences will influence

hydration capability, this does not explain why the inter-lamellar water does not swell, even under the influence of thermal fluctuations (1).

The ***aim of the project*** is to produce a deeper understanding of confined water behaviour and its relationship to the lipid matrix in the hopes of producing a broader model for lipid self-assemblies, where *water and lipid* are regarded as a single inseparable entity.

The ***project objectives*** aim to understand the lipid/water structure and dynamics in planar and tubular confinement, applying a new model for describing three different water regions. The three regions concern (i) 'the headgroup water', (ii) 'perturbed water' near the membrane/water interface and (iii) a core layer of 'free water' (unperturbed water). The objectives are the following:

- **Objective 1**: Demonstrate the confined water organisation model in planar confinement under the influence of temperature and hydration properties (see Chapter 3).
- **Objective 2**: Demonstrate the confined water organisation model in tubular confinement under the influence of temperature and membrane curvature (see Chapter 4).
- **Objective 3**: Demonstrate the confined water organisation model in planar confinement under the influence of cations with chaotropic to kosmotropic character (see Chapter 5).

Chapter 2. Experimental Methods: X-Ray Diffraction of Lipids Self-Assemblies

2.1 Introduction to X-ray Diffraction

As discussed in Chapter 1, lipids form self-assembled *crystalline* structures when hydrated with water. X-ray scattering techniques are an invaluable, non-evasive tool in understanding lipid self-assemblies formed in water similar to their natural environmental conditions. Fundamental concepts of X-ray crystallography were developed at the University of Leeds by William H. Bragg, winning the Nobel Prize for Physics in 1915. This pioneering work explained the origin and occurrence of diffraction peaks. X-ray scattering is now routinely used to categorise the atomic or molecular structure of a variety of materials used across science and industry.

Diffraction of X-ray derives from the phenomena of crystalline atomic planes (or molecular planes for the case of soft matter systems) to act as diffraction gratings, producing interference patterns. X-rays are scattered in all directions from the electron contrast within the atomic planes and display constructive or destructive interference, depending on the phase difference of the incident waves compared to the waves received at a detector at an angle, θ from the scattering plane. Such reflections are known as *Bragg reflections*, and the intensity peaks are recorded as a function of scattering angle, 2θ. The relationship between the scattering angle and the inter-atomic distance (also known as the lattice spacing), *d*, is expressed using *Bragg's law*:

$$n\lambda = 2d_{hkl} \sin\theta \qquad (2.1)$$

where λ is the X-ray wave length and d_{hkl} is related to the lattice planes described by the Miller indices *h*, *k* and *l* (for their definition refer to the text book of Kittel (50)). *n* is the order of Bragg reflection, which must be an integer value for constructive interference to occur and a diffraction peak to be observed. For centrosymmetric crystals, such as lipid bilayer stacks, the condition for constructive interference to be fulfilled only occurs, when the phase difference between detected and incident waves is either 0 or π. Such a situation will produce an intensity maxima, hence a diffraction peak.

In the recorded intensity pattern are two types of scattering present: the diffuse scattering due to the electron contrast (originating from the building block in the crystal unit cell, the membrane in our case) and the diffraction scattering arising from the ordered crystal structure. In scattering theory the former is called the *form factor* contribution, and the latter is referred to as the *structure factor* contribution (51), referring to the *crystal structure* which, for instance, can take the form of 1D lamellar stacks or 2D arrangements of rod-like micelles. The scattering intensity is a product of both the form and structure factor as a function the scattering wave vector modulus, *q*. The modulus of the scattering vector, *q* derives from Braggs law and is expressed as:

$$q = \frac{4\pi sin\theta}{\lambda} = \frac{2\pi}{d} \tag{2.2}$$

where λ is the wavelength of incoming X-rays and θ is half the scattering angle. *d is* the lattice spacing. The overall scattering intensity is given by:

$$I(q) = \frac{S(q)|F(q)|^2}{q^2} \tag{2.3}$$

Where *S(q)* is the structure factor contribution and *F(q)* is the form factor contribution (see Figure 2.1). Normalising by q^2 is known as the Lorentz correction (52). This correction needs to be applied to account for two geometrical factors. The first of which is resultant from the diffraction pattern to appear as Debye-Scherrer rings for isotropic scatterers (Figure 2.2), where the total recorded intensity is proportional to $2\pi q$ (the circumference of the ring). The radius of the ring is related to the scattering angle and therefore also related to the scattering wave vector, *q.* From the convention that all 1D-scattering curves (see Figure 2.1) are displayed as if recorded by a 1D-detector, only a constant part, *dq*, from each diffraction peak is captured. *dq* represents a fraction of the total intensity of a given Debye-Scherrer ring. Therefore, each diffracted intensity must be normalised by its *q* value, since the total recorded intensity, *I(h),* is proportional to its wave vector, *q(h)*. The second correction, derives from the fact that at any given instrumental resolution *dq*, the number of crystallites fulfilling Braggs law is inversely proportional to the scattering vector *q* (52).

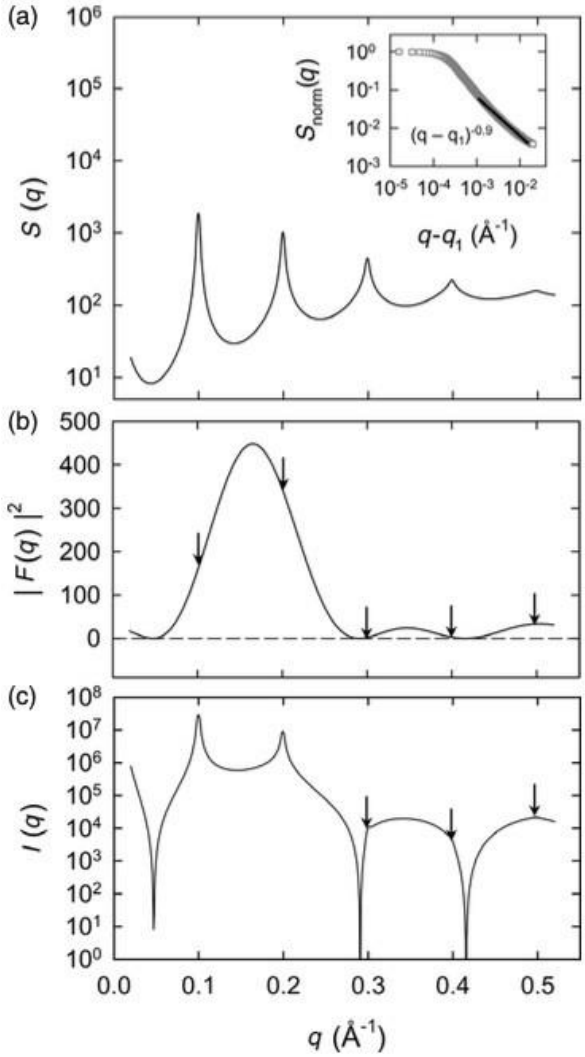

Figure 2.1 The scattering contributions arising from multi-lamellar bilayer systems. (A) The structure factor contribution as a function of q according to MCT. The inset shows a double logarithmic scale of the structure factor decay normalised to the first order Bragg peak. (B) The absolute square of the form factor. (C) The overall scattering intensity. Arrows in (b) and (c) indicate the position of the Bragg peak. Image taken from (53).

2.2 X-ray Scattering from Lyotropic Liquid Crystalline Systems

2.2.1 Lipid Bilayer Scattering Displaying Disorder of the Second Kind

For a single crystal, the diffraction peaks will appear as single points. For powders or isotropically oriented liquid crystals (such as MLVs in solution) the diffraction pattern appears as Debye-Scherrer rings on a 2D-detector. Due to the absence of any crystal structure in ULV dispersions, they will produce diffuse scattering only. MLVs display both diffuse scattering arising from the membrane and diffraction rings arising from

the radial 1D-stacking of the membranes. If our sample were to be supported, such that the lamellar stack is aligned vertically like a film in grazing incidence scattering (54), the scattering pattern would appear as a vertical set of diffraction peak points (perfect stacking) or arcs, if the film displays orientational imperfections (Figure 2.2).

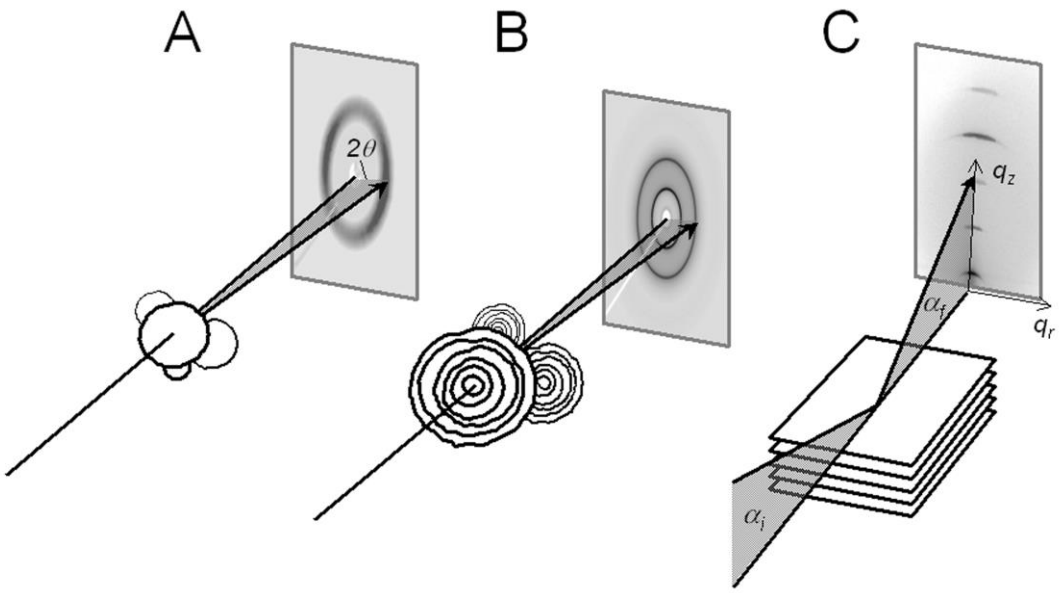

Figure 2.2 Typical X-ray scattering cases from lipid-based membrane systems. (A) Diffuse scattering from ULVs, (B) powder diffraction from MLVs, and (C) Grazing incidence small angle X-ray diffraction from supported membrane films. This figure has been taken from (9).

Lattice disorder is present in all crystals and is considered in the description of the structure factor. If crystalline structures would contain absolutely no disorder, then their diffraction peaks would be resemble delta functions. However, this case practically does not exist. As such, crystal disorder manifests in two important ways, namely, disorder of the *first* and *second* kind.

Disorder or the first kind, also known as *thermal disorder,* is regularly seen in solid crystals, where motion about the lattice points (individual atoms) are localised around an equilibrium position, maintaining the long-range order of the crystal lattice. This allows the diffraction peaks of solid crystals to be sharp and well defined. Here, the intensities will decays exponentially with the diffraction order, but the diffraction peak width is conserved.

Disorder of the second kind is far more relevant to soft matter systems like lyotropic liquid crystals. Here the motion of building block, in this case the membrane,

is dictated by the position and motion of its neighbouring membranes. Therefore the uncertainty in the equilibrium position of an individual membrane increases with the number of membranes in the stack to such an extent that long-range order is lost (51). Disorder of the second kind not only dampens the intensity of the diffraction peaks, but also broadens the reflections as a function of the scattering angle. Indeed at heightened fluctuation distances under the influence of increased in Helfrich undulations (Equation 1.4), the diffraction peaks from the second order onwards can become broad and weakly defined. For this reason, the long-range order in lyotropic liquid crystals is actually only a *quasi-long-range* order.

Due to the typical length scales of lyotropic liquid crystals (5-10 nm), we have used Small Angle X-ray Scattering (SAXS) in these presented studies. As the name suggests, SAXS measurements take place in the small angle regime, resolving scales from 1-300 nm. This makes SAXS ideal for the study of lipid self-assemblies.

2.2.2 SAXS Data Reduction

The raw scattering data must undergo several important corrections before it is fit for analysis. Firstly, the so called 'zero position' of the direct beam must be set. Most important, when analysing several data sets for the system, this step essentially assures that the *q*-axis origin coincides with the direct beam position.

Next the measured intensity should be corrected for incoming flux and the different sample transmissions. The former correction ensures the measured intensity is corrected for the incident flux I_0. The latter normalises the scattered intensity by its transmission, ensuring that all experimental curves are normalised according to their X-ray absorption aptitude. Practically, both corrections can be combined into one by dividing the recorded scattered intensity, *I(q)*, by the transmitted intensity, I_T, which is measured after the sample position, for instance by the attenuated direct beam intensity or by a diode placed in the instrument's beamstop (55):

$$I_{corr}(q) = \frac{I(q)}{I_0 \cdot I_T/I_0} = I(q)/I_T \qquad (2.4)$$

Thirdly, the background scattering from the empty capillary and the solution must be removed. This is done in two steps. First the measured empty capillary

scattering is subtracted from both the recorded solution *plus* capillary scattering, as well as the recorded dispersion *plus* capillary scattering. Second, the pure solution scattering is subtracted from the pure dispersion scattering. However, the solution scattering can only be directly subtracted from the dispersion scattering for very dilute dispersions (< 1 vol%). Generally, the *excluded solution volume* in the dispersion must be considered. For example, in a sample comprised of 40 wt% lipids (which to a good approximation equals 40 vol%) only 60% of the solution scattering should be subtracted. Simple though it seems, the reality is slightly more complicated. Variations in capillary diameter and weighing errors can influence the correct *excluded volume fraction*, causing it to deviate from the expected value. Thus, this correction factor should be fine-tuned to match the intensity of the solution to the zero-points of the form factor given in dispersion scattering (see Figure 2.1 b). Practically speaking, the form factor zero-points of the dispersion and solution scattering must be equal before subtracting the *excluded volume* solution scattering contribution (in our case water).

2.3 Modelling of the Lamellar Fluid Lipid Bilayer from Scattering

After the data correction, analysis may begin, where the all-important physical membrane parameters are calculated. Over the decades, various membrane models have been developed. The first membrane model was suggested by Luzzati (27), dividing the lattice spacing (*d*-spacing) into a bilayer thickness d_{LZ} and water layer thickness d_W. This model describes the lipid/water interface as a sharp boundary, also known as the 'Gibbs-Dividing Surface' (56). Since we are considering the water interface in detail throughout these studies, it is useful to keep the Gibbs-Dividing Surface at the forefront of our interpretations.

The next important models to consider are the bilayer strip models and Gaussian-based bilayer models (Figure 2.3), which simulate the electron density profiles across the bilayer (57, 58). The simplest Gaussian bilayer model describes the electron density profile across the bilayer with three Gaussian distributions, two positive electron density contrasts for each headgroup, and one negative for the chain region. For well-ordered fluid membrane stacks, the electron density profile (EDP) is directly

obtainable from small angle X-ray diffraction experiments (57-59). However, to produce an accurate EDP, at least four diffraction orders need to be recorded, which is problematic for fully hydrated and *quasi-ordered* membrane stacks. The EDP is useful to determine because it allows direct measurement of the approximate membrane thickness. What is commonly referred to as the 'headgroup-to-headgroup' distance, d_{HH}. This value is measured from the distance of the two given maxima in the EDP (Figure 2.3B: note, $d_{HH} = 2\ z_H$).

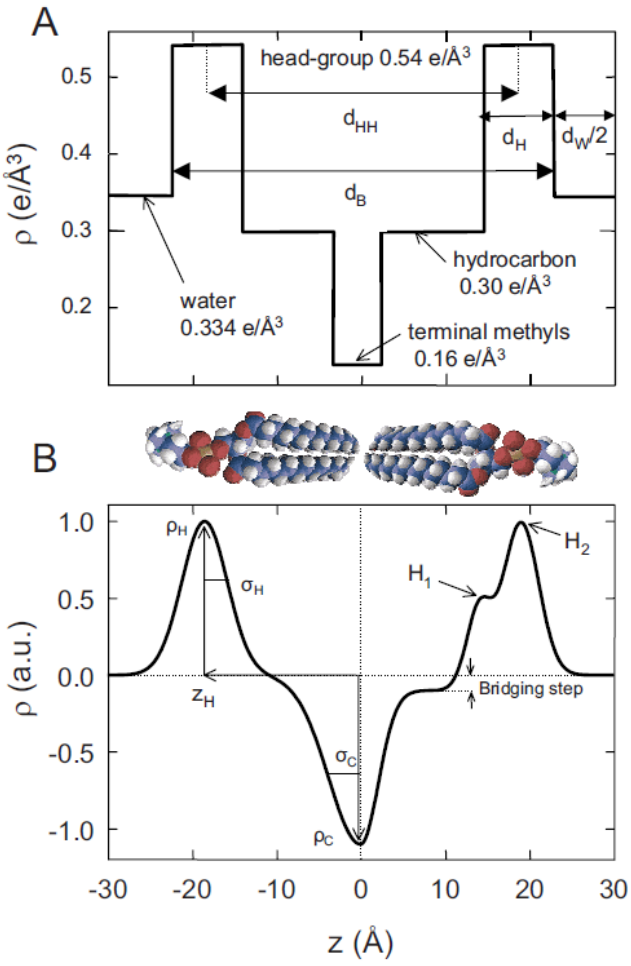

Figure 2.3 Phospholipid bilayer models. (A) A strip-model and (B) two different Gaussian component models are presented. Two lipid molecules are depicted to illustrate the bilayer electron density profiles. Figure taken from reference (57).

To actually calculate EDP of a bilayer systems *model-free*, Fourier analysis of the diffraction pattern is required. The EDP is the result of the Fourier series analysis of the recorded diffraction data. For centrosymmetric structures, only the cosine terms need to be considered in the analysis:

$$\rho(x) = \sum_{h=1}^{h_{max}} \alpha_h F_h \cos\left(\frac{2\pi x h}{d}\right) \qquad (2.5)$$

where h is the diffraction order, F_h are the form factor coefficients. Obtaining the coefficients is achieved from the square root of the Lorentz corrected area for each diffraction peak. d is the lattice spacing, obtainable from Equation 2.2. For SAXS experiments of lamellar systems, the peak position scales linearly with the diffraction order, i.e., the second peak is at twice the q value of the first peak, the third order at three times the value and so forth. x denotes a position in real space. The α_h parameter in the formula refers to the phasing of each diffraction order. The 'phase problem' arises from the nature of the recorded intensity, $I(q)$, being proportional to $F(q)^2$, meaning the amplitude's phase are unknown, since all intensities are naturally recorded as positive values. Conveniently for centrosymmetric structures, the phasing reduces to values of $\pm\pi$, resulting in phasing factors, $\alpha_h = \cos(\pm\pi) = \pm 1$ (60). Various methods have been employed to solve the phasing problem (61, 62). Often *a priori* knowledge of the bilayer structure is used, testing all possible phase combinations to see which result most closely resembles the expected model (39, 63). For multilamellar phospholipid-based phases, the phase combination goes as: -1, -1, +1, -1, -1 for the first five diffraction orders (57).

Alternatively to determining the EDP *model-free* with Fourier analysis, SAXS curves can be fitted by applying models. Scattering measurements take place in inverse space (50). As discussed above, in inverse space the scattering intensity is a product of the form and structure factor, which refers in real space to a *convolution* of the membrane profile and the 1D-lattice structural motif (or building block). Applied fitting models must account for both contributions, form and structure factor, which allows data fitting over the entire recorded q-range.

Although a calculated EDP provides structural details, it does not produce information about membrane dynamics. For a fuller picture, we must implement models that consider the 1D-lattice stacking including its disorder. The first model to consider disorder of the 2nd kind was the paracrystalline theory (64, 65). Whilst this theory works well for various polymer applications and rigid membrane systems, it does not consider membrane bending which frequently occurs for lyotropic liquid crystals. It was in Caillé's ground-breaking work (66) that, not only membrane fluctuation, but also membrane bending was considered in the description of disorder of 2nd kind. Later Nagle and collaborators published a structure factor

description known as the Modified Caillé Theory (MCT) (67), able to measure membrane fluctuations from the tailing of the diffraction peaks. The mean square separation of adjacent bilayers decays logarithmically according to MCT. The intensity in the structure factor decays with a power law behaviour (see Figure 2.1 inset), influenced by the bending and bulk compressibility moduli of the membrane system. The scope of fluctuation is summarised in the Caillé fluctuation parameter, η, which is given by (68):

$$\eta = \frac{\pi k_B T}{2d^2\sqrt{BK_c}} \tag{2.6}$$

where k_B is the Boltzmann constant, T is the temperature and d is the d-spacing. B and K_c are the bulk compressibility and bending moduli, respectively. Further, η is related to the physical fluctuation distance, σ, through the equation (69):

$$\sigma = \sqrt{\eta}\,\frac{d}{\pi} \tag{2.7}$$

With these parameters, we are able to form a detailed picture of membrane dynamics. As previously discussed, membrane fluctuation broadens the diffraction peaks as a function of q. MCT therefore quantifies the peak broadening by the tailing off of the peaks, such that peaks with longer tails suggest a higher degree of fluctuation.

In the global fitting ansatz (56, 70), both form and structure factor are applied to fit the entire SAXS diffraction curve. The bilayer model applied in this studies uses three Gaussian distributions, one for each headgroup region and one for the hydrocarbon core (cp. Figure 2.3 B, left). Each of the annotated lengths is used as a fitting parameter to estimate the EDP, which serves to fit the diffuse form factor scattering contribution.

Optimising the curve fitting leads equally to a refined structure factor calculation. The fit result pertain the lattice parameter, *d,* and lattice disorder, which is related to the mechanical parameters of the bending and bulk compression moduli (Equation 2.6). Fitting both form and structure factor contributions also means that disordered samples can be analysed and accurate information about the membrane thickness and fluctuations distances are obtained. Even in the case of broad or weakly defined diffraction peaks.

Chapter 3 Planar Confined Water Organisation in Lipid Bilayer Stacks of Phosphatidylcholine and Phosphatidylethanolamine

Abstract

Phospholipid-based liposomes are abundantly studied in biomembrane research and used in numerous medical and biotechnological applications. Despite current extensive knowledge on membrane nanostructure and its mechanical properties under various environmental conditions, there is still a lack of understanding on interfacial lipid-water interactions. In this work, the nature of the confined water layer for L-α-phosphatidylcholine (egg-PC), 1,2-dioleoyl-*sn*-glycero-3-phosphocholine (DOPC), 1,2-dimyristoyl-*sn*-glycerol-3-phosphocholine (DMPC) and 1,2-dimyristoyl-*sn*-glycero-3-phosphoethanolamine (DMPE) in the fluid lamellar phase of multilamellar vesicles was investigated. A new model for describing three different water regions is proposed, which have been characterised using a combination of small angle X-ray scattering (SAXS) and densitometry. The three regions concern (i) 'the headgroup water', (ii) 'perturbed water' near the membrane/water interface and (iii) a core layer of 'free water' (unperturbed water). The behaviour of all three layers is discussed as a function of temperature, concerning influences of chain saturation and headgroup type. While the overall water layer and perturbed water layer thickness increase with temperature, the free water layer displays the opposite trend for PCs, and in PEs is completely absent. Furthermore, an estimate of the temperature dependent headgroup orientation is given for both, PCs and PEs. The newly presented structural data deduced from the three-water region model will be useful for future refined molecular dynamics simulations and allow a better theoretical understanding of the attractive Van der Waals force between adjacent membranes.

3.1 Introduction

Amphiphilic lipid self-assemblies belong to the class of lyotropic liquid crystals, and as such, they display a variety of complex mesophases and nanostructures, depending on the environmental conditions, lipid type and molecular shape (9, 10, 71). In this study, we focus on the biologically most significant fluid lamellar phase of phospholipids, which form the core matrix of plasma cell membranes (72-74). In particular, we investigated the hydration behaviour of phosphatidylethanolamine (PEs) and phosphatidylcholine (PCs) multilamellar vesicles (MLVs); two very prominent biomimetic model membrane systems (37-40, 75). Generally, liposomes of multilamellar and unilamellar vesicles are widely studied as model systems for understanding the role of the biomembrane matrix in solute interactions, raft formation and fusion processes (21, 23, 76, 77). Further to this, their importance is fundamental in the design of nanoparticles for drug delivery (78-81), due to their low toxicity, compatibility with cellular membranes as well as tuneable functionality. More recently, membrane research is focussing on the understanding of essential processes of life through modular reconstitution of artificial and minimal cells (82, 83), and the use of giant unilamellar vesicles (GUVs) as bioreactors for artificial cell replication to take place (84). All these applications have been bolstered by the information extracted from studying the fluid lamellar phase.

Biomembranes exist in excess of water and the extent of membrane hydration is primarily dictated by the propensity of the headgroup to form hydrogen bonds with interfacial water molecules (85). Elevated temperatures increase the area per lipid due to enhanced chain splay (86), which increases the hydration as the headgroup occupies a larger volume. Another factor influencing chain splay is the number of double bonds along the chain, which dictates the chain disorder, and thus influences in turn the area per lipid. Considering the membrane hydration in each case, PCs are known to hydrate well, displaying a full hydration limit at around 43 wt% of water (37, 87), compared to about 25 wt% in PEs (31, 88). Further, molecular dynamics (MD) simulations on PC membranes indicate, that a clathrate shell forms around the choline moiety due to the hydrophobicity of the methyl groups (89-91), allowing a greater number of water molecules to become associated with the headgroup of PCs. Additionally, the PC headgroup's greater volume and larger area per lipid provide a

greater physical space for interfacial hydration to take place (37). Hydrogen bonding at the lipid/water interface primarily occurs at the oxygen atoms associated with the phosphate of the lipid headgroup as well as at the carbonyl group of the ester linkage in both PCs and PEs.(89, 92, 93) It has also been put forward that inter-bilayer hydrogen bond bridges between adjacent PE membranes prevents the MLVs from swelling.(43, 94)

Our understanding of membrane properties is based on several theoretical aspects. Firstly, the formation of a lipid bilayer is driven by the hydrophobic effect (14), whereby it is energetically more favourable for the polar headgroup to aggregate in an aqueous environment, while the hydrophobic chains will prefer to aggregate among each other (95). Thus, the headgroup interface forms protective layers largely excluding water molecules from the hydrophobic core of the bilayer (13). The first membrane model was suggested by Luzzati (27), dividing the lattice spacing (*d*-spacing) into a bilayer thickness d_{LZ} and water layer thickness d_W. This model describes the lipid/water interface as a sharp boundary, also known as the 'Gibbs-Dividing Surface' (96). In the fluid phase of PCs and PEs this boundary is close to the position of the phosphate atom of the headgroup (37). Whilst this model is a reasonable approximation, and works well for PCs and PEs to derive structural parameters such as the membrane thickness, it does not reflect the true interfacial details of the distribution of water at the polar/apolar lipid water interface. The next membrane models to gain popularity were bilayer strip models and Gaussian-based bilayer models, which simulate the electron density profiles across the bilayer (Figure A1) (56, 70). The simplest Gaussian bilayer model describes the electron density profile across the bilayer with three Gaussian distributions, two positive electron density contrasts for each headgroup, and one negative for the chain region (97). From well-ordered fluid membrane stacks (as a rule of thumb, at least four diffraction orders need to be recorded (57)), the electron density profile (EDP) is directly obtainable from small angle X-ray diffraction experiments (59), while for less-ordered fluid lamellar systems their bilayer structure is commonly analysed by applying global fitting procedures (51, 58). Once the refined bilayer EDP is obtained, it is possible to determine the head-to-head distance, $d_{HH,}$ from the positions of the two positive electron density maxima. In order to take into account not only the form factor

scattering contributions (arising from bilayer scattering), but also the structure factor contributions (lattice scattering contributions), we applied a global fitting method in this study described in more detail in the Material and Methods section and works of Georg Pabst and colleagues (70, 98). Importantly, it allows us to additionally evaluate membrane fluctuations in the MLVs resultant from the mechanical behaviour of the bilayers.

As outlined above, great knowledge on the nanostructure of lipid self-assemblies has been accumulated, however, there is still a lack of understanding of membrane behaviour in conjunction with its confined water. Studies are scarce which investigate how the lipid and the confined water layer interact, and rarely a holistic view is applied, treating the lipid/water systems as a single inseparable unit. Exceptions concern the work of Mezzenga and co-workers, who have focussed on the confinement of water in various lipid self-assemblies (99). They have shown that low-temperature crystallisation of molecules into a hexagonal structure is prevented and only amorphous ice forms. Pabst and colleagues included in their latest bilayer modelling also a fixed number of headgroup-bound waters next to an unbound water distribution (100). More specifically, Kasson et al. have shown that water ordering takes place at the membrane interfaces, when simulating the fusion of two vesicles. This surprisingly leads to a form of hydrophilic confinement of non-bulk-like water behaviour (101). More generally, in terms of the waters' behaviour relative to the planar lipid bilayer, McIntosh and co-workers have published several studies on membrane hydration and water depth penetration, which suggest vastly differing hydration processes between PCs and PEs (43, 94, 102, 103). Within confined water research, Wurpel et al. used coherent anti-Stokes Raman (CARS) techniques, showing some evidence suggesting weakened hydrogen-bonds (H-bonds), when interlamellar waters were confined in MLVs (104). These weakened H-bonds among interlamellar waters was confirmed again with attenuated total reflection Fourier transform infrared (TR–FTIR) (105). More recently it has been suggested in a NMR study that 'bound water' near the region of the lipid headgroup is more stable than bulk water, having a more restricted motion and longer stability than that of the bulk (106). This study also supports the idea of distinct water species within the confinement. In all

these works, however, there is a lack of discussion on what consequences these observations might have on the bilayer in return.

There remain many open questions regarding membrane behaviour, for which it might be possible that water structuring around the bilayer could give some answers. For example, the incorporation of cholesterol into the bilayer can induce cholesterol-rich domains, so-called liquid ordered (L_o) membrane rafts, which align in radial direction of MLVs or supported lipid films, i.e., L_o-membrane domains register in stacking direction, and are observed as a distinct set of diffraction peaks next to the diffraction peaks of the liquid disordered phase (L_d) (49). Cholesterol imbeds itself along the hydrocarbon chain, reducing its degrees of freedom (107), reducing the area per lipid and increasing the membrane thickness, which in turn disrupts the homogeneity of hydration across the membrane, in which L_d and L_o stacked domains coexist (108). To this end, it remains an open question (109), if these confined water differences may have any effect on the stacking alignment of L_o and L_d membranes, respectively. The effect of interfacial water structure might be of great importance for solving this poorly understood phenomenon. Secondly, whilst it is fairly well understood that PEs hydrate poorer than PCs, it is comparatively less understood why this should bring the adjacent bilayers in PEs into such a close separation distance of 0.4-0.5 nm only (45). It seems an additional attractive force contribution is missing to fully understand the thin interlamellar water spacing. Hopefully, these and other open questions can be better understood from more in-depth studies on the confined water structure.

In this study, using a combination of small angle X-ray scattering (SAXS) and densitometry, we are proposing a new distinctive description of individual water regions. Our model accounts for three water layers, namely concerning ‘headgroup water’, ‘perturbed water’ and ‘free water’.

3.2 Materials and Methods

3.2.1 Materials

L-α-phosphatidylcholine (egg-PC), 1,2-dioleoyl-sn-glycero-3-phosphocholine (DOPC), dipalmitoyl-*sn*-glycerol-3-phosphocholine (DMPC), 1,2-dimyristoyl-*sn*-glycero-3-phospho-ethanolamine (DMPE) were purchased from Avanti Polar Lipids (Alabaster, AJ, USA) and used without further purification. All lipids had a purity of >99%, except egg-PC >95%. All lipids were studied exclusively in their fluid phase, therefore all measurements were carried out above their melting temperature T_m. The experimental temperatures ranged from a few degrees above T_m (note, melting points are given in section 3.3.1) up to 80 °C.

3.2.2 Densitometry Measurements

Samples were prepared in concentrations of 10 mg/ml using ultrapure, distilled water (resistance 18 MΩ cm) and vortexed for at least 5 minutes until the lipid was fully dispersed forming MLVs. Density measurements were taken using an Anton-Paar DMA-4500M densitometer (Graz, Austria). The apparatus measures density via the vibrating tube principal (110). We note that the formation of air bubbles within the tube can affect the densitometry measurements quite significantly. Thus, air bubbles were removed by placing the sample in a shaking water bath for 5 minutes and then stirring it on a hot plate at 80°C for another 5 minutes.

Equation 3.1 converts the measured density values into the partial specific volume per lipid (110, 111),

$$\rho_V = \frac{1}{\varphi_S}\left(1 - \frac{\varphi - \varphi_S}{c}\right) \tag{3.1}$$

where ρ_V is the partial specific volume of the lipid, φ is the measured density of the dispersion, φ_S is the density of the solvent (water), and c is the concentration of lipids. The densities of water at each temperature were taken from the calibration charts of the operating manual for the machine. Equation 3.2 is used to calculate the volume per lipid,

$$V_L = \frac{M_L}{N_A} \cdot \rho_V \tag{3.2}$$

where M_L and N_A are the molecular weight of the lipid and Avogadro's number, respectively. It is important to note that DMPE proved to be problematic to measure

with this technique, often a sedimentation of the DMPE liposomes was observed inside the oscillating tube. Since we were not able to verify the exact reason for this particular behaviour, the volumetric data for DMPE was taken from literature (112) and used for further data analysis.

3.2.3 Small Angle X-Ray Scattering (SAXS)

All samples were prepared by suspending lipids in ultrapure water at differing weight percentages (wt % of lipid) (Egg-PC at 40 wt%, DOPC at 40 wt%, DMPC at 25 wt% and DMPE at 20 wt%), and vortexing them at room temperature for 5 minutes until a homogenous dispersion formed. We note that all samples were prepared in excess of water; in order to optimise the SAXS counting statistics of Egg-PC and DOPC MLVs, higher weight percentages were chosen for these less ordered systems. Owing to the PEs poorer hydration properties compared to PCs, the DMPE sample was kept at 80°C for 2-3 minutes in order to facilitate full lipid hydration; upon cooling a homogenous dispersion formed. The samples were then transferred by pipette into 1 mm reusable quartz capillary holder and inserted into a temperature-controlled stage on the SAXSpace instrument (Anton Paar, Graz, Austria).

The scattering intensity is a function of the form and structure factors of the sample, expressed with the equation:

$$I(q) = \frac{S(q)|F(q)|^2}{q^2} \tag{3.3}$$

where *S(q)* and *F(q)* are the structure and form factor contributions, respectively, and *q* is the scattering wave vector modulus expressed as:

$$q = \frac{4\pi sin\theta}{\lambda} \tag{3.4}$$

where λ is the wavelength of incoming X-rays and 2θ is the scattering angle.

All scattering curves were normalised by the sample transmission and incoming flux, which was achieved by dividing each SAXS curve with the recorded attenuated direct beam intensity. Secondly, the normalised scattering contribution of the empty capillary was subtracted from all other normalised data sets. Thirdly, the pure water SAXS pattern was subtracted from the dispersion SAXS pattern. In this last data reduction step, the excluded water volume was considered (113).

All fully corrected scattering patterns were analysed according to the modified Caillé theory (MCT) (67, 68), considering both the bilayer nanostructure and membrane fluctuation. The exact analysis model and underlying grounds have been described elsewhere (70) (for an in depth review see Rappolt (58)). Parameters such as the lamellar repeat distance, *d*, and the bilayer head-to-head distance, $d_{HH,}$ are directly obtainable from the global fits. The key mechanical fitting parameter, η, known as Caillé parameter or fluctuation parameter, defines the extent of membrane fluctuation. This parameter is directly related to the mean membrane fluctuation distance, σ, via the equation (69):

$$\sigma = \sqrt{\eta}\,\frac{d}{\pi} \tag{3.5}$$

where *d* is the lamellar repeat distance. Global fitting examples of DMPC, egg-PC and DOPC sample are shown in the Appendix A (Figure A2).

We note that this global fitting procedure worked well for fully hydrated PC samples, however, it was difficult to obtain satisfactory global fits for DMPE without applying stronger fitting constraints, most probably due to the less suitable structure factor description in this case. Thus, a model free approach was applied. That is, a Fourier analysis was used to obtain the EDPs for DMPE. For centrosymmetric structures such as bilayer stacks, the Fourier summation reduces to only the cosine terms,(59) given by the equation:

$$\rho(x) = \sum_{h=1}^{h_{max}} \pm F_h \cos\left(\frac{2\pi x h}{d}\right) \tag{3.6}$$

where *h* is the order of the Bragg-reflection, *x* is the distance is real-space, *d* is the *d*-spacing, obtained from the peak positions, *q(h)*, (*q(h) = 2*π *h/d*) by linear regression, and F_h are the form factor values derived for each peak. d_{HH} was deduced from the positions of the two positive maxima in the EDP. η values for DMPE were taken from previous synchrotron SAXS studies (40). F_h coefficients were obtained by measuring the height of each peak relative to the baseline and performing the Lorentz correction. We note that for the SAXS instrument used with a beam size of 0.2 x 20 mm (this beam profile can neither be considered a perfect point nor ideal line focus), the Lorentz correction was given by the empirical value of $q^{1.5}$ (this specific correction was derived from reproducing as close as possible published EDPs of DPPC in the gel-phase (62, 97, 114); note powers of 1, 1.25, 1.5, 1.75 and 2 were tested). The

corrected intensities were square rooted. All *F(h)/F(1)* values are reported in the Appendix A (Table A1).

3.2.4 Definition of Three Distinct Water Layers

For our study, we introduce three different regions of water. Figure 3.1 shows a schematic of a single lipid and outlines thicknesses of each of its water regions: (i) the 'headgroup water' (blue), (ii) 'perturbed water' (light blue), and (iii) the 'free water' regions (light green). Note, that these highlighted regions are shown per lipid. The overall lipid length is divided into the chain length, d_C (the occupied chain volume is shown in light orange in Figure 3.1) and the headgroup thickness, D_H. The partial headgroup thickness, D_{H1}, measures the distance between the phosphate and the average hydrocarbon chain boundary. An experimentally scrutinized value was published by Nagle and co-workers, reporting D_{H1} = 0.49 nm for both PCs and PEs (37, 43, 44), which enables the deduction of the lipid chain length from the experimentally obtainable head-to-head distance, d_{HH} (i.e., the phosphate to phosphate distance). Finally, introducing a second partial headgroup length, D_{H2}, the Luzzati bilayer thickness can be expressed as a function of d_{HH}:

$$d_{LZ} = d_{HH} + 2(D_{H2} - D_{H1}) \tag{3.7}$$

For clarity, all parameters of Equation 3.7 are defined schematically in Figure 3.1 (note, since we display one lipid molecule only, $d_{LZ}/2$ and $d_{HH}/2$ are shown). The three water layer thicknesses per lipid, concerning the headgroup, perturbed and free water regions are referred to as (i) D_H, (ii) d_w^σ, and (iii) $d_w^f/2$. Note, d_w^σ is defined to be equal to σ (Equation 3.5) and appears on either side of the free water core, d_w^f. Finally, the total water layer thickness can be written as:

$$d_W = d - d_{LZ} = 2d_w^\sigma + 2(D_H - D_{H2}) + d_w^f \tag{3.8}$$

We note, that d_{HH} and d_{LZ} for PCs and PEs are not far off, i.e., they are equal to each other within 0.1-0.2 nm (37), and for a first approach estimation can be set equal. However, there is simple way to estimate this deviation $2(D_{H2}-D_{H1})$. Since the water volume in the headgroup region, V_W^H, can be described by the Luzzati method as well as by using the excluded headgroup volumes, V_H, approach, we can write:

$$(D_H - D_{H2})\, A_L = D_H\, A_L - V_H \tag{3.9}$$

where A_L is the headgroup area per lipid. From volumetric data and the EDPs it is possible to determine the area per lipid, A_L. Using the deviation of d_{HH} from d_{LZ} one arrives at the equation:

$$A_L = \frac{2V_L}{d_{LZ}} = \frac{2V_L}{d_{HH}+2\cdot(D_{H2}-D_{H1})} \quad (3.10)$$

Finally, inserting A_L from Equation 3.10 into Equation 3.9, we are able to estimate D_{H2} (see Appendix A).

$$D_{H2} = \frac{V_H\cdot(d_{HH}-2D_{H1})}{2(V_L-V_H)} \quad (3.11)$$

We note that this ansatz can be used as an alternative approach for carrying out tedious and long-lasting gravimetric measurements. Exemplary values on d_{HH}, d_{LZ} and A_L of this study are listed together with literature values in Table A2 and show very good agreement.

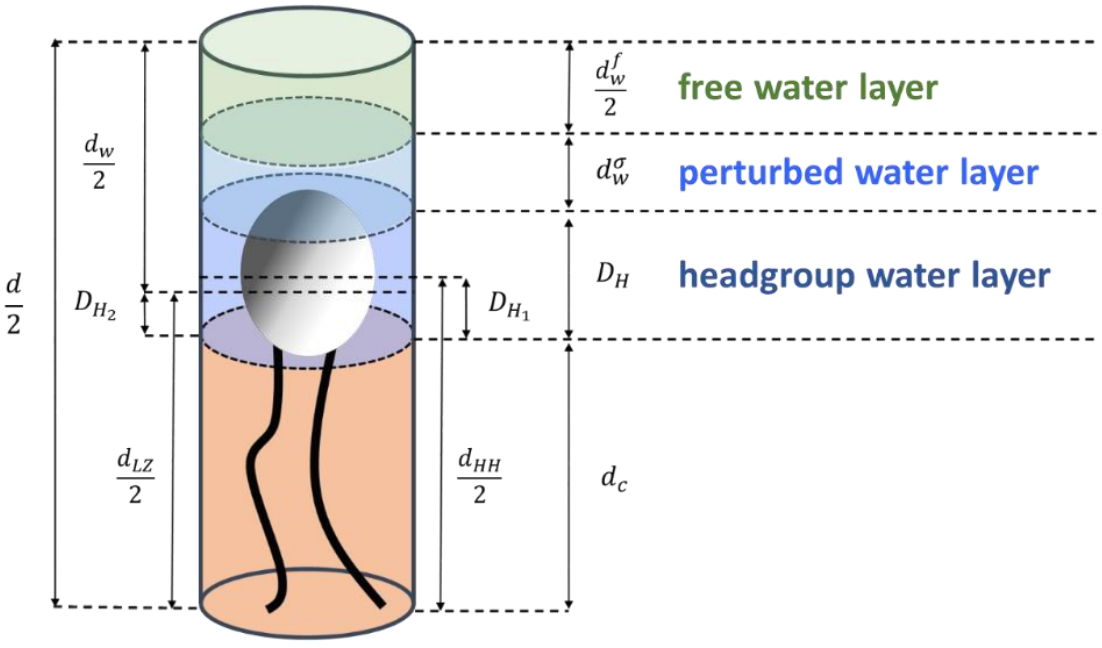

Figure 3.1 The three-water region model. A simplified lipid model is depicted in grey/black together with the distinct water layers associated with the (i) headgroup (blue), (ii) perturbed (light blue), and (iii) free waters (light green). The chain region is shown in light orange.

Specific numbers of waters per water region were calculated, dividing the partial water volumes ($A_L\cdot d_w^\sigma$ and $A_L\cdot d_w^f/2$) by the volume of a single water molecule (V_{H20} = 0.03 nm^3 (115)). The headgroup thickness D_H, was taken from literature to be 0.9 or 0.85 nm for PCs and PEs, respectively (37). D_H is dependent upon the averaged

headgroup orientational angle, this idea is investigated in more detail in section 3.3.6. Lastly, the headgroup volumes were derived from the gel-phase to be V_H = 0.319 nm^3 (37) and 0.252 nm^3 (40) for PCs and PEs, respectively.

3.3 Results and Discussion

3.3.1 Volumetric Data

The volume per lipid, V_L, was determined from the density measurements and are summarised in Figure 3.2. In all cases, a linear increase in the volume per lipid is observed as the temperature increases. The behaviour of the membrane in the fluid phase is relevant to this study, thus for Egg-PC and DOPC data were measured from 10 to 80 °C, whereas DMPC was investigated from 25 to 80 °C and DMPE from 57 to 80 °C. We note, that the melting points, T_M, for egg-PC, DOPC, DMPC and DMPE, are -15 °C, -17 °C (116, 117), 24 °C (116, 117) and 50 °C (116, 117), respectively. A higher transition temperature for DMPE of 55 °C was reported by Koynova and Hinz (112). Similarly, we observed in our SAXS experiments an abrupt lattice spacing change at 55 °C (in the heating direction the *d*-spacing decreases from 5.5 to 5.0 nm), which is in agreement with previous X-ray scattering measurements (118). In order to ensure that all samples were fully in the fluid phase, we have only included data above the main transition.

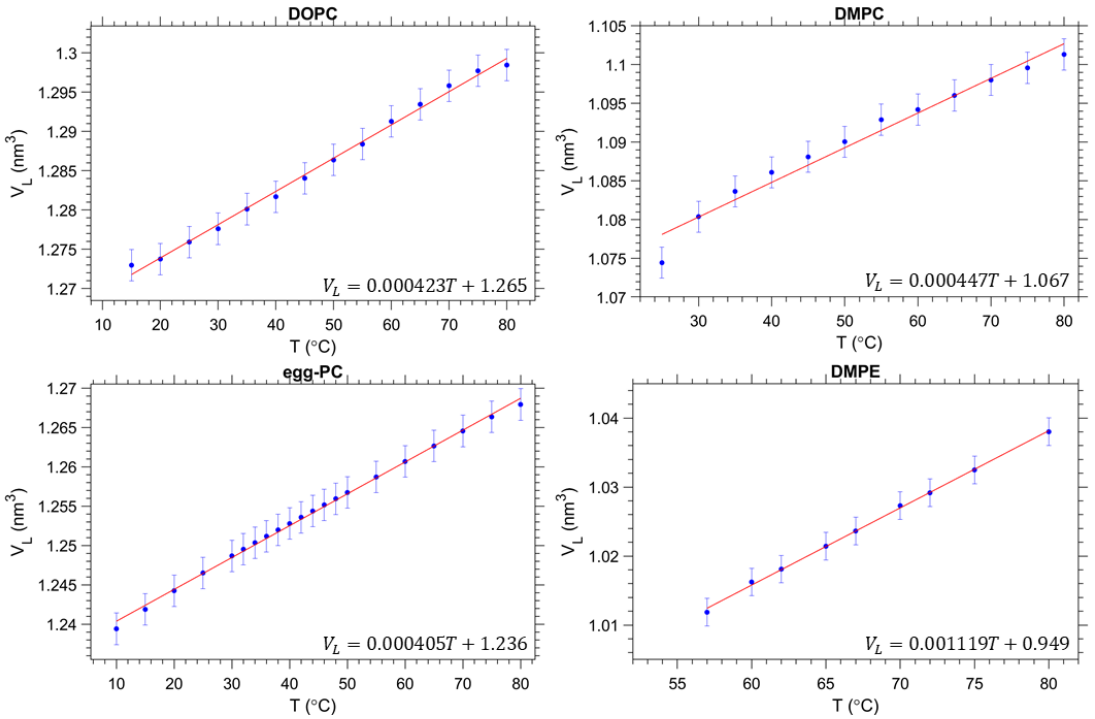

Figure 3.2 Volumetric data per lipid for each of the samples measured. Our results are in good agreement with previous studies on egg-PC (119), DOPC (120) and DMPC (121). Data for DMPE was taken from (112).

3.3.2 Overview of the Bilayer and the Three Water Regions

Data from the SAXS curves were analysed to decipher the thicknesses of the different sub-layers of the interstitial water by using Equation 3.8. The behaviour of the different layers with temperature is summarised in Figure 3.3 in schematic diagrams, showing two opposed lipid monolayer leaflets. From top to bottom the layers of the hydrocarbon chains, d_C, the headgroup extension layer, D_H, the perturbed water layer thickness, d_w^{σ}, and the free water layer thickness, d_w^{f}, are depicted. In all cases, a thinning of the bilayer is observed with increasing temperature, reflecting the extent of chain disorder. As the temperature increases, so does the thermal energy available to the chains, which undergo increasingly *trans* to *gauche* conformations (122, 123), thinning the bilayer monotonously with temperature. Whilst the bilayer itself thins, the overall *d*-spacing increases due to the dominant water layer increase, reflecting the swelling of MLVs for all PCs measured. Remarkably, for DMPE the water layer thickness slightly shrinks. That is, the water uptake is greatly reduced, when compared to the PC MLVs (the water uptake will be further discussed in Section 3.3.5). Membrane fluctuations also tend to increase with temperature as seen by the

increase in d_w^{σ} (its boundaries are given by green and blue lines). Interestingly as the fluctuations increase, d_w^{f} shrinks. This was observed in all PCs investigated. The case is very different for DMPE, where the membranes are in such close registry that the opposed perturbed water layers in fact slightly overlap; consequently, there is no free water layer apparent. For this reason, the free water boundaries (green) have been omitted in the DMPE structural data-based schematic. We note that for now we have taken the headgroup thicknesses, D_H, to be constant over the entire temperature regime; this simplification will be dropped in Section 3.3.6 and temperature dependent estimates for D_H will be discussed.

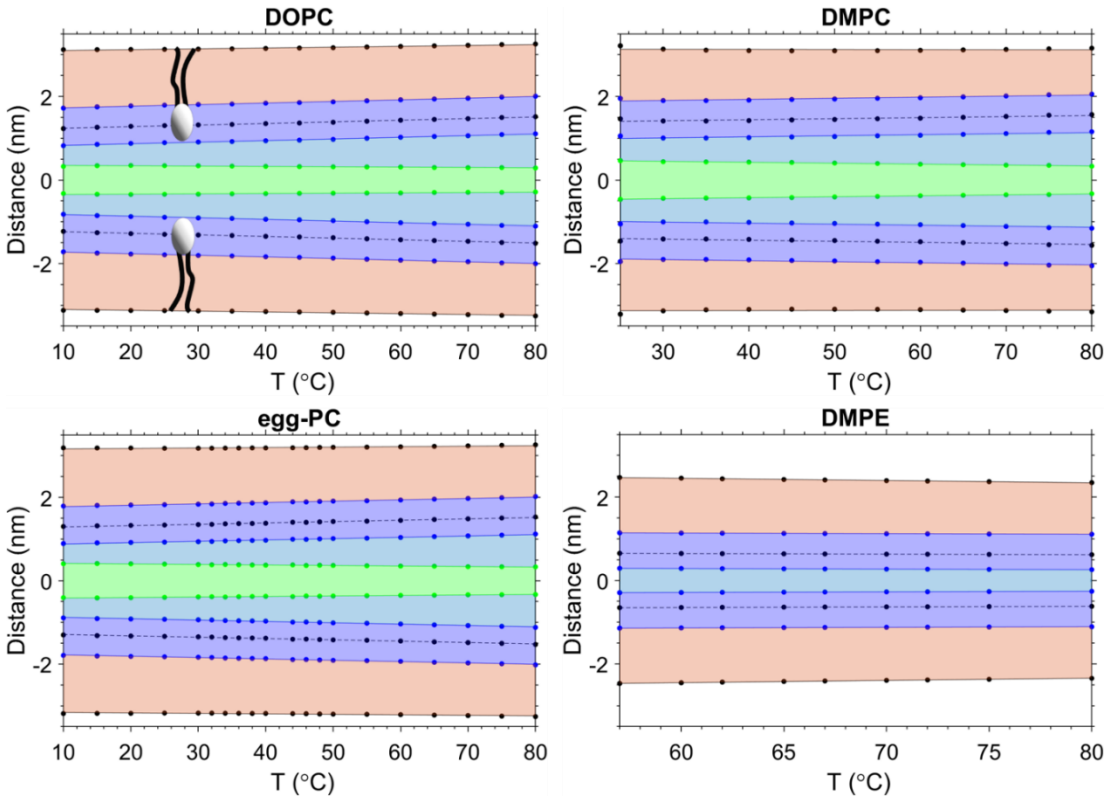

Figure 3.3 Diagrams showing the structural changes of the three water layers and two opposed lipid leaflets (light orange) as a function of temperature. The solid black lines indicate the position of the methyl trough region and the dashed black lines the position of the phosphates. The blue lines indicate inner and outer headgroup boundaries, and the light green lines indicate the boundaries between perturbed and free water regions. The three water layers are colour-coded blue (headgroup water), light blue (perturbed water) and light green (free water).

3.3.3 Headgroup Influence on the Interlamellar Water Regions

For a better understanding of the influence of the headgroup onto the planar-confined water regions, we compare DMPE *vs.* DMPC in detail. Figure 3.4 summarises the overall behaviour of the membrane and water layers as a function of

temperature. The difference between these two lipids is the presence of a choline group for DMPC and an ethanolamine group for DMPE, both conjugated to the phosphate group. Both lipids form hydrogen bonds around the phosphate group, but the hydration level in DMPC is clearly enhanced due to the three methyl groups being associated to water clathrate shells (124, 125). Cleary, the behaviour of d_w is the most apparent difference between these two lipids, and the influence of the hydrogen bonding and hydration propensity influence this. Membrane fluctuations further increase the water layer thickness in DMPC, as the repulsion between bilayers, due to the Helfrich undulations (46), does increase with the mean membrane fluctuation distance, σ (Equation 3.5). As seen in Figure 3.4b (middle panel), the perturbed water layer thickness, d_w^{σ}, of DMPE instead is very constrained, not changing by more than tenth of a nanometre over the entire temperature range. That is, the membrane fluctuations are far less noticeable, when compared to DMPC. This is coupled with the diminished ability to retain water between the bilayer and near the headgroup (125). Further to this, the perturbed water layer is relatively small, leaving very little interstitial water between adjacent membranes, leading to an extreme close registry of adjacent membranes. Most remarkably, is the apparent absence of a free water layer in DMPE. This is markedly different for the case of PCs; coupled to a greater repulsion force acting on DMPC membranes, the MLVs do swell significantly at higher temperature. Nonetheless, the free water layer thickness (Figure 3.4b, top panel) decreases with temperature for DMPC, since the water up-take is greatly dominated by the 'perturbed water' layer increase.

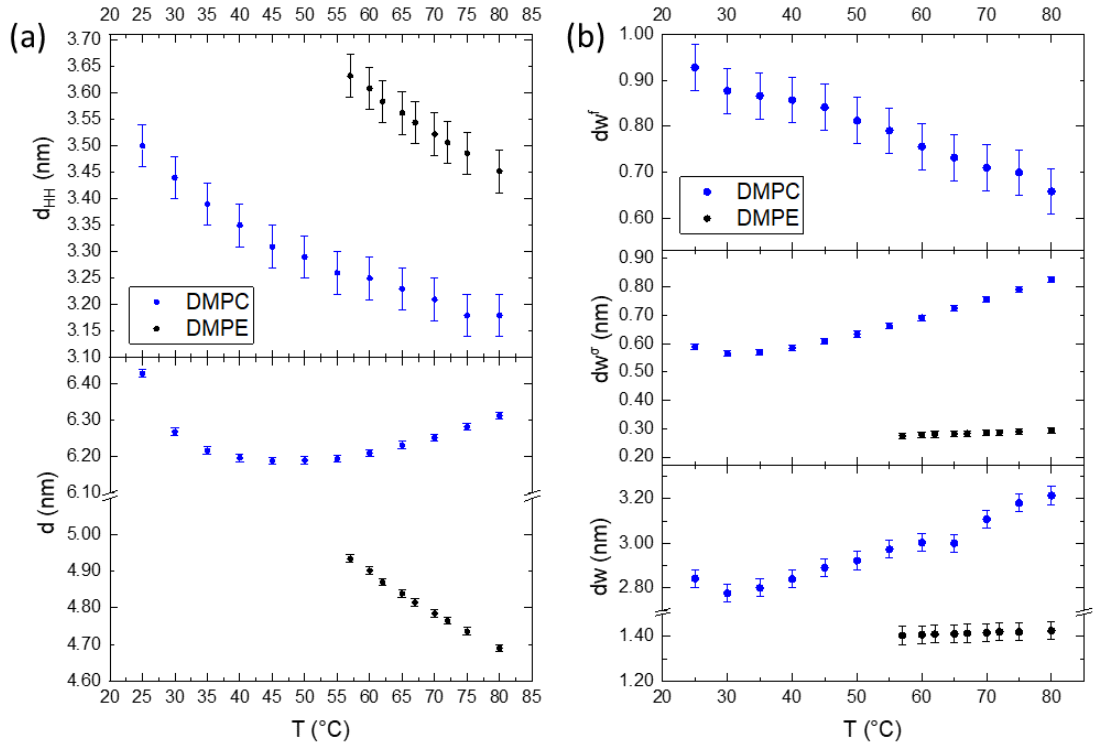

Figure 3.4 Structural parameters of DMPE and DMPC. a) Behaviour of the bilayer thickness, d_{HH} (top) and overall *d*-spacing (bottom) as a function of temperature. b) The thickness of the free water layer (top) and perturbed water layer thickness (middle) and the overall water layer thickness (bottom).

Taking a closer look to Figure 3.4a, we can clearly see that the bilayer, d_{HH}, shrinks upon heating in both cases. This is expected as this is mainly dominated by the hydrocarbon chains, which become more disordered as the temperature increases, transferring from *trans* to *gauche* states (123). Both lipids have the same fully extended, *all-trans* state chain length of 1.63 nm, as outlined by Seelig and Seelig (123) (note, here d_C is defined as (N_C - 1) · 0.125 nm, with N_C being the number of hydrocarbons and 0.125 nm being the chain-projected C-C bond length). At 80 °C this value reduces by 0.39 nm and 0.53 nm for DMPE and DMPC, respectively, which would amount to four effective *gauche* states per chain for DMPC and three effective *gauche* states for DMPE. We note, as described in the common brush model (53, 126), the membrane bending modulus, K_C, is proportional to the squared membrane core thickness, $(2d_C)^2$, as well to the area compression modulus, K_A (126),:

$$K_C = K_A\,(2\,d_C)^2/24 \qquad (3.12)$$

Where the term $2d_c$ represents the "deformable" membrane thickness. Equation 3.12 arises from the consideration of a simple elastic sheet (monolayer), the area

expansion of a region within the sheet is related to the change of the arc lengths based on the two principal curvatures as well as the regions distance from the mid-plane. The volume expansion then, is related to the area expansion and the thickness of the region of interest as well as the elastic properties represented by K_C and K_A. Therefore, the energy of expansion across the entire thickness of the simple elastic sheet is proportional to the elastic constants, K_C and K_A. For two simple elastic sheets forming a bilayer, the energies are summed. It is important to note that the brush model does not consider energetic contributions resultant from lipid headgroup interactions. The model stipulates that changes in surface pressure derive from the free energy changes in the chain region (see appendix in reference (126)). However, more detailed elastic free energy models which consider headgroup interactions as well as energetic cost of tilt elasticity have been developed (127). Never the less, we apply the simple brush model in this case because of its effectiveness at predicting the relationship between elastic constants and membrane thicknesses for the lamellar phase (126). Hence, the influence of the bending modulus on the mean fluctuation distance, σ^2, is inversely proportional to the 'deformable' membrane thickness (note, $\sigma^2 \propto \eta \propto 1/\sqrt{K_C} \propto 1/(2d_C)$ (9, 69)). In simple words, thicker membranes are expected to fluctuate less, leading to a thinner perturbed water layer d_w^{σ}. The results obtained for DMPE are understood through the brush model, where the membrane is thicker compared to DMPC, therefore the fluctuation distance is shorter. Studies to experimentally measure the bending modulus in DMPE and DMPC have produced varying results(128-131), but a recent simulation study (132) determined the bending modules, K_C, for DMPE at a value of 22 k_BT compared to 14 k_BT for DMPC, implying stiffer DMPE membranes. Considering the *d*-spacing, we see that PC MLVs swell, whilst PEs slightly shrink as a function of temperature, which is in this picture is generally understood on the basis of the differing mechanical properties of the membranes.

The Helfrich undulation force depends on the membrane bending modulus as well as the interstitial water layer thickness. However, at small water layer distances (0.4 to 0.8 nm) the repulsive hydration force is dominant, which decays exponentially with d_W (133, 134). Across all bilayer separations, the Van der Waals (VdW) attractive force competes with the two aforementioned repulsive forces, and ultimately, this

balance of forces determines the adjacent membrane distance, d_W. The attractive VdW force is proportional to the Hamaker constant, which is related to the static dielectric permittivity of the aqueous medium. Changes in the density across the aqueous medium will influence the dielectric permittivity and therefore influences the strength of attraction between adjacent membranes. In general, a decrease in water density decreases the permittivity, which alters the dielectric contrast influencing the Hamaker constant (for a review see chapter 13 in Israelachvili's book on 'Intermolecular and surface forces' (135)). Considering the density changes across the water layer, it is plausible that the water density is slightly different in each of the defined sub-layers (Figure 3.1), due to the influence of the membrane undulations and the degree of headgroup hydration. The orientational ordering of water around the headgroup dipole increase the strength of the interfacial electric field which also contributes to the decrease in relative permittivity. These supposed water density differences mean that the permittivity is non-uniform across d_W, therefore, in a refined description of the VdW force, the Hamaker constant should be considered to change as a function of distance from the polar/apolar interface. The area per lipid also needs to be considered in the strength of the Hamaker constant. For instance, an increase in the area per lipid decreases the effective surface charge density (deceasing the strength of the interfacial electric field) in the headgroup region. Consequently this increases the (relative) dielectric permittivity in the interfacial (headgroup) water region (136-138). Similarly, the ordering of water molecules close to the membrane interface (within the Stern layer) will diminish as a result of the weakened electric field, resulting in an increase in relative permittivity (139). This increase in permittivity affects the strength of the VdW interaction allowing the water spacing to increase, which is observed in the swelling of PC MLVs.

Similar arguments, but with opposite effect, apply for VdW force in DMPE. In the absence of a free water layer (when only the perturbed, less dense water is apparent) a relative decrease in dielectric permittivity of its interstitial water is expected, hence a greater overall Hamaker constant. In contrast to PCs, the dominant repulsive force is not the Helfrich undulation force; the water hydration force is dominant at such small membrane to membrane distances (125, 140). Remarkably, the very low d_W in PE systems has long puzzled the scientific community (43, 45). In

1982, Lis et al. considered an increase in the attractive VdW pressure explaining the smaller equilibrium spacings in PE systems but actually reported on too large d_W values. This led to other research groups assuming other additional attractive forces in order to overcome the repulsive hydration force in PE membrane stacks. The idea of a solvent-mediated attraction force found some attraction (see references (45, 125) and therein). It has been argued that a small fraction of direct electrostatic and/or indirect hydrogen-bonded water interactions between the NH_3^+ group in one membrane and the PO_4^- group in the opposing membrane could account for the additional interaction in PE bilayers.

3.3.4 Hydrocarbon Chain Saturation Influence on the Interlamellar Water Regions

Figure 3.5 compares the effect of the hydrocarbon chain and degree of saturation for DMPC, DOPC and egg-PC. All lipids possess the same choline-tipped headgroup. DMPC is fully saturated (C14:0 chains), DOPC has monounsaturated chains (C18:1) and egg-PC is a mixture of lecithins, both with saturated and unsaturated PCs (mostly C16:0 and C18:1) (141). In general, across all the parameters described, the hydration behaviour is the same, in that water layer thicknesses increase with temperature as the liposomes swell under the influence of the increasing Helfrich undulation force. The unsaturated chains in DOPC and egg-PC make them more susceptible to chain splay and hence chain disorder, however, their effective chain length is bigger than for DMPC. Hence, the DMPC bilayers are actually thinner, while DOPC and egg-PC bilayers display similar d_{HH} values (Figure 3.5a, bottom). According to the brush model (see Equation 3.12), the membrane rigidity is not only influenced by the chain fluidity and hence its lateral compressibility modulus, K_A, but more strongly to variations in the 'mechanical' membrane thickness. We note, that K_A does not vary much among PCs containing C14:0, C18:0, C18:1 and C18:2 hydrocarbon chains (126), which are predominantly also found in eggPC. Thus, with eggPC and DOPC having significantly bigger bilayer thicknesses than DMPC (Figure 3.5a, top), one would expect this to be reflected in a lower membrane rigidity of DMPC bilayers. However, Doktorova et al. pointed out that the classical brush model is not equally applicable to fully saturated lipids, when compared to lipids with unsaturated chains (35). Evidence is put forward that the 'mechanical' or 'deformable' thickness is relatively bigger for saturated lipids

(coming close to d_{HH}), whilst being close to $2d_C$ for unsaturated lipids. Thus, similar 'mechanical' membrane thicknesses among eggPC, DOPC and DMPC would explain similar values in d_w^{σ}. Indeed, our determined η values (Caillé fluctuation parameter) for the studied PCs do not vary much and are in good agreement to literature values, when comparing identical hydration conditions at 30 °C (DMPC: 0.080 compares to 0.077(129); DOPC: 0.081 to 0.095(120) and eggPC: 0.073 to 0.088(69)). Finally, the deviation from a linear water layer thickness trend in DMPC (see 25-30 °C interval), is explained by the effect of anomalous swelling just above the melting point of DMPC (129, 142), where the coexistence of gel-like domains in the fluid lamellar bilayer lead to a drop in both the bending rigidity and the bulk compression modulus. The anomalous swelling regime in DMPC also explains the local minima in the recorded *d*-spacing of DMPC at about 40 °C; while the bilayer thickness monotonously decreases, the MLVs do swell near the melting point as well as at high temperature.

As mentioned before for DMPC, the trend in the free water layer spacing (Figure 3.5b top panel), is opposite to the dominant increase in the perturbed water layer for all PC samples. At lower temperatures the equilibrium distance between adjacent bilayers, d_W, ranks in the order of DMPC > egg-PC > DOPC, most probably reflecting the reverse order of deformable membrane thickness, which in turn dominates the strength of the Helfrich undulation forces. The same ranking in thickness is found for the free water layer thickness.

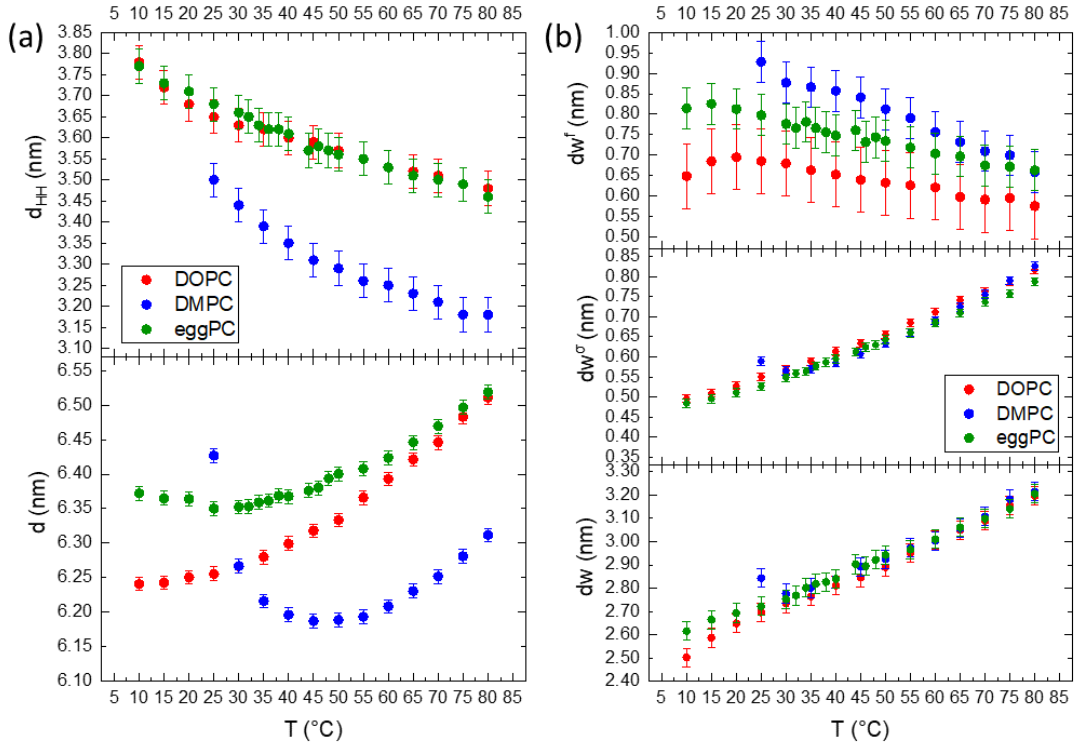

Figure 3.5 Structural parameters of DMPC, egg-PC and DOPC. a) Temperature trend of the bilayer thickness, d_{HH} (top), and d-spacing (bottom). b) Thickness of the free water layer (top), the perturbed layer (middle) and overall water layer thickness (bottom) as a function of temperature.

3.3.5 Number of Water Molecules in the Three Water Regions

The area per lipid shows a general increase with temperature (Figure 3.6a). DOPC obtained the largest area, owing to the relatively highest disorder in the hydrocarbon chain, arising from the two monounsaturated oleic acid chains (C18:9). DMPE has the lowest area per lipid, which is understood due to its relatively small headgroup, and coupled to it, the relatively lowest disorder in the hydrocarbon chain region caused by the lowest number of *gauche* conformers per saturated myristic acid chains (see discussion in Section 3.3.3). Another major difference of DMPE MLVs is the fact that they do not swell as compared to PC MLVs. An entirely different balance of forces and poor hydration does explain this exceptional behaviour of the fluid lamellar phase of PEs (see discussion in Section 3.3.4). In this section, we take a closer look onto the number of waters in the different water regions.

First, the total number of waters per lipid for DOPC, egg-PC, DMPC (n_W = 33, 32 and 24 at 30 °C, respectively) and DMPE (n_W = 12 at 60 °C) are in excellent agreement with literature values (37, 143) (see Table A2 in Appendix A). Second, a recent small angle

scattering model, introducing a fixed hydration shell to the headgroup for improving the quality of fits at lower scattering angles, report on waters per headgroup to be 10-13 of saturated PCs and 16 for loosely-packed monounsaturated PCs (100). More specific values are reported by John Nagle's lab (see reference (87) and therein) for DMPC (n_W^H = 7 at 30 °C), egg-PC (n_W^H = 10 at 30 °C), DOPC (n_W^H = 11 at 30 °C), and for dilauroyl phosphatidylethanolamine, DLPE (n_W^H = 6 at 35 °C). Note, to the best of our knowledge, there is no published literature value of n_W^H for DMPE available, but having the same headgroup and being only two hydrocarbon chains shorter, DLPE n_W^H values are expected to very similar to those of DMPE. Thus, all published n_W^H values are in excellent agreement with obtained values in this study (Figure 3.6b). In further detail, the (i) number of headgroup waters, the (ii) number of perturbed waters, and the (iii) number of free waters all depend on the trend of A_L and their layer thicknesses, D_H-D_{H2}, d_W^σ and $d_w^f/2$ (Figure 3.6b-d). Noteworthy, the number of total water molecules per lipid, the water molecules per headgroup and per perturbed regions do display all the same trend, i.e., DOPC > egg-PC > DMPC > DMPE. That is, they are dominantly influenced by the area per lipid, A_L. However, the number of free waters displays the opposite order and are - as noted above - dominated by their extension, $d_w^f/2$, which decreases from DMPC > egg-PC > DOPC. For DOPC, the free layer does not change its number of water molecules by a significant amount (less than 1), when compared to egg-PC and DMPC. DOPC also has the lowest gradient for n_w^f against temperature; -0.0048 °C^{-1} compared to -0.011 and -0.025 °C^{-1} for egg-PC and DMPC, respectively. These imply that the free layer of DOPC remains essentially constant over the whole temperature range. This interpretation, as well as the apparent lack of a free layer in DMPE, are used in the next section to roughly estimate the temperature dependent headgroup extension D_H.

A final remark shall be given with respect to confined water in non-planar lipid self-assemblies. While this study focusses on planar confined water, the three-water layer model is also applicable to confined water near curved membranes interfaces. Indeed, we have completed a study on the inverse hexagonal phase in greater detail (see Chapter 4) and would like to herald that it is feasible to introduce the distinction between 'perturbed' and 'free' water regions in this case. Nonetheless, the situation

is more complex, since the mechanical behaviour along the membrane/water interface is not constant in the inverse hexagonal phase, but depends on the locally varying membrane stress (compression vs. decompression zones), which do induce local changes in the thickness of the perturbed water layer.

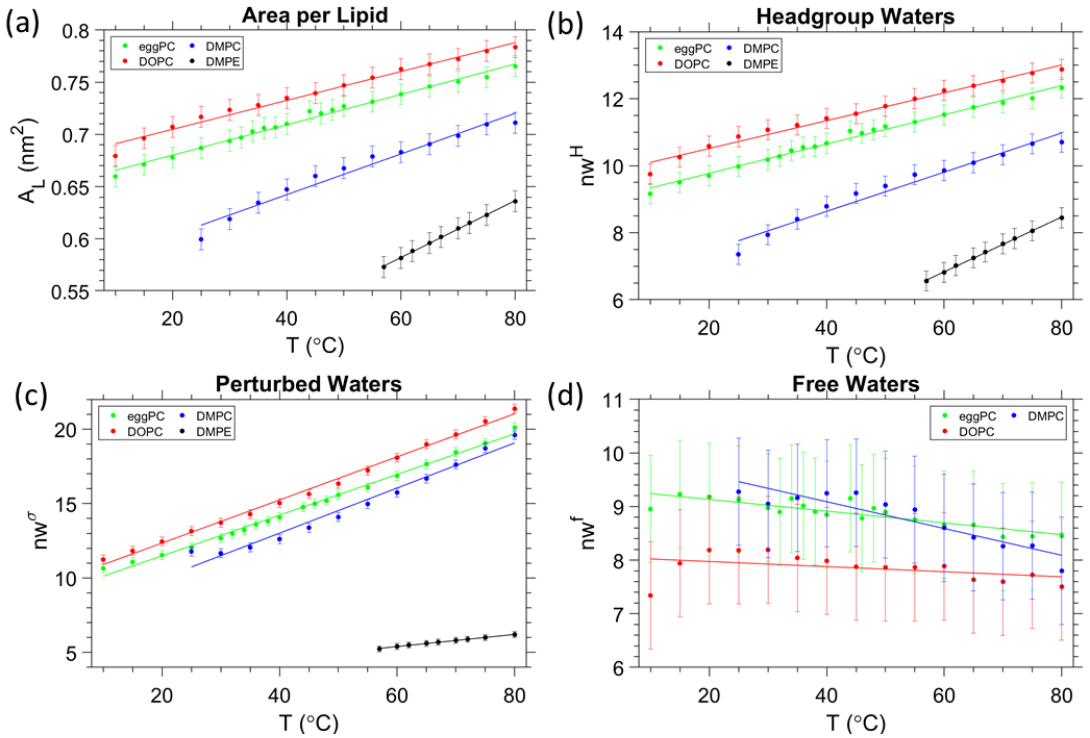

Figure 3.6 Hydration properties of DMPC, egg-PC, DOPC and DMPE. a) Area per lipid. b) Number of waters in the headgroup region. c) Number of waters within the perturbed water region, and d) number of free waters.

3.3.6 Refining the Headgroup Extension

From the estimation of the number of water molecules present in each sub-layer of the confined water strip, a picture of each sub-layers behaviour begins to form. Equation 3.8 can be further utilised for the cases of DMPE and DOPC. Here we actually observe that the free water layer thickness in DMPE is practically zero (we note, occurring negative values make no physical sense) and in DOPC the free water layer thickness is constant within error. Thus, our hypothesis is that the apparent trend seen in $d_w^f/2$ may actually be caused by a temperature dependent headgroup extension, D_H, instead. Our reasoning for this is that the glycerol backbone of the headgroup is commonly assumed to be of constant thickness (144-147), however, the region between the phosphate and tip of the headgroup is more likely to flex and

reorient as demonstrated with NMR measurements(148, 149) as well as shown theoretically and by MD simulations (137, 150).

Starting with DMPE after setting the free water layer to 0 (indicative of the results from SAXS, Figure 3.3) and rearranging Equation 3.8 for $D_{H,}$ we can see that the vertical headgroup extension thins as the temperature increases due to an increase in the tilt angle of phosphate to tip of the headgroup moiety (see Figure 3.7). At the onset of the melting temperature, D_H is equal to 0.86 nm, which is in good agreement with previously reported values (37). This value then decreases to 0.82 nm at 80°C. This thinning of the headgroup extension is understandable, when considering the trend of A_L that increases with temperature, meaning the headgroup would need to occupy a larger surface area. The headgroup therefore reduces the apparent thickness of D_H-D_{H1} by reorientation of the phosphate to tip of the headgroup extension towards the membrane plane.

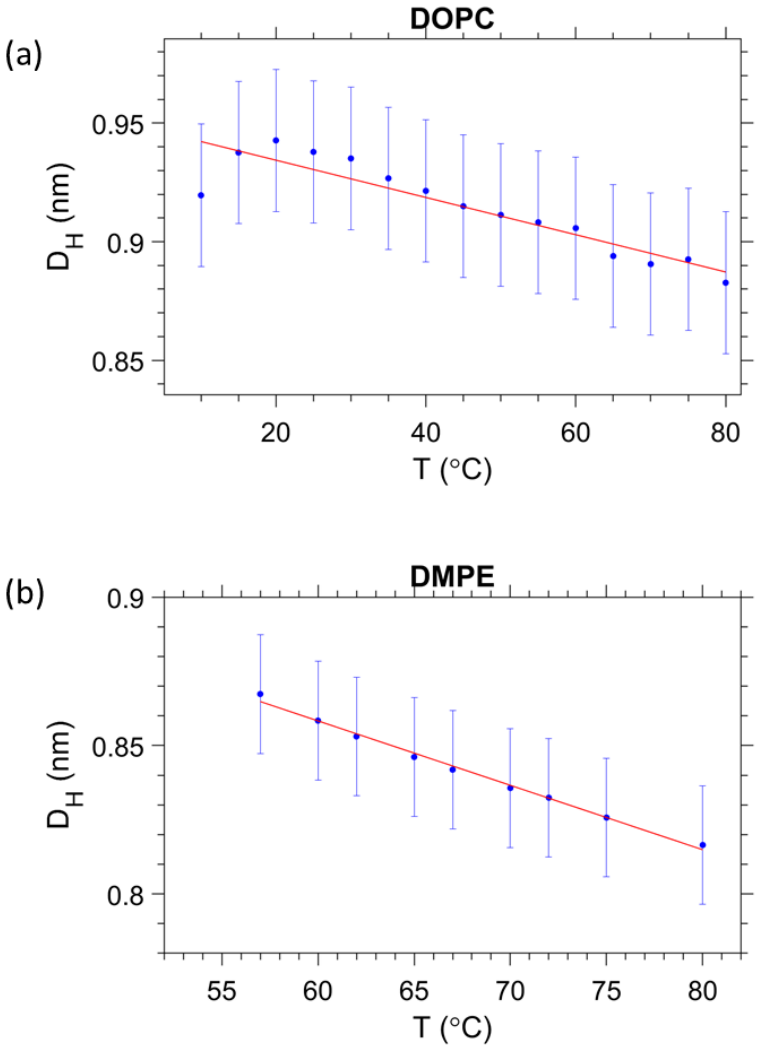

Figure 3.7 Estimation of the temperature dependent headgroup extension D_H for a) DOPC and b) DMPE, respectively.

In a similar manner, we have set the free water layer for DOPC to a constant value, averaged from high temperature data values obtained in Figure 3.5b (top panel). The first values for D_H are slightly higher than 0.9 nm, but this is never the less in good agreement with the previously reported values (37). The reduction of headgroup thickness is explained in the same way as for DMPE, whereby the increase in area per lipid is compensated with a thinning of the apparent headgroup thickness, D_H. The assumed temperature dependence of D_H, slightly alters the number of headgroup waters, which in this scenario do not change by more than a single water molecule. The refined hydration changes are summarised in the Appendix A (Figure A3).

3.3.7 Estimation of the Headgroup Tilt

Having obtained a linear regression for the headgroup extension, we can now attempt to estimate its tilt angle. Note, we follow the same assumption as before that the glycerol backbone thickness, D_{H1}, is constant, leaving the portion between the phosphate and the tip of the headgroup to flex and re-orientate. The headgroup thickness, D_H, is a projection of the physical extension of the headgroup to the bilayer normal. Thus, to calculate the headgroup tilt angle, it requires the knowledge of the reference length given by the physical distance from the phosphate to the tip of the headgroup, $D_{H\ ref}$. For PC and PE we use the literature value of 0.47 nm as the phosphate to nitrogen distance (151) and known bond lengths (152) as well as bond angles (153), concerning the N-C, C-H and N-H bonds found in the choline and ethanolamine headgroups. This results in $D_{H\ ref}$ = 0.68 nm and 0.63 nm for PC and PE, respectively (Figure 3.8b). The tilt angle, θ_{Tilt}, is then given by:

$$\theta_{Tilt} = \cos^{-1}\left(\frac{D_H - D_{H1}}{D_{H\ Ref}}\right) \tag{3.13}$$

Utilising the obtained headgroup thickness, $D_H(T)$ (Figure 3.7), we are able to calculate the tilt angle as a function of temperature, and further able to illustrate how much of the area per lipid, A_L, is occupied from the precession of the headgroup. The results are summarised in Figure 3.8.

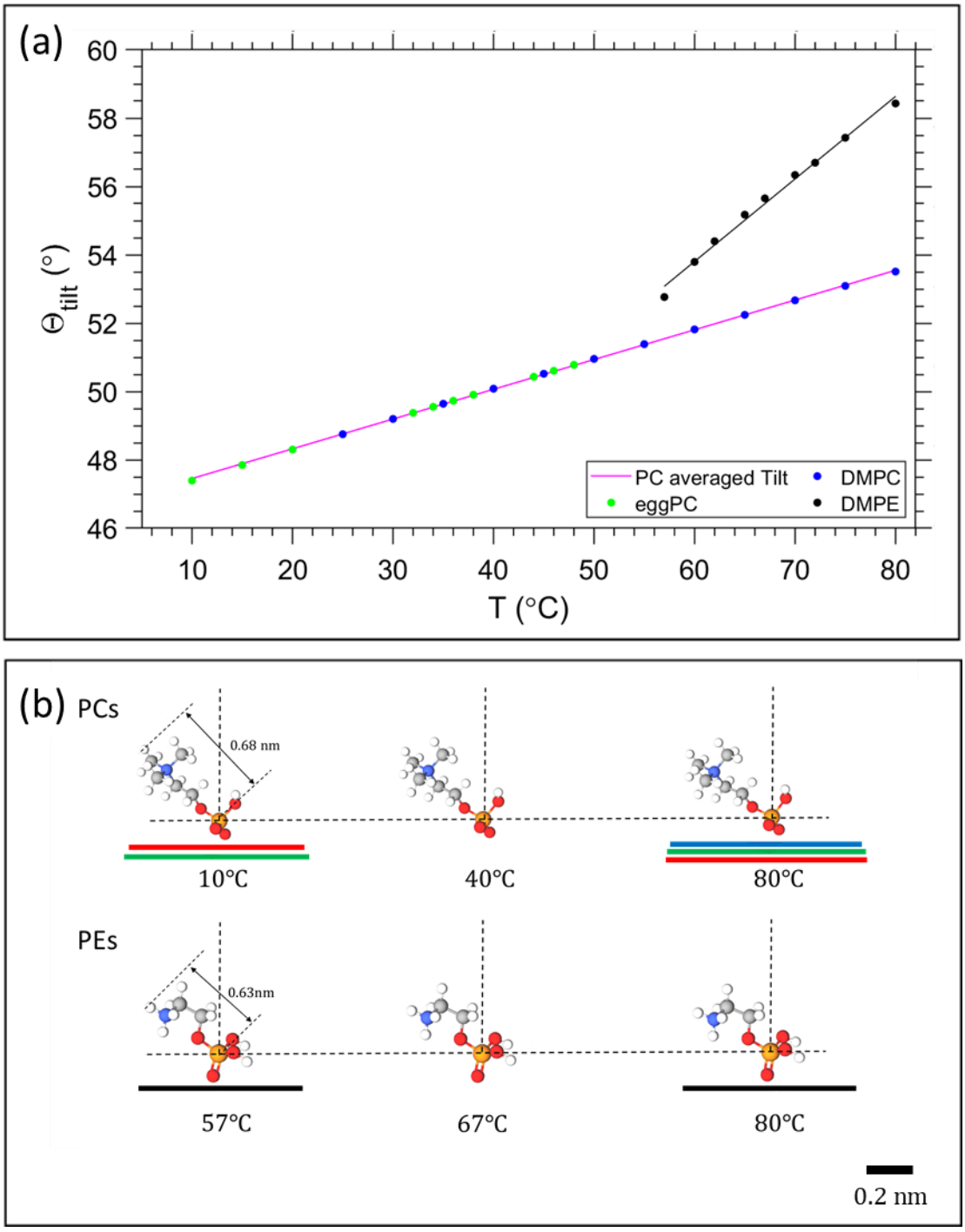

Figure 3.8 Temperature dependent headgroup orientation. a) Tilt angle as function of temperature for PCs and PEs. b) Orientation of the headgroups (P-N axis) of PCs and PEs with respect to projected extensions of A_L (red –DOPC; green – egg PC, blue – DMPC; black DMPE). As shown from left to right the tilt angle increases with temperature, with the P-N axis orientation coming closer to the membrane plane. Molecular models were made with MolView (http://molview.org). All schemes are referring to the same scale bar of 0.2 nm.

From Figure 3.8a, it is clear that the tilt angle increases with temperature, implying that the headgroup tends towards a more horizontal position relative to the bilayer.

This result is unsurprising, considering that the area is expanding, whilst the bilayer is thinning and the volume per lipid increases. Theoretical studies and MD simulations confirm that the lipid headgroups tend to a more horizontal position due to thermal movements (rotation), which is more intense at higher temperatures.(137, 150) The pink line in Figure 3.8a represents the averaged linear regression from all the PCs studied; note, all the data points display the same linear trend, since only one linear regression of D_H was applied. DMPE displays a stronger tilt angle, which is to be expected, when considering the proximity of adjacent PE bilayers. Figure 3.8b, illustrates how the headgroup tilt angle goes hand in hand with the trend in A_L. The planar projection of the headgroup length, $D_{H\,ref}$, superimposes well with the lateral radius per lipid, $\sqrt{(A_L/\pi)}$.

3.4 Conclusions

We have introduced a three-water region model, while commonly only two water regions are considered, i.e., headgroup and interlamellar water. In our model, the interlamellar water region is further divided into free and perturbed water regions, which can be forthrightly determined, when the bilayer nanostructure as well as membrane fluctuations are known. Applying this approach, we have revisited the fluid lamellar phase of PCs and PEs, and particularly chosen these two key lipid species, since they are displaying an extremely different hydration behaviour. Applying this new three-water region model, the following achievements have been made:

- We are able to estimate the 'Gibbs dividing surface' without the need of gravimetric measurements. That is, we are able to estimate the Luzzati bilayer thickness, d_{LZ}.
- We are providing all standard structural membrane parameters, such as d_{HH}, d_C, A_L, and V_L.
- We give a detailed description of three-water layers and the water numbers per region.

- We provide a rough estimate of the temperature dependent headgroup extension, D_H, and its tilt angle.

The presented three-water region model will help to refine existing membrane force descriptions, in particular when revisiting existing models on the attractive Van der Waals forces. Note, we expect that the Hamaker constant, H, to be different in the perturbed and free water layer extensions, with $H_{perturbed}$ being greater as H_{free}. The latter notion is in agreement with the extreme differences found for the equilibrium distance of adjacent membranes in PC and PE MLVs, respectively. Finally, due to the refined description of the confined water regions and their temperature behaviour, ('headgroup' and 'perturbed' water numbers increase with T, while 'free' water numbers display a small decreasing temperature dependence), we are able to provide more detailed lipid/water data sets for future refined molecular dynamics simulations.

Chapter 4 From Angular to Round: In Depth Interfacial Analysis of Binary Phosphatidylethanolamine Mixtures in the Inverse Hexagonal Phase

Abstract

Packing stress in the lipidic inverse hexagonal H_{II} phase arises from the necessity of the ideally cylinder-shaped micelles to fill out the hexagonally-shaped Wigner-Seitz unit cell. Thus, hydrocarbon chains stretch towards the corners and compress in the direction of the flat side of the hexagonal unit cell. Additionally, the lipid/water interface deviates from being perfectly circular. To study this packing frustration in greater detail, we have doped 1-palmitoyl-2-oleoyl-*sn*-phosphatidylethanolamine (POPE) with increasing molar concentrations of 1,2-palmitoyl-*sn*-phosphatidylethanolamine (DPPE: 0 to 15 mol%). Due to its effectively longer hydrophobic tails, DPPE tends to aggregate in the corner regions of the unit cell, and thus, increases the circularity of the lipid/water interface. From small angle X-ray diffraction (SAXD) we determined electron density maps. Using those, we analysed the size, shape and homogeneity of the lipid/water interface as well as that of the methyl trough region. At 6 and 9 mol% DPPE the nanotubular water core most closely resembles a circle; further to this, in comparison to its neighbouring concentrations, the 9 mol% DPPE sample has the smallest water core area and smallest number of lipids per circumference, best alleviating the packing stress. Finally, a three-water layer model was applied, discerning headgroup, perturbed and free water, demonstrating that the hexagonal phase is most stable in the direction of the flat faces (compression zones) and least stable towards the vertices of the unit cell (decompression zones).

4.1 Introduction

Hexagons represent an omnipresent class of polygons throughout nature: on the nanoscale, hexagonal close packed crystal structures are present for many different elements with Mg and Co coming the closest to the ideal cell axial ratio c/a of 1.633 (154). On a slightly larger scale, lipid self-assemblies display various pathways for formation of hexagonally closest packed cylindrical micelles (155-157), on the macroscale it has been the shape of choice in the construction of beehives. Larger still are the rock formations, which adopt hexagonal columns at the Giants Causeway, and even larger, is the hexagonal storm situated at Saturn's north pole (158, 159). The major intrinsic property of regular hexagons, which allows them to be used so seamlessly and efficiently throughout the natural world, is the hexagons' proclivity for closest packing in two dimensions. Already two millenniums ago, Pappus of Alexandria (~290 to 350 A.D.), a Greek mathematician, expressed this in the honeycomb conjecture that 'any partition of the plane into regions of equal area has a perimeter at least of that of a regular hexagonal grid', but it took until 2001 until this conjecture could be finally proved (160).

Focussing on self-assembled lipid aggregates, particularly phospholipid-based membranes, the fluid lamellar L_α phase is the biologically most relevant for modelling and understanding the behaviour of the cell wall (37, 58). Nonetheless, non-lamellar phases are of interest due to the formation of cubic membranes in biological systems, which can develop under protein alterations, drug intervention or stress (161, 162), and due to their importance in fusion-related processes (for a review see(163)). Cylindrical-shaped membranes play a crucial role in local and transient steps of membrane fusion (164, 165). It has been proposed that cylindrical-shaped micelles form within the L_α phase, either by fusion of inverted spherical micellar intermediates (IMI) (166), or alternatively, apposing IMIs may seed line-defects (167), inducing the formation of inverted micellar rods (for a review see (163)). Furthermore, tubular intercellular connections could be identified in cell-to-cell communication (168).

Aside from possible biological implications this system delivers, e.g., using lipid extracts (26), the inverted hexagonal phase is widely studied for drug delivery of

antivirals and other bioactives (169-174). Practical use has been made from the inverted hexagonal phase for the determination of the spontaneous monolayer curvature of various amphiphilic molecules (175) as well as a detailed structural model now allows for the global fitting of small angle scattering patterns of the H_{II} phase (176).

The inverted hexagonal H_{II} phase as a model system has been widely studied (63, 71, 164, 177-179), and is characterised by a high lipid/water interfacial curvature perpendicular to the long axis of the cylinder-shaped micelles arranged on a hexagonal lattice (Figure 4.1A). Non-lamellar lipids with relatively small interfacial head-group areas (Figure 4.1B), such as phosphatidylethanolamines (PE) with a non-zero spontaneous curvature, induce membrane curvature towards the water phase, which constitutes the driving force for the L_α to H_{II} transition. Comparing the critical packing parameters at a given temperature of various PEs (31, 63, 156), demonstrates that the formation temperature, T_H, for the inverse hexagonal phase decreases linearly with the degree of chain splay (Figure 4.1C). Furthermore, the packing of the lipid nanotubes on a hexagonal grid allows for the closest packing of the inverse lipid cylindrical micelles. Considering the crystallographically used oblique unit cell description for the hexagonal lattice (a = b and γ = 120°), it is helpful to also employ the hexagonal Wigner-Seitz unit cell, when describing the packing frustration within the H_{II} phase (Figure 1A). As can be easily demonstrated (180), an inscribed circle to the Wigner Seitz cell only covers 91% of the area, that is, 9% of interstitial area is unaccounted for. Thus filling out the hexagon with inverted columnar micelles is accomplished firstly by a deformation of the ideally circular lipid/water interface, and secondly, the lipid chains must stretch and compress around the quasi-circular water core in order to fill the unit cell, leaving no void space in the interstitial regions (decompression regions). Note, the radius defining the position of the phosphates, R_P, is the longest, when pointing towards the vertices of the hexagon and the shortest, when oriented perpendicular to the flat side. This stretching and compression of the hydrocarbon chains (Figure 4.1A, top right), as well as the deformation of the lipid/water interface, comes at an energetic cost known as the 'packing frustration' (181-183). Interestingly, only when lipid-shape anisotropy is

taken into account (Figure 4.1B), the overall correct interfacial shape can be simulated, hereby determining the appropriate relationship between the bending deformation and stretching of hydrocarbon chains (71, 184, 185).

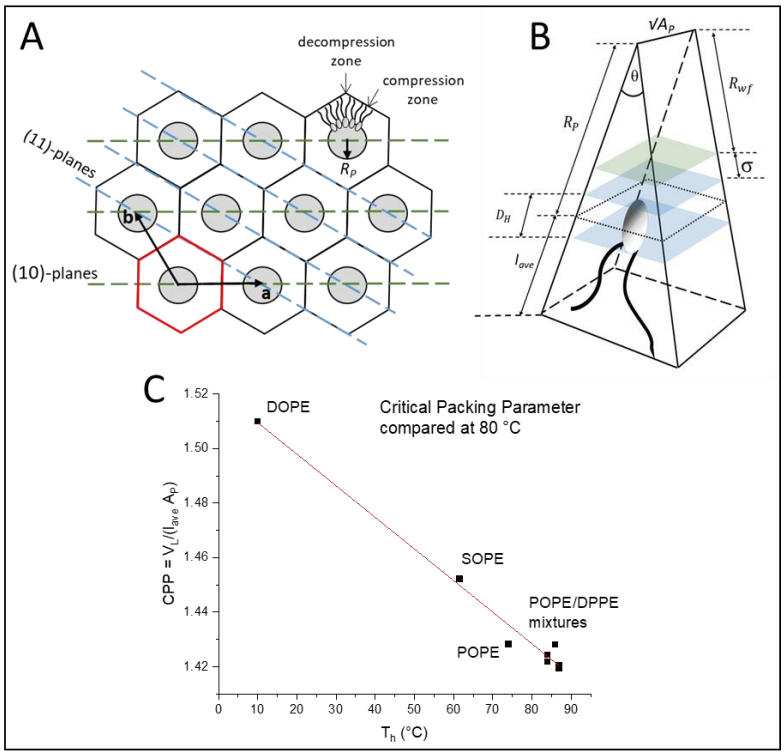

Figure 4.1 (A) Illustration of the hexagonal lattice with unit vectors ***a*** and ***b***. The Wigner Seitz cell is shown in red. Monolayers of lipids align around the water cores (grey circles). The lattice planes in the <10> direction (green) and in the <11> direction (blue) are shown (B) A schematic of a single lipid encased in a wedge geometry. The black dotted line indicates A_p. The volume encased by the two blue planes depicts the headgroup region. The green plane indicates the fluctuation distance, σ. R_{wf} is the radius related to the free water region. Note, the wedge has a depth of vA_P. (C) Critical packing parameter (CPP) compared for different PEs (data were retrieved from the references (31, 63, 156) are compared to this studies POPE/DPPE mixtures).

The alleviation of packing frustration is achievable with the addition of host molecules. Here, alkanes such as tetradecane are well-studied, aggregating within the hydrophobic region and essentially filling the interstitial void spaces (186). Reducing the packing stress in this way has been shown to lower the transition temperature at which the H_{II} phase occurs. This additional 'padding' along the methyl trough region allows the packing stress to relax and the water core interface to become more circular. Dodecane has also been studied, similarly demonstrated to

aggregate within the hydrophobic regions, i.e., mainly in the corners of the Wigner-Seitz cell (187), reducing the need for lipid-chain compression towards short length (flat side) and increasing the effective maximum lipid length, l_{max}. Overall, alkanes not only relieve the extension stress but concomitantly relax the compression stress at the flat sides of the hexagon. Conversely, alpha-tocopherol (vitamin E) aggregates within the short lipid-length regions, allowing the lipids to stretch to their natural length in the corner regions (188), leading to a reduction in l_{max}. Any stress reducing additives serve to lower the free energy of the H_{II} phase, as much of the energetic cost arises from the distortion of the cylindrical water core into a quasi-cylindrical shape. This energy cost is intrinsically linked to the stretching and compression of the lipid chains.

In this study, we scrutinised the shape of the water core by how closely it resembles a perfect circle after adding a host lipid akin to the main building block. That is, SAXD measurements were performed on 1-palmitoyl-2-oleoyl-*sn*-phosphatidylethanolamine (POPE) with increasing molar concentrations of 1,2-palmitoyl-*sn*-phosphatidylethanolamine (DPPE). DPPE is a phospholipid with two fully saturated C16 hydrocarbon tails, whereas POPE has one monounsaturated C18 hydrocarbon tail. Due to its effective longer chain length (note, at 75 °C the steric membrane thickness of DPPE is 4.6 nm compared to 4.3 nm of POPE (40)), DPPE is thought to aggregate orientated towards the vertices of the Wigner-Seitz cell, while POPE will aggregate mainly in the flat side regions. In this way, packing stress is released as each lipid will tend to locate where it can assume its natural length. Therefore, the energy loss associated with the interstitial void regions is accounted for by the longer-chained DPPE lipids. Our aim of this study was to find the critical DPPE concentration at which the packing stress is minimised and the water core will adapt a nearly perfect circle in order to understand the interplay of packing and curvature frustration within the inverse hexagonal unit cell. Furthermore, we are presenting the local membrane hydration differences in the flat and corner zones of the hexagonal unit cell and demonstrated how the lipid compression and decompression alter the hydration properties locally.

4.2 Materials and Methods

4.2.1 Materials and Sample Preparation

1-Palmitoyl-2-oleoyl-sn-phosphatidylethanolamine (POPE) and 1,2-palmitoyl-*sn*-phosphatidylethanolamine (DPPE) were used as supplied from Avanti Polar Lipids, Alabaster, AL (purity >99%). Lipid stock solutions were prepared by dissolving weighted amounts of dry POPE or DPPE powder in chloroform. DPPE concentrations of 3, 6, 9, 12 and 15 mol % within the lipid bilayer were obtained by mixing appropriate amounts of the stock-solutions. The organic POPE/DPPE mixture was vortexed for 2 min and the solvent was evaporated in a vacuum oven for 24 h at 30 °C at $2 \cdot 10^{-3}$ mbar to secure that all traces of chloroform were removed. The thin lipid films on the bottom of the glass vials were subsequently suspended in 18 MΩ cm water (MilliQ). To ensure complete hydration, the lipid dispersions were shock-frozen in liquid nitrogen, thereafter thawed for 15 min, reaching a final temperature of 75 °C (about 15 °C above the main transition of DPPE), and finally vigorously vortexed for 2 min. For further annealing of the multilamellar vesicles, the above procedure was repeated six times. For the X-ray scattering experiments a final lipid concentration of 20 wt% was used.

4.2.2 X-ray scattering Measurements and Analysis

Diffraction patterns of multilamellar vesicles were recorded on the Austrian SAXS beamline at the Synchrotron of Trieste(189, 190), using a one-dimensional Gabriel detector(191) covering the corresponding q-range ($q = 4\pi \sin(\theta)/\lambda$) of interest from about 2π/450 Å to 2π/12Å. The angular calibration of the detector was performed with silver-behenate (192). The lipid dispersions were measured in a thin-walled, 1-mm diameter quartz capillary in a steel cuvette (Anton Paar, Graz, Austria), which was inserted into a brass block, being in thermal contact with a water bath circuit (Unistat CC, Huber, Offenburg, Germany). The entrance and exit windows of the sample cell have been covered with a thin polymer film in order to avoid air convection at the capillary. The temperature was measured in the vicinity of the capillary in the sample holder block with a Pt-element (100 Ω). Before exposure, the

sample was equilibrated for a period of 10 min for a given temperature. Exposure times was set to 30 s.

The electron density maps of the H_{II} phase were derived from the small-angle X-ray diffraction pattern by standard procedures (31, 156). Briefly, after the raw data had been corrected for detector efficiency and the background scattering arising from the water and the capillary had been subtracted, all Bragg peaks were fitted by Lorentzian distributions (see fitting examples in Figure B1 in the Appendix B). The fittings were carried out with the software package Origin Pro 9.0 (OriginLab Corporation, Northampton, MA). Second, the intensities were normalised for their multiplicity. Thereafter, a Lorentz correction was applied by multiplying each peak intensity (peak area) by its corresponding squared wave vector modulus, q^2. Finally, the square root of the corrected peak intensity was used to determine the form factor *F* of each respective reflection (for details see ref. (59)). The electron density contrast relative to water was calculated by the Fourier analysis:

$$\Delta\rho(x,y) = \sum_{h,k\neq 0,0}^{h,k\ max} \alpha_{h,k} \cdot F_{h,k} \cdot \cos(q_x(h,k)\,x) \cdot \cos(q_y(h,k)\,y), \qquad (4.1)$$

where $F_{h,k}$ is the amplitude of the peak at the position *q(h,k)* and *h,k* are the Miller indices of each reflection. Note, for centrosymmetric electron density maps the phase information for each amplitude is either positive or negative, i.e., $\alpha_{h,k}$ takes the value of +1 or -1. The best phase choice combination (+1 -1 -1 +1 +1 +1 +1) for the recorded (1,0), (1,1), (2,0), (2,1), (3,0), (2,2) and (3,1) reflections were taken from literature(31, 39). Due to experimentally reported zero-crossing of the form factor near the (21) reflection(63), its best phase choice has been checked for all electron density map calculations. Additionally, the two weakest reflections (22) and (31) reflections were checked for their best phase choices as well (for further details see Figure B2 in the Appendix B).

After Fourier analysis, the real space electron density map can be plotted for each molar fraction of DPPE defined as f = DPPE/(POPE+DPPE). Using a MatLab programme, 2D images of the electron density map were plotted (*x, y*), where the height in the z-axis represents the electron density contrast, $\Delta\rho$. The centre of the nanotube, which resides in the water core, rests on the origin (see Figure 4.1 and

Figure 4A). Thus, the nanotube long-axis is parallel to the z-axis. The lattice parameter, *a*, is the distance from the centre of one nanotube to the centre of an adjacent nanotube.

The y-axis passes through the origin and intersects with the centre of the flat side of the Wigner-Seitz cell, which is referred to as the zero position, denoted by an orientation angle γ = 0°. An electron density profile (EDP) along *y(0°)* (the short length) was determined. Using the MatLab programme, the line *y(0°)* is rotated by γ =30° to create an EDP, which intersects with the corner of the Wigner-Seitz cell, the longest distance that the lipids need to fill (Figure 4.1 and Figure 4.4A). Further, EDPs along two interfacial lines were calculated, i.e., concerning the maximum density at the position of the phosphate group and the minimum density in the methyl-trough region as a function of the rotation angle γ (Figure 4.4A). Finally, using these two orientation angles, the radial position, R_P, of the phosphate group can be determined as a function of γ using the electron density profiles along the two interfacial lines. However, in this study, we solely report on R_{max} and R_{min}.

To calculate the circularity of the water core, it is necessary to first calculate its circumference and area. Starting from the zero position, R_p as a function of γ was calculated. The angle, *y*, was varied in steps of 1°, leading to two subsequent radii, which we shall refer to as R_n and R_{n+1}. The corresponding points of the phosphate group positions are defined as $H_n(x, y)$ and $H_{n+1}(x, y)$, respectively. These two positions are observable from the maximum in electron density. The distance, $\overline{H_n H_{n+1}}$, between these two consecutive points, was then calculated using Pythagoras' theorem. By rotating *y* in 1° steps within a 30 ° segment, the arc length around the water core was then calculated from the summation of 30 segments: $\sum_{n=0}^{n=30} \overline{H_n H_{n+1}}$. The arc length of one 30° segment multiplied by 12 results in the water core circumference (Figure B3 in the Appendix B). The area of the water core was calculated from the summation of each of the small triangles enclosed by the lengths of R_n, R_{n+1} and the distance $\overline{H_n H_{n+1}}$. The lengths of R_n and R_{n+1} were calculated from the distance of their respective phosphate group positions from the origin. The area of a single triangle was given by the formula:

$$A_{Triangle} = \frac{1}{2} R_n R_{n+1} \, sin(\Delta\gamma) \tag{4.2}$$

where Δγ was set 1°, the angle between the two subsequent radii. A 30° segment will include 30 individual areas, which were summed together and multiplied by 12 to approximate the area of the water core. Once circumference and area are known, the circularity can be calculated using the equation:

$$C = \frac{4\pi A}{P^2} \tag{4.3}$$

where *A* and *P* are the approximate water core area and circumference, respectively. We note that a perfect circle will have a circularity value of 1.

Calculation of the maximum and minimum lipid length requires the average water core radius $R_{ave.}$ For this study we have averaged the radius from each measurement within the 30° segment. The minimum, maximum and average lipid length can then be calculated from:

$$l_{min} = \frac{a}{2} - R_{ave} \tag{4.4}$$

$$l_{max} = \frac{a/2}{\cos(\pi/6)} - R_{ave} \tag{4.5}$$

$$l_{ave} = \left(\frac{a}{2} - R_{ave}\right) \cdot \left(1.1084 + 0.0572 \left(\frac{R_{ave}}{\frac{a}{2} - R_{ave}} - 1\right)\right) \tag{4.6}$$

where *a* is the lattice parameter. Note, the Equation (6) was derived in reference (39), while Equation (4.4), (4.5) and (4.7) follow from simple geometrical relationships, where the latter was used to calculate the apparent area per lipid, A_P, at the phosphate position (see Figure 4.1):

$$A_P = V_{ave} \left(\frac{2\pi R_{ave}}{\frac{\sqrt{3}a^2}{2} - \pi R_{ave}^2}\right) \tag{4.7}$$

V_{ave} is the averaged lipid volume, which was calculated from:

$$V_{ave} = (1 - f) \cdot V_{POPE} + f \cdot V_{DPPE} \tag{4.8}$$

where *f* is the molar fraction of DPPE and the temperature dependent volumes of POPE and DPPE were taken from references.(156, 193) From the linear behaviour of

the molecular volumes as a function of temperature, we found by linear regression: V_{POPE} (nm^3) = 0.0008016 · T + 1.152 (R^2 = 0.9867) and V_{DPPE} (nm^3) = 0.0014692 · T + 1.058 (R^2 = 0.9968).

Further, the number per lipids along the circumference, n_L, the area per lipid at the steric lipid/water interface, A_W (see Figure 4.1), and the molecular wedge angle, θ (see Figure 4.3) were determined according to reference.(31)

$$n_L = 2\pi \cdot R_{p\,ave} / \sqrt{A_p} \tag{4.9}$$

$$A_W = A_P \frac{R_W}{R_P}, \text{ with } R_W = R_P - 0.55 \text{ nm} \tag{4.10}$$

$$\theta = 2 \cdot \arctan\left(\frac{\sqrt{A_P}}{2\,R_P}\right) \tag{4.11}$$

To examine the influence of DPPE on membrane stability, we have investigated the type of disorder in two directions, i.e., oriented to the vertex and flat side of the Wigner-Seitz cell as a function of DPPE concentration. For this, the two corresponding sets of diffraction peaks with the Miller indices (1 0), (2 0), (3 0) and (1 1), (2 2), respectively, have been analysed. These two families refer to the <1 0> and <1 1> directions, respectively (Figure 4.1A). Since the peak width progression of the (1 0), (2 0) and (3 0) clearly displays disorder of 2nd kind (Figure B4 in the Appendix B), we applied, in a zero order approach, the Modified Caillé Theory (MCT) (194) to this set of planes. Note, while this set of planes is strictly not resembling a planar smectic phase, still the water channels are aligned coplanar and are stacking in an alternating fashion with lipid-bilayer regions. After background subtraction this set of diffraction peaks were analysed with MCT in order to retrieve the fluctuation parameter, η, which then can be related to a mean square fluctuations between layers through the equation (69):

$$\sigma = \sqrt{\eta}\,\frac{d}{\pi} \tag{4.12}$$

where σ is the fluctuation distance and d is the d-spacing. Note, each diffraction peak was fitted individually and the resulting η values were averaged to retrieve one σ value referring to the <1 0> direction.

Following the recently published three-water layer model (195), and having estimated the membrane-fluctuation distance, σ, allows us to divide the water core into three distinct regions: (i) the “headgroup region” associated with the water volume around the headgroup, (ii) the “perturbed region” defined by the fluctuation distance σ, and (iii), the “free water region”, which is unperturbed by the fluctuating lipid monolayer. For the calculation of the total water volume, we used the approximation (31):

$$V_w = \frac{A_p \cdot R_p}{2} \qquad (4.13)$$

Note, this estimation sets the net water-lipid interface at the height of the phosphate group. This artificial net interface is also known as Gibbs dividing surface (58). Also the perturbed and free water volumes are based on the geometry of the molecular wedge-shape model depicted in Figure 4.1B (cp. Equation 13). In this model, the radii and their corresponding areas are proportional since the wedge depth is constant. For instance, we deduced the area A_{wf} from the relationship: $R_{wf}/R_p = A_{wf}/A_p$. Specific number of waters per water region were calculated, dividing the partial water volumes by the volume of a single water molecule (V_{H20} = 0.03 nm^3 (115)). The headgroup extension, D_H, in radial direction was taken from literature to be 1.1 nm;(63) accordingly $R_p = R_{wf} + \sigma + 0.55$ nm.

All errors given in the Results and discussion section are referring to standard deviation for directly-retrieved parameters, e.g., *d*-spacings that were determined by fitting their corresponding diffraction peak positions. All other derived parameters errors were determined by standard error propagation.

4.3 Results and Discussion

4.3.1 Fluid lamellar to Inverse Hexagonal Phase Transition

Transition temperatures were obtained from the fractional formation plots of the H_{II} phase, $f(H_{II})$, which were derived from the fitted total intensities of the first order diffraction peaks of the L_α and H_{II} phase with $f(H_{II}) = I(H_{II})/[I(H_{II}) + I(L_\alpha)]$ (Figure 4.2B-D; see Figure B5 in the Appendix B for an overview of all transition plots). The inflection point determines the transition temperature, T_H (Figure 4.2A). The data were fitted with a logistic function, setting $f(H_{II})$ at the beginning and the end of the transition to 0 and 1, respectively. For the best comparison, all inverse hexagonal phases were analysed in this study 5 °C above T_H, ensuring the systems had developed a fully stable H_{II} phase. We note that this choice meant that traces of the L_α phase are coexisting with H_{II} phase, but even so, avoiding the onset of dispersion instabilities that we observed closer to the boiling point of water.

The observed increase in T_H (Figure 4.2A) is in agreement with the linear relationship of the critical packing parameter (the CPP) with T_H (Figure 4.1C). The addition of DPPE causes the overall degree of chain splay to decrease which leads to an increase of T_H of about 11 °C. Interestingly, we observe a local minimum in the transition width at 9 mol% DPPE, which means that this particular sample displays the highest transition cooperativity. Generally, the cooperativity in a given transition increases with its crystallinity, or in other words, with the degree of structural order. The following section on the fine structural analysis of the different POPE/DPPE mixtures will explain the exceptional good degree of order for the 9 mol% DPPE sample in more detail.

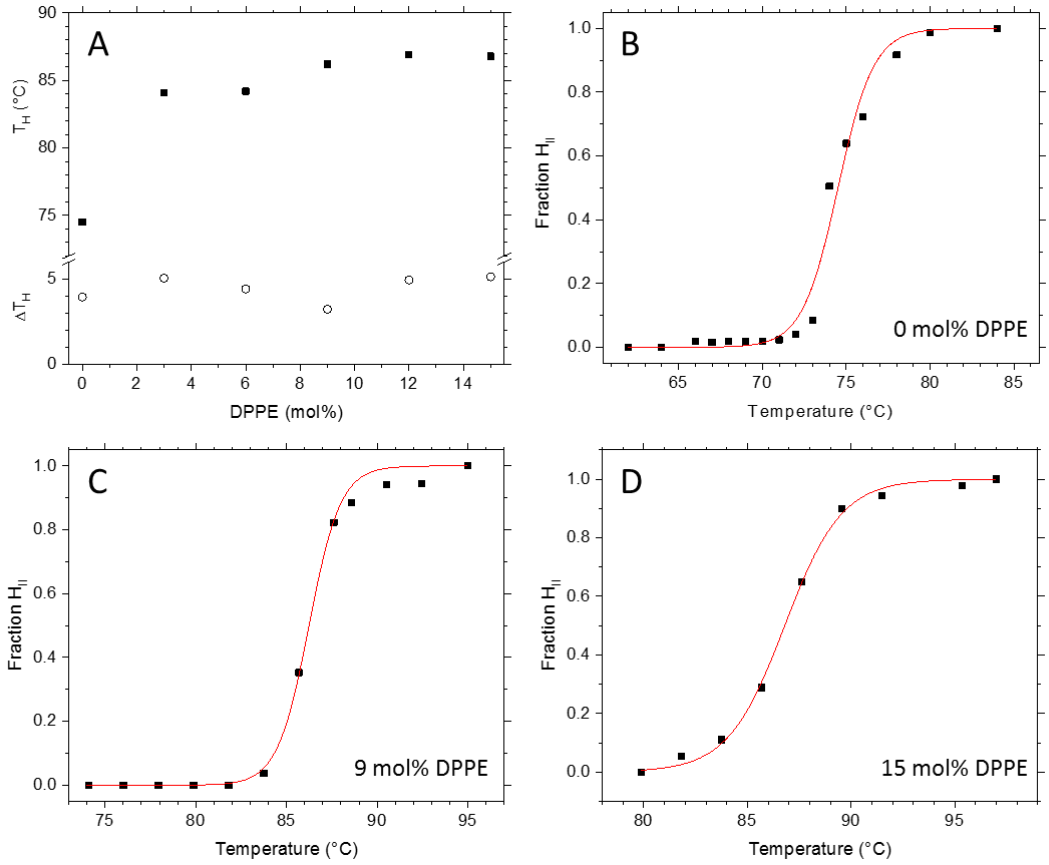

Figure 4.2 Formation of the inverse hexagonal of POPE/DPPE mixtures. (A) The transition temperature from the L_α to H_{II} phase, T_H (squares) and the *FWHM* of the transitions (circles) are plotted as a function of the molar DPPE content. (B-D) Turnover curves as a function of temperature are plotted for 0, 9 and 15 mol% DPPE samples. Best logistic fits are given as red lines. Note, the inflection point of the logistic function defines T_H, while the *FWHM* of the corresponding logistic distribution defines the transition widths, ΔT_H.

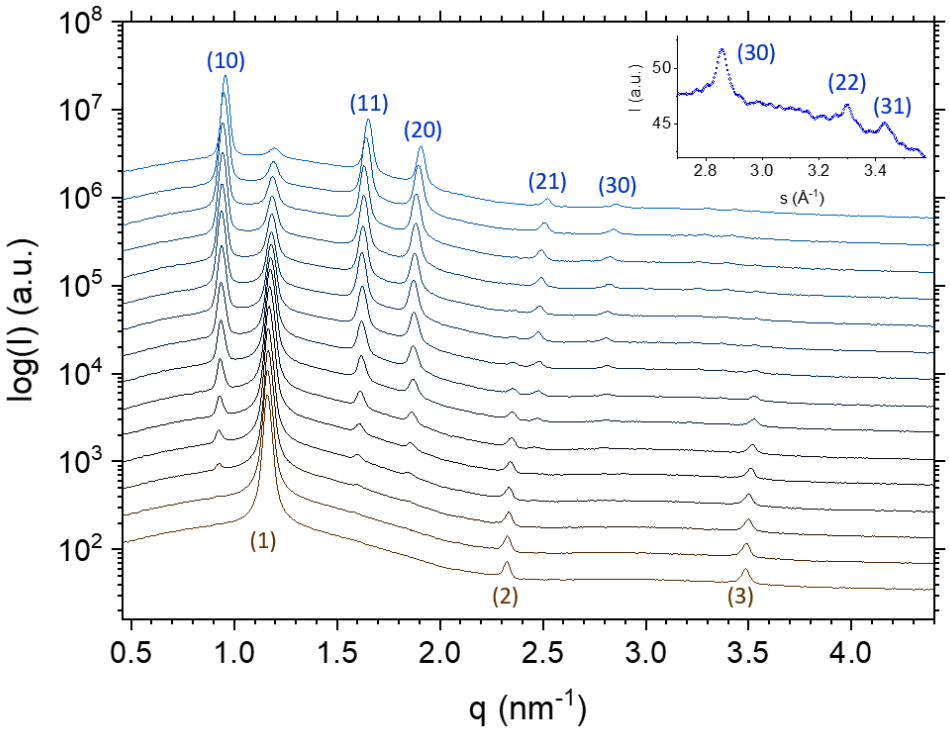

Figure 4.3 Stack plot of the SAXD pattern of the POPE/DPPE mixture with 3 mol% DPPE. The temperature was increased in constant steps from 78 to 95 °C. The midpoint of the transition from the L_α to H_{II} phase is at 84 °C.

The stack plot of the small angle X-ray diffraction patterns (SAXD) displays L_α to H_{II} phase transition of the POPE/DPPE mixture with 3 mol% DPPE (Figure 4.3). The temperature-range spans from 78 to 95 °C with T_H = 84 °C. From the L_α phase, the first three diffraction orders were recorded, while the (31)-reflection was the highest recorded diffraction peak for the H_{II} phase. In order to analyse the effect of the host molecule concentration of DPPE on the packing frustration within the H_{II} phase, electron density maps of all mixtures with DPPE concentrations of 0, 3, 6, 9, 12 and 15 mol% were determined at $T = T_H + 5$ °C. This included all recorded reflections from (10) to (31). For an overview on the experimental conditions and the determined intensities $I_{h,k}$ and amplitudes $F_{h,k}$ of all experiments refer to Table S1 in the ESI. Further note, given the similar molecular volumes of POPE and DPPE, the corresponding vol% values at $T_H + 5$ °C are close to the mol% values, i.e., 2.9, 5.8, 8.8, 11.7 and 14.6 vol%.

4.3.2 Fine-structural analysis of the inverse hexagonal phases

Nanostructural analysis conducted on the electron density maps is shown in Figure 4.4 (see also the overview graph Figure B6 in the Appendix B). In panel A, two key orientations within the Wigner-Seitz unit cell (red dotted line) are shown, concerning γ = 0° being congruent with the *y*-axis (red dashed line), as well as the orientation for γ = 30° (blue dashed line). The first orientation shows the shortest radial distance in the Wigner-Seitz cell, whilst the second orientation shows the longest radial distance. Thus, these are the two orientations of the maximum hydrocarbon chain compression (γ = 0°) and decompression (γ = 30°), respectively (see also Figure 4.1A). The H_{II} phase structure has a 6-fold symmetry, therefore the lipid compression and decompression is the same in the orientation of any corner or flat side, meaning that it is sufficient to analyse all structural details over a 30° segment as pictured in Figure 4.4A. Maximum electron density is colour-coded with dark-red and minimum electron density with dark blue; correspondingly, the red-dotted line indicates the methyl trough region of the lipid matrix, and the blue-dotted line indicates the apparent position of the phosphate groups. The radial position of the phosphate group, R_P, as a function of γ was calculated as the distance from the origin to the maximum density. Whilst some structural differences are already seen by the naked eye in the electron density maps (Figure 4.4 and Figure B6 in the Appendix B), finer details are revealed through investigation of the different structural parameters as a function of the rotational angle, γ. A first overview of the structural results is given in Table 4.1.

From Table 4.1 it can be seen that the averaged radius, $R_{P\,ave}$, increases after the addition of DPPE, gradually at first, but it appears to plateau after 6 mol%. This is to be expected since the addition of fully saturated DPPE lipids reduces the effective chain splay. This is best observed in the averaged molecular shape: the molecular wedge-angle (see Figure 4.1B) drops from initially 19.9° to 17.8° (Table 1; Equation 4.11). As this occurs, the added DPPE reduces the need for stretching and compression of lipids around the water core, since both POPE and DPPE are allowed to reside in regions where they can best adopt their natural length. This is confirmed by the local minima of the lattice spacing, *a*, at 9 mol% DPPE, which is dominated by

the phosphate position radius $R_{P\,ave}$. We also observe for 9 mol% the smallest water core area (πR_p^2) and lowest number of lipids around its circumference with respect to its neighbouring DPPE concentrations. Note, the average lipid length, the headgroup area and the chain splay change significantly only once DPPE is added, but these parameters remain within errors constant from 3 to 15 mol% DPPE (Table 4.1). Since the interstitial regions in the inverse hexagonal phase account for about 9 vol% (180), it is plausible that 3 mol% DPPE (equal to 2.9 vol% DPPE) is not sufficient to fill out the corners of the unit cell. Beyond the ideal concentration of 9 vol%, it is plausible that DPPE again starts to inhibit the ideal packing of POPE, causing the lipid chains to stretch/compress beyond their natural state. Interestingly, for 9 mol% DPPE the water core area is the smallest compared to adjacent concentrations; although the headgroup area per lipid remains, within errors, the same. Indeed, the number of lipids per water core circumference, n_L, also displays accordingly, a local minimum. This means, adding too little DPPE most probably leads to an accumulation of relatively more POPE in the vertices (decompression zones) to overcome the packing frustration, whereas adding too much DPPE leads to packing stress in the compression zones of the hexagon. This is then compensated by accumulating relatively more POPE in the compression zones. Last, we note that average chain splay – which is directly observed in the wedge angle – increases linearly with temperature for pure lipid/water systems (31). However, the wedge angle in our study does actually decrease when DPPE is added, although the mixtures are analysed at slightly increasing temperatures. This is understandable, due to the lower chain splay caused by the added DPPE lipids. Concluding, the lowest water core area and smallest number of lipids per circumference imply that the packing stress is the lowest at 9 mol% DPPE; further to this, the 9 mol% mixture displays the best circularity of the water/lipid interface (Table 4.2), which is discussed in more details in the next paragraphs.

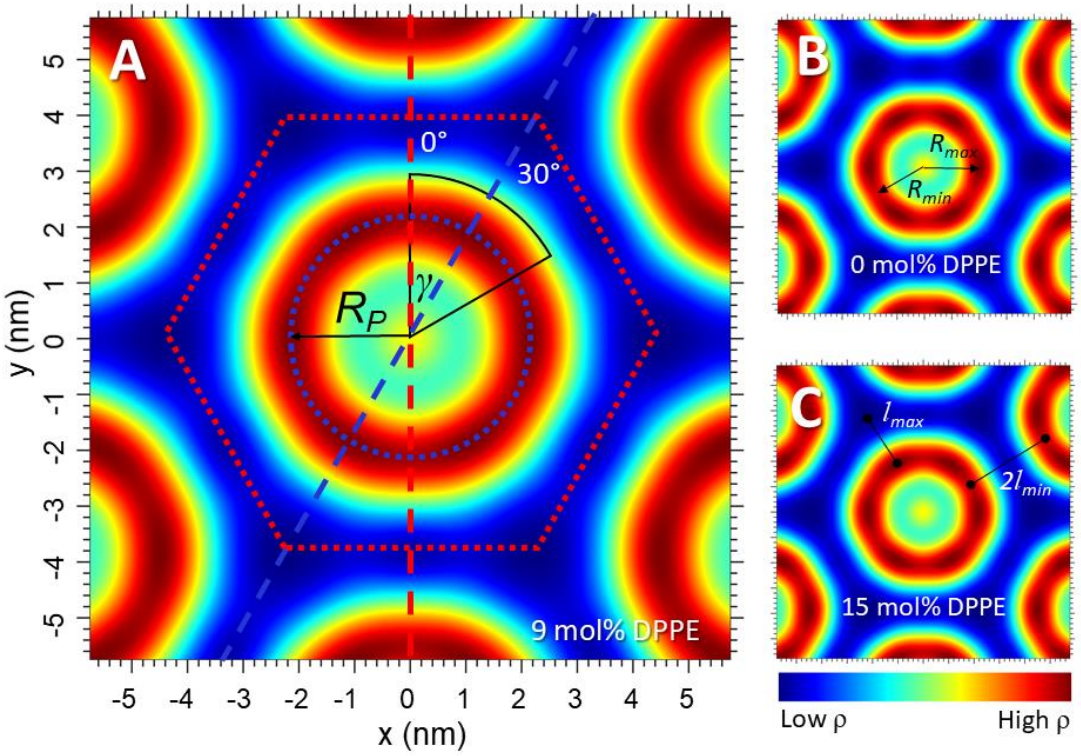

Figure 4.4 Electron density maps of POPE/DPPE for 0, 9 and 15 mol% DPPE. (A) The head-group interface (blue dotted line), the methyl trough region (red dotted line; note this defines also the Wigner-Seitz cell of the H_{II} phase), the radius R_P, the orientational angle γ and with it two pathways for calculating the electron density profiles are defined. R_{min} and R_{max} as well as l_{min} and l_{max} are illustrated in (B) and (C).

Table 4.1 Structural parameters of the H_{II} phase as a function DPPE concentration.

DPPE (mol%) @ T (°C)	a (nm)	$R_{P\,ave}$ (nm)	Water core area (nm²)	l_{ave} (nm)	V_{ave} (10^{-3} nm³)	A_P (nm²)	n_L	Wedge angle (°)
0 @ 80.0	7.12±0.007	1.98±0.01	12.4±0.02	1.77±0.01	1215±5	0.48±0.1	18.0±0.2	19.9±0.2
3 @ 89.5	7.66±0.008	2.13±0.01	14.2±0.02	1.91±0.01	1222±5	0.45±0.1	20.0±0.2	17.8±0.2
6 @ 89.5	7.73±0.008	2.17±0.01	14.8±0.02	1.90±0.01	1221±5	0.45±0.1	20.3±0.2	17.6±0.2
9 @ 90.5	**7.66**±0.008	**2.14**±0.01	**14.4**±0.02	1.90±0.01	1221±5	0.45±0.1	**20.0**±0.2	17.8±0.2
12 @91.5	7.72±0.008	2.16±0.01	14.7±0.02	1.91±0.01	1221±5	0.45±0.1	20.2±0.2	17.7±0.2
15@ 91.5	7.70±0.008	2.15±0.01	14.6±0.02	1.91±0.01	1220±5	0.45±0.1	20.2±0.2	17.7±0.2

As seen in Figure 4.5A, the EDP curves as a function of γ smoothen out at 9 mol% DPPE in the head group region. In the methyl trough region (Figure 4.5B), it is the 15mol% DPPE sample instead, which shows the least disparity between its minimum and maximum electron density values. Nonetheless, 9 mol% DPPE promotes the greatest homogeneity of the lipid packing around the water core itself. From Figure 4.5C, 4.5D, 4.5E comparing the EDPs along R_{min} and R_{max}, it is shown that the electron density is closest to uniformity at 9 mol% DPPE, as opposed to the two extremes of 0 and 15 mol% DPPE. Similarly low are the electron density fluctuations for the 6 mol% (see Figure B8 in the Appendix B). This interpretation is further illustrated in Figure 4.6C, where the ratio of the phosphate electron density values given for the <10> and <11> direction, is close to unity at 9 mol% due to a more even distribution of the lipid headgroups around at the water/lipid interface. Conversely for the 0 and 15 mol%, which display about 8% lower ρ_{min}/ρ_{max} values (Figure 4.6C), where the phosphate electron density ratio is much lower, it suggests lipid headgroups are not homogenously spread out at this interface compared to 9mol%.

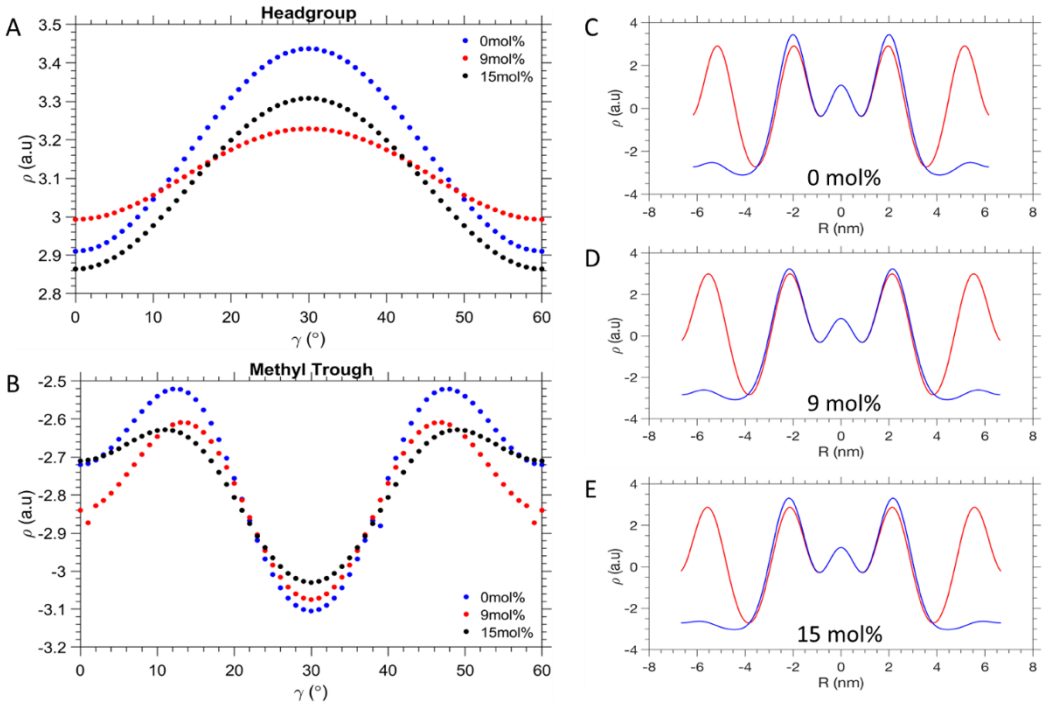

Figure 4.5 Electron density profiles. (A) Electron density fluctuation along in the head-group regions and (B) the methyl trough interfaces. (C-E) Radial electron density profiles with orientation of γ = 0° (red) and γ = 30° (blue). The interfaces and γ orientations are defined in Figure 4.4A. Comparisons of all concentration are shown in Figure B7 and B8 in the Appendix B.

Table 2 summarises the characteristics of the phosphate interface and its circularity. The data show that the system is at near equilibrium at 9 mol%, because the values for R_{max} and R_{min} are not only the lowest (Figure 4.6A), but display the smallest deviation from each other (Figure 4.6B). This is plausible from the alleviation of packing stress, meaning the lipids do not have to compress/decompress as much as compared to the neighbouring concentrations of DPPE. This is further supported by the value of the circularity being closest to 1 at this concentration. For pure POPE we observe the smallest l_{max} and l_{min} values due to the strongest chain splay given (Table 1). This is also reflected in the fact that POPE lipids in the fluid state are about 0.15 nm shorter than DPPE lipids(40) (see also l_{ave} in Table 1). Furthermore, for pure POPE the circularity is relatively low, clearly displaying non-ideal lipid packing. The same is true of 3 mol% DPPE, which in fact has the lowest circularity all around. It can be inferred that after the introduction of 3 mol% of DPPE, the packing efficiency may have worsened in this respect. The DPPE is therefore acting here essentially as an impurity, not yet at the threshold concentration to provide packing frustration relief. The 6 and 9 mol% DPPE mixtures appear to be the most homogenously packed aggregations, given their values for circularity. At the highest DPPE concentrations, a subsequent decrease of the circularity is observed. This is reflected in the increase of differing R_{min} and R_{max} values, mirroring the behaviour at 0 and 3 mol% of DPPE (Figure 4.6B). The notion that the 9 mol% DPPE sample is reducing packing frustration the best, is further illustrated in Figure 4.6C. The ratio of the phosphate electron densities given for γ = 0° and 30°comes close to unity. In contrast, the 0 and 15 mol% DPPE mixtures display a significantly lower the electron density ratio, which suggests that lipid headgroups are less homogeneously packed. However, the 6 and 9 mol% DPPE samples display a slightly bigger chain packing frustration as compared to 12 and 15 mol% DPPE, with their ρ_{max}/ρ_{min} values being about 2% smaller (Figure 4.6D). These subtle homogeneity improvements in the methyl trough region are most likely caused by a smoother and broader distribution of DPPE around the vertices as can be seen in the EDPs in Fig 4.5B. Summarising, while 3 mol% of DPPE does not induce any apparent chain packing frustration release (ρ_{max}/ρ_{min} = 0.81), a sudden improvement in the chain packing order is achieved for concentration for 6 mol% and greater (0.85-0.87).

Overall, the 9 mol% DPPE sample parameters confirm close to ideal lipid packing within the hexagon. From the geometric considerations of the Wigner-Seitz cell, the interstitial void regions constitute 9% of the overall area, so it is volumetrically plausible that 9 mol% DPPE (8.8 vol%) best accounts for this interstitial region to be occupied with the lowest packing frustration, and hence leading to a minimum in hydrocarbon chain compression/decompression within the vertex and flat areas. Predominant locations of DPPE in corner zones and POPE in the flat zones of the Wigner-Seitz cell, are therefore likely to be driven by releases in chain stretching energy (71, 179, 184). Indeed, free energy model calculations based on the theory of Iglič and colleagues (71), display a shallow local minimum in the free energy around 6-9 mol% DPPE with a value of about -0.06 kT per lipid, in which the bending energy accounts for -0.47 kT per lipid and the stretching energy with 0.41 kT per lipid (Figure B9 in the Appendix B).

Table 4.2 Structural parameters concerning the circularity of the phosphate position in the H_{II} phase.

DPPE (mol%)	l_{min} (nm)	l_{max} (nm)	R_{min} (nm)	R_{max} (nm)	Circularity
0	1.58±0.01	2.12±0.01	1.97±0.01	2.00±0.01	0.993±0.005
3	1.70±0.01	2.30±0.01	2.11±0.01	2.14±0.01	0.982±0.005
6	1.69±0.01	2.29±0.01	2.16±0.01	2.18±0.02	**0.997**±0.005
9	1.69±0.01	2.28±0.01	**2.13**±0.01	**2.15**±0.01	**0.997**±0.005
12	1.70±0.01	2.29±0.01	2.15±0.01	2.18±0.01	0.994±0.005
15	1.70±0.01	2.29±0.01	2.13±0.01	2.17±0.01	0.994±0.005

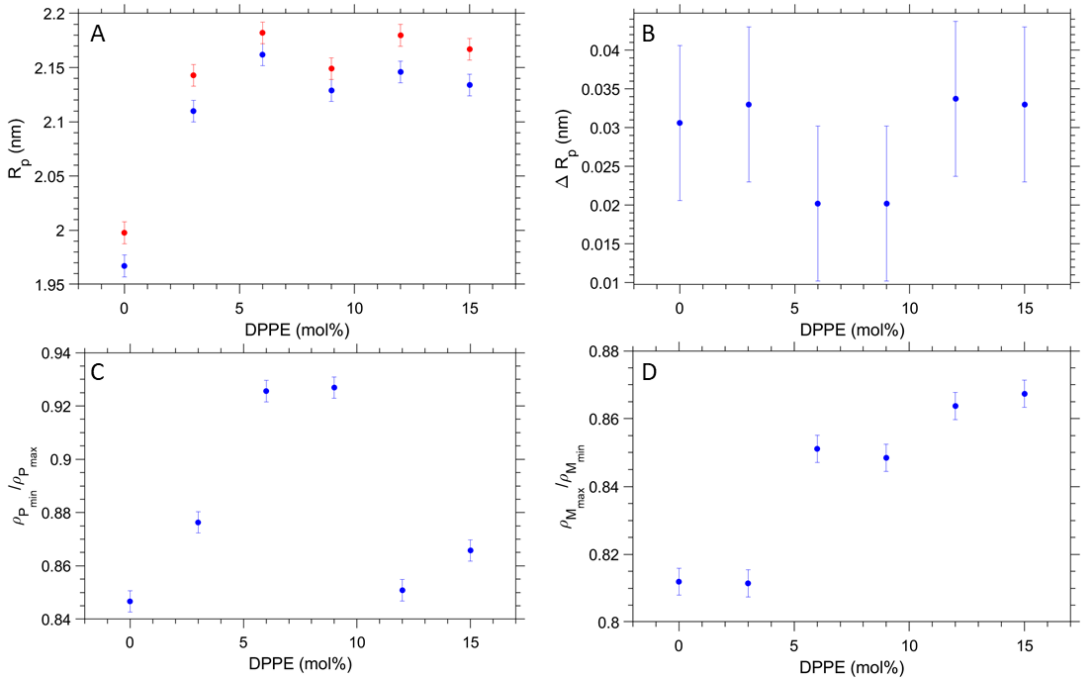

Figure 4.6 Probing the circularity the water core as a function of DPPE concentration. (A) R_P orientated towards the corner (red; R_{max}) and normal to the edge (blue; R_{min}), (B) ΔR_P equals R_{max} minus R_{min}, (C) electron density ratio $\rho(0°)/\rho(30°)$ determined at the phosphate position, and (D) electron density ratio $\rho(0°)/\rho(30°)$ determined at the methyl trough region.

Figure 4.7A and B display schematic models of the POPE-only and POPE/DPPE 9 mol% mixture. Note, the Wigner Seitz cells are drawn in scale, refering in their heights to the lattice parameters, a, equal to 7.12 and 7.66 nm, respectively. Further, the circles with the radius R_P plus l_{ave} of the POPE-only case are shown in both models with a dashed line, indicating that the average lipid length in the pure POPE sample comes closer to the minimum length, l_{min}, of the 9 mol% DPPE sample. These models confirm the notion that the POPE lipids are dominating the flat side locations, while the relatively longer DPPE lipids concentrate in the vertices of the hexagon.

4.3.3 Anisotropy of Disorder – Thermal *versus* Disorder of Second Kind

Finally, we have analysed the dynamic behaviour of the inverse hexagonal phase for 3, 9 and 15 mol% of DPPE samples. Of special interest is the local membrane fluctuation behaviour of the inverse hexagonal phases in the <10> and <11> directions (Figure 4.1 and Figure 4.7), which refer to the direction of R_{max} (towards the vertices) and R_{min} (towards the flat sides) within the hexagonal unit cell. As clearly

demonstrated in the Figure B4 (Appendix B), the peak shape progression in the <10> direction shows an increase in width as a function of the diffraction order, which reveals disorder of 2nd kind with strong undulations within this set of planes. In contrast, the peak shape progression in the <11> direction displays a constant width as function of the diffraction order, which demonstrates dominating thermal disorder instead. Thus, there is a clear anisotropy of disorder given in the inverse hexagonal phase. At this point, we have to stress once more that the MCT analysis that we applied to the (10), (20), (30) peaks (Figure B4 in the Appendix B) can strictly only be applied to smectic liquid crystals in the fluid phase (68) however, the purpose here is to gain an approximate value of the local layer fluctuations in this direction. The value of the fluctuation distance, σ, being in the order of 0.3 nm compares very well to the σ published for 1,2-dimyristoyl-sn-glycero-3-phospho-ethanolamine (DMPE) in the smectic phase at 80 °C (1, 40).

Table 4.3 Results concerning the fluctuation distance and number of water molecules per lipid in each water region.

DPPE (mol%)	σ (nm) <10>	Total Waters (averaged)	Headgroup waters	Core waters	Perturbed waters <10>	Free waters <10>
3	0.26±0.05	16.7±0.8	8.0±0.6	8.7±0.7	2.6±0.3	6.1±0.5
9	0.30±0.06	17.0±0.9	8.1±0.6	8.9±0.7	3.0±0.3	5.9±0.5
15	0.28±0.06	16.9±0.9	8.0±0.6	8.9±0.7	2.9±0.3	6.2±0.5

Given the fact that the disorder in the <11> direction is dominated by thermal disorder (Figure B4 B), we interpret the (10) planes to fluctuate more than the (11) planes at all concentrations of DPPE. Interestingly, this mechanical behaviour of the hexagonal aggregate being more compressible in the <10> directions, is also reflected in the electron density maps (Figure 4.4 and Figure 4.7C). The headgroup thickness apparently stretches over a wider region in the <10>, and subsequently the inner water core reduces in diameter in this direction. Thus, the water core can roughly be described as a rounded hexagon, but rotated by 30° relative to the hexagonal Wigner-Seitz unit cell (Figure 4.7C). While no clear DPPE concentration-dependent trend was

observed in the fluctuation parameter, we deduce the compressed lipid zones (flat sides) are mechanically more stable than the decompressed lipid zones around the vertices (see Figure B4).

4.3.4 Hydration properties of the inverse hexagonal phase

Concerning the number of water molecules in each defined water region, the headgroup waters are constant within errors for all mixtures (Table 4.3), which aligns with the small changes in the area per lipid, A_p. Indeed, A_p does not vary more than 1% from 3 to 15mol% DPPE (Table 4.1). For our DPPE/POPE mixtures, we find 8 water for the headgroup region, which compares to 7 waters per headgroup found in 1-stearoyl-2-oleoyl-*sn*-glycero-3-phosphoethanolamine (SOPE) (31). Also the total numbers of about 17 waters per lipid are within error margins constant and compare well to the 16 waters per lipids found in SOPE. Second, the number of perturbed waters per lipid is expected to be larger in the <10> direction as mediated by the larger fluctuation distance, σ. This consequently leads to a relatively smaller number of free waters per lipid in the vertices regions, when compared to the flat regions. In Figure 4.7D, we have graphically summarised our model for the extension of the headgroup water region, the perturbed water layer and the free water core.

Comparing the water distribution in the inverse hexagonal phase to the three-water layer model applied to the fluid lamellar phase of PEs (195), some remarkable differences become clear: First, the fluid lamellar phase of PEs has no free waters per lipid, while the inverse hexagonal phase displays 6.5 free waters per lipid in the <10> direction and most probably displaying an even greater number in the <11> direction (Table 4.3). Second, while the perturbed water layer thickness is constant along the lipid/water interface (σ = 0.3 nm for DMPE at 80 °C (1)), the membrane undulations in the inverse hexagonal phase differ in the vertices ($\sigma \approx 0.3$ nm) from those in the flat regions (disorder of 2nd kind *versus* thermal disorder). Third, the number of waters in the headgroup region are slightly smaller in the inverse hexagonal phase. Here 8 waters compare to 8.5 waters in the lamellar phase of DMPE at 80 °C (1). The same accounts for number of perturbed waters per lipid (about 3 waters compare to 6 waters in DMPE at 80 °C (195)). The latter differences are explained by the smaller

area per lipid in the inverse hexagonal phase (A_p = 0.45 nm^2 in the H_{II}-phase compares to A_p = 0.64 nm^2 in DMPE at 80 °C (195)) and its molecular wedge shape (Figure 4.1B).

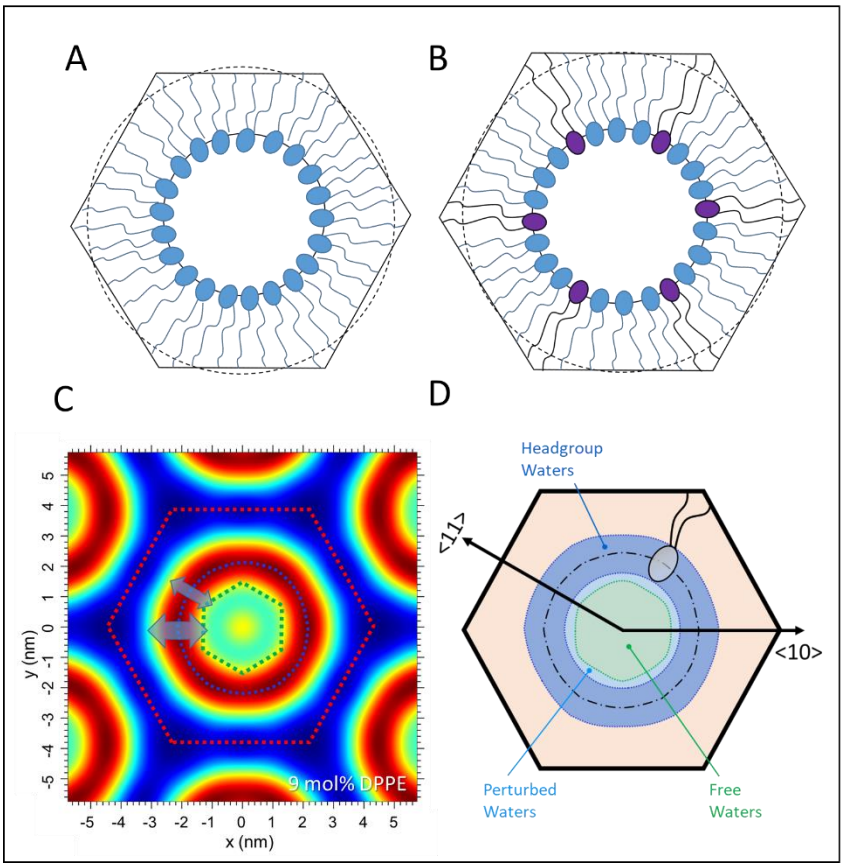

Figure 4.7 (A) Structural Model for POPE only and (B) the POPE/DPPE 9 mol% mixture. Note, for best comparison both models refer to the same scale. (C) Electron density map of the 9 mol% DPPE mixture, indicating stronger interfacial fluctuations in the <10> directions symbolically with a bigger double arrow (blue) and less dominant fluctuations in the <11> direction with a smaller double arrow (blue). Noteworthy, the resulting water/lipid interface resembles roughly a hexagon (green), being rotated by 30° with respect to the unit cell (red dotted lines). (D) Three different water regions are highlighted in blue ('headgroup' water), light blue ('perturbed' water) and light green ('free' water).

The observed anisotropy in the mechanical behaviour of the inverse hexagonal phase, and concomitantly, the change of local hydration properties has implications that go beyond this study. It can indeed be expected that any curved membrane contains a curvature-dependent mechanical stress distribution (23), which in turn will lead to local variations in hydration properties of lipid/water interface. Noteworthy, local variations in hydration properties go hand in hand with changes in repulsive

undulation and attractive Van der Waals forces (1) which might be decisive for a deeper understanding of biomembrane interactions with its extracellular world (73).

4.4 Conclusion

In this study, POPE was investigated in the H_{II} phase with increasing molar concentration of DPPE. The circularity as a function of DPPE concentration was determined to illustrate the alleviation of packing stress around the quasi-cylindrical outline of the phosphate positions. It was found that adding 6 and 9 mol% DPPE produced polar/apolar interfaces, which most closely resembled a perfect circle. Concerning the methyl trough regions, clearly the 9 mol% DPPE sample delivered the most homogeneous electron density distribution. Most likely, the longer hydrophobic chains of DPPE lead to its aggregation in the corner areas of the hexagonal Wigner-Seitz cell, and thereby reducing packing frustration in these interstitial regions. In particular, at 9 mol% of DPPE the smallest water core area and lowest number of lipids per circumference is given with respect to its neighbouring concentrations of 6 and 12 mol%, supporting the hypothesis that DPPE allows the lipids to aggregate more homogenously around the water core and ultimately reducing the energetic cost of chain stretching. Finally, we have shown that interfacial fluctuations are not significantly influenced by the addition of DPPE, but we have shown that the inverse hexagonal phase is mechanically most stable in the <11> direction (thermal disorder), and least stable in the <10> direction (disorder of 2^{nd} kind). The compression and decompression zones within the lipid monolayer also lead to a variation of hydration behaviour along the membrane/water interface.

Chapter 5. Membrane Dynamics and Confined Water Layer Classification in the Presence of Ion-Rich Solutions

Abstract

Ions intercalate in and around the plasma membrane of cells in order to facilitate cell function. The interaction of ions with the membrane interface influences inter-membrane forces, which determine membrane stability and dynamics. Understanding this interaction is beneficial for the improvement of models which utilise model membranes in order to replicate biological processes. In this study, multilamellar vesicles (MLVs) consisting of dipalmitoylphosphatidylcholine (DPPC) hydrated with ion solutions, at molar concentrations ranging from 0 to 1 M. The ions tested were monovalent sodium chloride (NaCl) and potassium chloride (KCl) (both monovalent), as well as magnesium chloride ($MgCl_2$) which is divalent. It was found that the monovalent salts continuously swell the inter-lamellar water spacing, with apparently little effect on the bilayer thickness. This is in contrast to the divalent $MgCl_2$, which at low salt concentrations displayed a degree of membrane unbinding. This behaviour eventually re-stabilises as the salt concentration increases and actually shrinks the inter-bilayer water spacing. This study also produced evidence to suggest that at high salt concentrations, the order of increasing membrane fluctuations does follow the cationic Hofmeister series. We have categorised out results according to a three-water-layer model, which accounts for water in the vicinity of the lipid headgroup, water perturbed by the membrane fluctuation, and a layer of free water which does not directly interact with the membrane. The influence of different ions at a range of concentrations is categorised according to this model, and the water molecules contained therein have also been calculated accordingly.

5.1 Introduction

Amphiphilic lipid molecules are present across many facets of nature making up the core matrix of cell membranes. Consisting of two hydrophobic chains and a hydrophilic headgroup, lipid molecules dispersed in water form a variety of liquid crystalline nanostructures with the lamellar phase most closely resembling the plasma biomembrane core (72, 73). An emerging field of research employing planar synthetic membranes relates to the design of artificial cells (82-84), which aims to mimic biological functions, using a minimalistic setup. The vast majority of model membrane systems are still used for studying biological interfaces under various environmental conditions (9, 37, 74, 134). In particular, phosphatidylcholine (PC) is a very well-studied phospholipid species, since it is frequently found in biomembranes (72).

When dispersed in water, phospholipids form bilayers where their hydrational state and nanostructure are closely related. Hydration is primarily dictated by the propensity of the headgroup to form hydrogen bonds (H-bonds) with interfacial water molecules (85). Here, the oxygen molecules of lipid headgroup function as H-bond acceptor, whilst the water molecule serves as the donor. For PCs, the focus of this study, the oxygen atoms at the phosphate group constitute the majority of hydrogen bonding, which occurs at the lipid/water interface. To a lesser extent, the oxygen atoms located at the ester linkages of the glycerol also contribute to hydrogen bond hydration (89, 92, 93). However, because of the ample hydrogen bonding at the phosphate, this region is commonly ascribed as the border between lipid and water, which to a very good approximation, coincides with 'Gibbs Dividing Surface' (96). PC lipids are zwitterionic, meaning they have a net neutral charge. Whilst the hydrocarbon core is apolar, the headgroup resembles a dipole along the phosphate (P) to nitrogen (N) vector. Here the oxygen atoms of the phosphate facilitate hydrogen bonding as acceptors due to their relative negative charge. The nitrogen atom of the choline group has a relative positive charge, thus cannot form hydrogen bonds with proximal waters. Water association at the choline moiety takes place via the hydrophobic effect, whereby waters from an ice-like clathrate shell around the choline group (89-91). This shell is loosely bound compared to the hydrogen-bonded

waters of the phosphate, but nonetheless, is linked to the choline and therefore the headgroup as a whole.

In our recently published study (1), the confined water layer in multi-lamellar vesicles (MLVs) was categorised into three distinctive sub-layers. Supported by small angle X-ray scattering (SAXS) results, a 'headgroup region', a 'perturbed water region' (directly adjacent to each headgroup region), and a single 'free water regions' have been proposed. A similar description of the confined water layer has been supported by quasi-elastic neutron scattering study (196), describing 'tightly bound' water (close to the glycerol and phosphate), 'loosely bound' water (close to the tip of the headgroup) and 'free water' (exclusive from the aforementioned classifications and yet different to the bulk water). Both studies emphasised the effect of water confinement on the behaviour of their respective sub-layer definitions. The behaviour of these sub-layers are intrinsically linked to the different hydration properties as well as to the inherent membrane mechanics given by the membrane bending and bulk compression moduli (134).

Contributing to our understanding of membrane hydration are the direct measurement of forces between adjacent bilayers and investigations on the adjacent membrane distances under applied osmotic stress (43, 94, 133, 197, 198), identifying vastly different hydration regimes between PCs and other lipid varieties (199, 200). Short-range forces concern the steric repulsion force at membrane distances below 0.4 nm and the repulsive hydration force from 0.4 to 1.0 nm (9). For membrane distances beyond 1.0 nm, long-range forces are facilitated by the attractive Van der Waals (VdW) and the repulsive Helfrich undulation force (201, 202). When the membrane surfaces hold a net charge, additionally electrostatic repulsion occurs (47, 203). The hydration properties of the different water regions becomes further complicated under the influence of added salts. Biological cells contain variety electrolytes, in the form of ions, with sodium (Na^+), potassium (K^+) and chloride (Cl^-) being the most commonly present. Ions within the intra and extra cellular medium play an important role in cell signalling (204), fusion (205), protein interactions (206, 207), and ion channel formation (20), which are essential to life across all organisms present on earth.

The intrinsic charge of an ion influences polar moieties like water. The effect of ions on water structure can be described as kosmotropic, hereby inducing water ordering and increasing the water-water hydrogen bond interaction. Ions of this nature are termed 'structure makers'. Conversely, ions can have 'structure breaking' characteristics that destabilise the water hydrogen bond network. Such ions are termed as chaotropic. Lipids themselves may also behave kosmotropically or chaotropically. For example, the relative positive charge of the choline group in PC membranes induces water ordering into an ice-like clathrate shell via the hydrophobic effect, which is chaotropic in nature. The extent to which a given salt ion has kosmotropic or chaotropic effects follows a frequently reoccurring trend across chemistry and biology known as the *Hofmeister series*.

The Hofmeister series is based on the ability of a salt to precipitate a protein in solution (208), originating from an anionic salt series, with chlorine (Cl^-) in a middle neutral position. Kosmotropic anions are protein stabilising (salting out), whilst chaotropic anions are protein destabilising (salting in) (207, 209, 210). Noteworthy, Cl^- hardly binds to the membrane, but is more likely to disperse in the water phase (211), where it is able to screen positive membrane surface charges (202). In fact, all ions, absorbed onto the membrane or dissolved in solution, will influence the charge density through the formation of an electric double layer.

Cations follow an inverse series with sodium Na^+ (roughly) at the central position, K^+ slightly chaotropic and Mg^{2+} being kosmotropic. That is, the ability to salt out proteins from solution is ranked $K^+ > Na^+ > Mg^{2+}$. Though Franz Hofmeister did observe this phenomena over a century ago (208), there is yet to be a conclusive explanation for its exact mechanism. Nonetheless, the Hofmeister series has been observed in a variety of biological processes, including lipid phase transition changes (210), vesicle swelling (212) and ion absorption (213).

Binding of an ion to the membrane interface occurs at the oxygen atoms, in this way dehydrating the membrane. Simulation and experimental studies on PC bilayers (214, 215) indicate that cations with an increasing ionic potential, as reflected in the increase of its radius with hydration (216), have a stronger binding affinity to the membrane. For instance, Na^+ and Mg^{2+} binds to the phosphate group. Whilst Ca^{2+},

with a lower ionic potential, binds at the glycerol group. Simulation studies of NaCl and KCl solution hydrated membranes revealed that Na^+ has a much higher binding affinity to the membrane compared to K^+ (214, 217). The effect of NaCl on water structure has also been linked to the swelling of dimyristoylphosphatidylcholine (DMPC) bilayers (218). Some evidence suggests this swelling effect in PC MLVs is slightly stronger for KCl (219). The cation Mg^{2+} is a kosmotrope with a strong affinity to the negatively charged phosphate group (215). $MgCl_2$ is expected to behave similarly to $CaCl_2$, leading to strong swelling of the MLVs at low salt concentrations due to unscreened electrostatic repulsion forces, whereas it will stabilise the bilayers at high salt concentration (203), leading to closer equilibrium distance of adjacent bilayers.

In this study, the lipid dipalmitoylphosphatidylcholine (DPPC) has been hydrated with solutions containing NaCl, KCl and $MgCl_2$ at molar concentrations ranging from 0 to 1 molar (M). Using SAXS, we have investigated MLVs in the liquid crystalline state in order to categorise membrane swelling under the influence of different ions, as well as trying to understand the effect ions have on membrane fluctuation and dynamics. Using these observations, we have also delineated the confined water layer into three distinct sub-regions defined by the three-water layer model (1) in order to shed further light on the complex salt ion, water and lipid interactions.

5.2 Materials and Methods

5.2.1 Materials and Sample Preparation

Dipalmitoylphosphatidylcholine (DPPC) was purchased from Avanti Polar lipids as a lipid powder dissolved in chloroform (25mg/ml). Sodium chloride (NaCl), potassium chloride (KCl) and magnesium chloride ($MgCl_2$) were purchased from Merck as a powder and used without further purification. 1M stock solutions were prepared using MilliQ water and then diluted down to form individual solutions with concentrations: 0.05, 0.15, 0.3, 0.6 M. These concentration as well as a 0M and the 1M solution were used to hydrate the lipid powder, which had been dried by evaporating the chloroform under a N_2 stream and dried further under vacuum for

30 minutes. All dried lipid films were hydrated resulting in 5 wt% lipid dispersions. Multilamellar vesicles (MLVs) were formed by vigorous vortexing and intermittent heating to 60 °C (see further explanations below).

When hydrating dried lipid films under the influence of salt ions, the risk of osmotic stress caused by a salt gradient inside and outside of the vesicles is well-known (220, 221). This commonly leads to the coexistence of osmotically stressed and non-stressed vesicles. In order to negate the effects of osmotic stress, ensuring an even distribution of salt ions in the intra- and extra-vesicular medium, a phase transition cycling method was used. The hydrated vesicles are heated to 50 °C (the chosen measurement temperature) and vortexed vigorously, then allowed to cool back down to below the melting transition temperature, for DPPC this transition occurs at 41.5 °C (37). Once cooled to room temperature the sample was vortexed again. This procedure is similar to a freeze thaw cycle (203, 222, 223), where ion diffusion is improved through vesicles rupture. This cycle was repeated 10 times for each salt at each concentration. The heat cycling method guarantees evenly distributed ion, because when approaching the main transition temperature, defects in the membrane start to form. This strong ion permeability of PC membranes around its melting point (224) allows the salt ions to penetrate through the membrane lamellae and distribute homogenously.

The dispersions were then transferred into 1.5 mm quartz capillaries and stored in a fridge (4 °C) for up to five days before X-ray measurements were performed. To avoid the anomalous swelling regime of DPPC near the main transition temperature (142, 225), all SAXS measurements were performed at 50 °C (this is roughly 7 °C above the anomalous swelling regime). Before the SAXS measurement was executed, each sample was equilibrated for 10 mins in 3-degree intervals from its transition temperature to the experimental temperature at 50 °C. At each interval a short X-ray exposure of 5 mins was performed and the resultant scattering curve was observed until it resembled a pure lamellar structure (meaning no peak splitting or diffraction peak shoulders apparent). This ensured that no osmotic stress effects were present. After the osmotic stress check, the final diffraction pattern was recorded.

5.2.2 Small Ange X-ray Scattering (SAXS) Experiments and Analysis

SAXS experiments were conducted at the Diamond Leeds SAXS Facility at the Diamond Light Source in Didcot using the Xeuss 3 instrument (Xenocs, Grenoble, France) equipped in with a molybdenum micro source with a wave length of 0.071 nm (Xenocs, Grenoble, France). The instrument is equipped with 2D Eiger R1M (Dectrix, Baden-Daettwil, Switzerland) and a sample to detector distance of 80 cm was used. The 1.5 mm wax-sealed capillaries were placed after leak tests under vacuum into the multiple capillary holder that controls the temperature with a Peltier element with a precision of ±0.1 °C (Xenocs, Grenoble, France). All measurement were performed under vacuum and the exposure was set to 1 hour.

The scattering intensity of multilamellar bilayers is expressed with the equation:

$$I(q) = \frac{S(q)|F(q)|^2}{q^2} \quad (5.1)$$

where *S(q)* and *F(q)* are the structure and form factor contributions, respectively, and *q* is the scattering wave vector modulus expressed as:

$$q = \frac{4\pi sin\theta}{\lambda} \quad (5.2)$$

where λ is the wavelength of incoming X-rays and 2θ is the scattering angle.

The data reduction steps were processed with the DAWN software (DAWN is funded primarily by the Diamond Light Source and works within the Eclipse Science Working Group). After the scattering data is imported into the programme, several important corrections must be performed before the data analysis. Here these steps will be briefly summarised, but a more detailed description can be found in reference (55). Firstly, a masking step is performed excluding invalid pixels, so they do not influence any further corrections. The next step concerns the determination of the counting uncertainty, which given by the square root of total counts in each detector pixel. Then the common incoming flux and transmission correction is performed by dividing the recorded intensity by the transmitted intensity (the transmitted intensity was determined in 25 x 25 pixel area around the direct beam position). Next is the angular efficiency correction, which accounts for the increase in photon detection probability at angles oblique to the detector. This previous correction marks the end of amendments arising from detector imperfections. A solid angle correction is performed to correct for the angle subtended by each pixel. An azimuthal correction

is done to reduce the 2D detector image into 1D-data. Finally, both the capillary and solution scattering is subtracted from the overall scattering signal of the dispersion (113), in which the excluded volume of the MLVs is considered when subtracting the solution scattering.

After the data reduction is completed, the resulting scattering curves were analysed using global fitting analysis (70). This method uses the structure factor according to the modified Callie' theory (68) and also is able to fit the form factor arising from membrane structure (here a simple 3 Gaussian model was applied (58)). Analysis of the data using this method yielded values for the lattice repeat distance, *d*, and bilayer head-to-head distance $d_{HH.}$ The latter of these two distances is calculated from the distance of the positive maxima of the electron density profile.

The fitting parameter, η, known as Caillé parameter or fluctuation parameter, defines the extent of membrane fluctuation. This parameter is directly related to the mean membrane fluctuation distance, σ, via the equation (69):

$$\sigma = \sqrt{\eta}\,\frac{d}{\pi} \tag{5.3}$$

where *d* is the lamellar repeat distance. In our discussion, σ is set equal to the thickness of the perturbed water region $d_W{}^{\sigma}$.

The Luzzati bilayer thickness (commonly defined by the 'Gibbs Dividing Surface' (56)) is reliant on the distance of the water/lipid interface from the lipid chain boundary. We define this distance as D_{H2}. The derivation of D_{H2} can be found in reference (1). Here, it is given by the equation:

$$D_{H2} = \frac{V_H \cdot (d_{HH} - 2D_{H1})}{2(V_L - V_H)} \tag{5.4}$$

where V_H and V_L are the headgroup and overall lipid volume respectively. D_{H1} is the partial head group thickness, or the distance from phosphate to chain boundary. In this study we use D_{H1} = 0.49 nm as an reliant estimate for PC bilayers (37, 43, 44). A constant volume of 1.232 nm^3 (37) was used for further calculations, as previous studies indicate that the volume per lipid does not change significantly within the salt concentration range used in this study (203, 223). A headgroup volume derived from the gel-phase was shown to be V_H = 0.319 nm^3 (37) and used in this study.

The Luzzati bilayer thickness, d_{LZ} is then calculated from the equation:

$$d_{LZ} = d_{HH} + 2(D_{H2} - D_{H1}) \quad (5.5).$$

Having all key parameters of the water layer defined (for graphical definition see Figure 5.2), we can then classify the overall water layer thickness d_W into its sub-layers via the equation:

$$d_W = d - d_{LZ} = 2d_w^{\sigma} + 2(D_H - D_{H2}) + d_w^{f} \quad (5.6)$$

where D_H is the headgroup thickness, shown to be 0.9 nm PCs (37) and d_W^f is the thickness of the free water layer (see Figure 5.2).

Finally, we are able to calculate the area per lipid A_L, which is required to calculate the number of water molecules in each water sub-layer. A_L is defined by the equation:

$$A_L = \frac{2V_L}{d_{LZ}} \quad (5.7)$$

which also defines the area of each water sublayer associated with a single lipid molecule. The number of water molecules in each layer was estimated by dividing the partial water volumes ($A_L \cdot d_w^{\sigma}$ and $A_L \cdot d_w^{f}/2$) by the volume of a single water molecule (V_{H20} = 0.03 nm^3 (115)). For the headgroup region, we define the excluded volume (D_H - D_{H2}) as the region containing water molecules. This region is defined by the water/lipid interface following the concept of the 'Gibbs Dividing Surface'.

5.3 Results and Discussion

Figure 5.1 displays the scattering curves for each sample and the best fit curves, using the global fitting method (56, 70). In general, we observed a slight increase of the diffraction peak tailing with increasing salt concentration, with the exception of $MgCl_2$, which actually exhibits peak sharpening, particularly at the higher salt concentrations. In this case, clearly three diffraction peaks are observed. Conversely at low salt concentrations, the influence of $MgCl_2$ demonstrates strong vesicle swelling, whereby the bilayers within the MLVs repel each other due to electrostatic repulsion. Overall, the increased peak tailing can be ascribed to an increase in membrane fluctuations due to an enhancement of the crystalline disorder of the 2nd kind (51). Disorder of 2nd kind also leads to a peak broadening as a function of

diffraction order, which can be seen in the dampening of the peak intensity of the 3rd diffraction order; observed by the diffraction peak being smoothened out into a broader distribution. We note, that any structure factor contribution beyond the 3rd order only displays as a diffuse scattering.

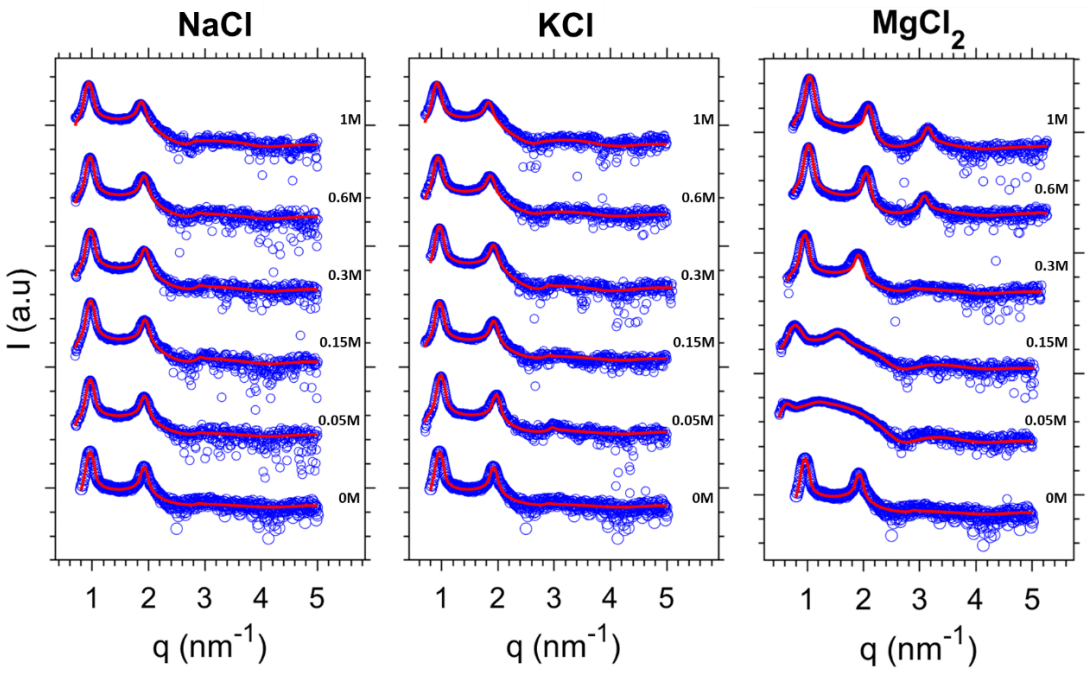

Figure 5.1 Diffraction pattern of DPPC MLVs under influence of salt ions. All diffraction pattern have been recorded at 50 °C and salt concentration have been varied from 0 to 1 M. From left to right, the influence of NaCl, KCl and $MgCl_2$ is illustrated. The experimental intensity data are depicted with blue circles, while best global fits are shown with red solid line.

Figure 5.2 summarises the overall findings on the behaviour of the confined water as a function of salt concentration. For NaCl and KCl, the water layer increases gradually with salt concentration, which is the main influence on the increasing *d*-spacing. At lower salt concentrations, the water layer thickness remains constant, but begins to increase approaching 1 M. The same is observed for the perturbed layer thickness in the presence of NaCl and KCl. Remarkably, the increase of the perturbed layer thickness as function of KCl concentration is more pronounced. For $MgCl_2$ an entirely different behaviour is eminent: At low salt concentrations a strong vesicle swelling is observed, due to a repulsion between bilayers by divalent cation adsorption to the bilayer surface (226, 227). At low salt concentrations, the shielding power of Cl^- ions

is too low to screen the electrostatic repulsion of the locally induced positive charge densities. With increasing Mg^{2+} concentrations, the charge density will approach its saturation in the membrane and concomitantly the charge density of Cl^- in the water phase increases linearly, at one point balancing the maximum charge density of Mg^{2+} in the membrane. This point is reached at about 0.5 M (Figure 5.2), therefore only at concentrations of 0.6 and 1.0 M the electrostatic repulsion is entirely screened, which is given at salt to lipid ratio of about 1 to 4 (Table 5.1).

Returning to the monovalent salt ions, simulation and experimental studies on K^+ and PC bilayers indicate that potassium ions do not penetrate and bind as closely to the membrane interface as Na^+ (201, 228). This reflects the slightly chaotrope character K^+. Pertaining to the swelling behaviour at 1 M, we observe a higher swelling in the presence of KCl when compared to NaCl (Figure 5.2, top row). Korreman and Posselt made the same observation in their study on the anomalous swelling in PC multilamellar vesicles in the presence of salts, which increases by 0.17 nm at 100 mM of NaCl and by 0.35 nm for 100 mM of KCl (219). The driving force for this lies in decrease of the Van der Waals (VdW) force in the presence of salt ions. For a better understanding, it is instructive to consider the Hamaker constant. The net strength of the Hamaker constant is proportional to the *dielectric contrast* between lipid headgroups and the aqueous solvent (8). Now, both NaCl and KCl do reduce the static dielectric constant from 80 (0 M) to about 65 at 1 M salt concentration (229). However, while Na^+ is placed in the midpoint of the Hofmeister series and K^+ is a weak chaotrope, the dielectric constant at the headgroup reduces in the presence of Na^+ ions, but is hardly influenced by the presence of potassium. We note, that simulations have shown the headgroup dielectric constant strongly varies with the hydration state of the headgroup, e.g., at 8 water per headgroup, the dielectric constant in PCs was simulated to be 8, while at full hydration it rises to 30 (230). That is, kosmotropes being in concurrence with the interfacial water do increase the overall dielectric contrast by lowering the headgroup dielectric constant, which explains the less weakened VdW force in the presence of NaCl. We note, while the static dielectric contrast reduction can account for a Hamaker constant penalty of 50% due to a spatial redistribution of ions (201), at high salt concentrations the optical (high

frequency) dielectric responses becomes dominant due modified ionic polarization in response to spontaneous charge fluctuations. As a consequence of a reduced VdW force (weakened bilayer attraction), entropic mixing contributions to swelling have also been proposed (see Petrache et al. (201)), but primarily the swelling is driven by an decrease in the dielectric contrast by lipid headgroup and the solution.

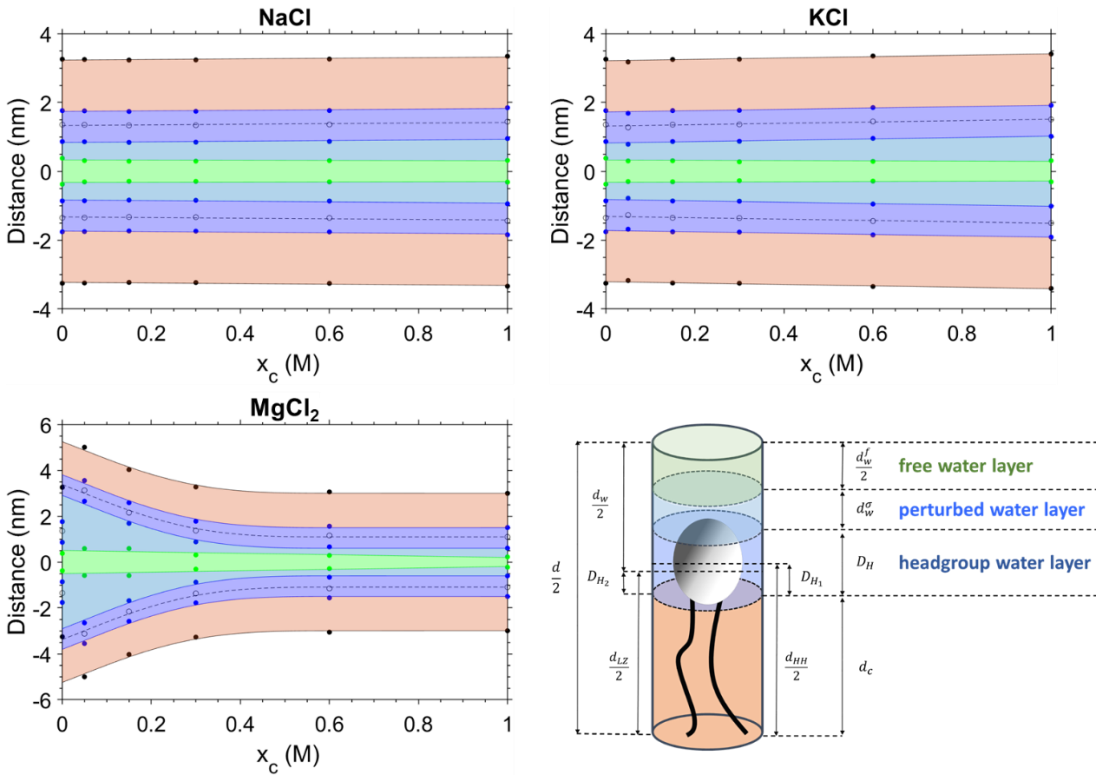

Figure 5.2 Adjacent monolayer and the confined water regions under the influence of NaCl (top left), KCl (top right) and $MgCl_2$ (bottom left). The solid black lines indicate the position of the methyl trough region and the dashed black lines the position of the phosphates. The blue lines indicate inner and outer headgroup boundaries, and the light green lines indicate the boundaries between perturbed and free water regions. The three water layers are colour-coded blue (headgroup water), light blue (perturbed water) and light green (free water).The three water layer model is displayed in the bottom right (scheme taken from our recent publication (1)).

Figure 5.3 presents the determined structural layer thicknesses in detail. As mentioned, *d*-spacing increases due to the screening of the VdW attractive force proportional to increasing salt concentration. However, $MgCl_2$ displays a different behaviour. At low salt concentration, membrane unbinding is nearly achieved due electrostatic repulsion. At high salt concentrations, when the electrostatic repulsion is entirely screened, the vesicles contract and concomitantly the *d*-spacing decreases.

We also observe a practically constant Luzzati membrane thickness, d_{LZ}, for the monovalent salts, which is consistent with previous studies on PC membranes (201, 203, 223, 231). As ions require a polar entity to bind to, provided by the lone electron pairs of the headgroup's oxygen atoms, the affinity to bind at the headgroup is predominant (232). The hydrocarbon chains are in contrast apolar; ions therefore do not bind to the tail region and cannot reduce chain splay in a direct manner. Cations can only interact on the chain packing indirectly by changing the hydrational state of the headgroup. Observing the influence of the divalent cation Mg^{2+}, within errors, the membrane bilayer thickness remains constant up to 1 M salt. This was also found for Ca^{2+} at lower salt concentrations. However, from 0.6 to 5 M a significant rigidification of the bilayer was observed (203). This membrane rigidification in turn reduces the repulsive Helfrich undulations force and does in part explain a reduced water layer thickness going hand in hand with reduced membrane fluctuations. Our data up to 1 M salt concentration does not allow such conclusion because a significant drop in the bending modulus is not confirmed. Thus, the repulsive fluctuation forces are not significantly changed by the addition of NaCl, KCl or $MgCl_2$ up to 1 M.

Despite the unchanging bilayer thickness, membrane fluctuations, dw^{σ}, do increase. We note, that the modified Caillé theory measures fluctuation through the η parameter, which is dependent not only on the bending modulus, K_C, but also the compression modulus, B. What we observe here in the increasing fluctuation distance is likely caused by an increase in the bulk compressibility of the MLVs. Following the theoretical model for calculating the free energy profiles of DPPC in the presence of $CaCl_2$ (233), we are similarly arguing that weakened VdW forces will lead to a shallower free energy minimum. Therefore, whilst the membrane rigidity does not significantly change when compared to the 0 M case, adjacent bilayers deviate to larger distances and are kept less strictly bound in place, as per the increase in disorder of the 2nd kind being mainly influenced by the bulk compression modulus.

At higher salt concentrations of $MgCl_2$, i.e., once the electrostatic repulsion force is entirely screened, the membrane fluctuations, dw^{σ}, decrease with respect to the pure DPPC behaviour at 50 °C. As the polar interface becomes more saturated with

Mg^{2+} ions it is also becoming more dehydrated, since water molecules at the headgroup are now replaced with ions. This dehydration goes hand in hand with an increase in the VdW force as is observed for poorly hydrated phosphatidylethanolamine bilayers (1), and DPPC membranes under the influence kosmotropic humectants (138). As discussed above, the Hamaker constant is primarily influenced by the dielectric contrast between the lipid and solution. Thus, due to the strong kosmotropic character of Mg^{2+} it expected that the VdW force increases due to the dominant decrease the dielectric constant of the lipid headgroup (230). However, we would like to remark that we are not excluding the possibility that that the multilamellar membrane stack is influenced by a change in both the VdW and Helfrich force. An increase in the VdW force (due to an increased dielectric contrast), as well as slight reduction in the Helfrich undulation force caused by an increase in bending rigidity of the membrane, would indeed explain a decrease in dw^{σ} observed for $MgCl_2$. That is, in our experiments, an increase in d_{LZ} might have been obscured by experimental errors.

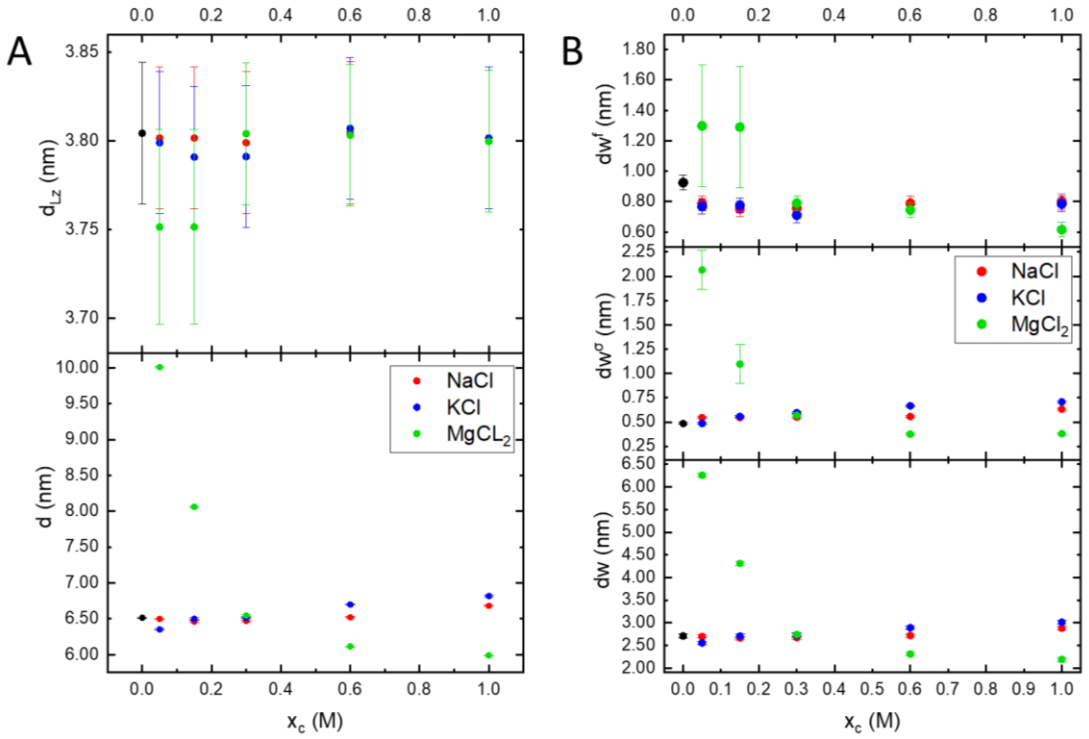

Figure 5.3 Structural parameters of DPPC under influence of addition of NaCl, KCl and $MgCl_2$. (A) Trend of the bilayer thickness, d_{LZ} (top) and overall *d*-spacing (bottom) as a function of salt concentration is given. (B) The thickness of the free water layer (top) and perturbed water layer (middle) and the overall water layer (bottom) is displayed.

Above 0.3 M salt concentration, the overall water layer thickness, d_W, and fluctuation layer thickness, dw^{σ}, rank in the order of $MgCl_2$ < NaCl < KCl. Interestingly, this order also follows the cationic Hofmeister series, with K^+ displaying the weakest ionic potential and Mg^{2+} the strongest. The affinity of membrane binding can be explained by an ions increase in ionic potential which is reflected in the increase of the bare ion radius to the hydrated ion radius. These radii increase by 2.49, 3.76 and 5.94 times for K^+, Na^+ and Mg^{2+}, respectively (216). As discussed above, an increasing binding affinity to headgroup is confirmed in the same order, both experimentally and by simulations (214, 215). Therefore, it becomes plausible that the binding of salt to the membrane is influencing fluctuations in a manner consistent with the Hofmeister series.

Concerning the free water layer, d_W^f, under the influence of the monovalent salts a slight decrease is observed initially when compared to the pure DPPC. Thereafter its value remains within errors constant. This trend is inverted for the divalent salt $MgCl_2$, chiefly due to the strong electrostatic repulsion at low salt concentrations. Nevertheless, once restabilized above 0.3 M, the trend is clearly decreasing. For the monovalent salts, we can summarise that both the overall water layer increase is dominated by the increase in the perturbed layer thickness, but hardly influenced by the free water layer thickness. For $MgCl_2$ the picture is starkly different, where progressive electrostatic screening causes the free layer to shrink as the entire multilamellar systems contracts under the increase of the VdW force and a possible reduction of the fluctuation forces. All the observed structural trends are further elucidated by the consideration of the number of water molecules in each of the discerned water regions.

As alluded to by the unchanging membrane thickness (Figure 5.3A), also the area per lipid does not change within the studied salt concentrations (Figure 5.4A). Only at small $MgCl_2$ concentrations (0.05 and 0.15 M), we do observe a slight decrease in the bilayer thickness, d_{LZ}, and accordingly an increase in the area per lipid. Although these changes are not very significant, a slight increase in membrane fluidity (decrease in K_C) can be interpreted as an impurity effect. At low Mg^{2+} concentrations,

a strong heterogeneity of ordered patches (lipid-salt complexes) within the fluid bilayer phase might actually cause a decrease in membrane rigidity. Similarly, cholesterol is known to enhance bilayer fluidity at low concentrations in the membrane (1-5 mol%), while inducing bilayer rigidification at concentrations above 10 mol%, which was explained through cholesterol's impurity effect at low concentrations (234). As expected the headgroup waters, n_W^H (Figure 5.4 B), follow the same behaviour as the area per lipid. The most interesting results come from the perturbed water numbers, which above 0.3 M coincide with the cationic Hofmeister series (Figure 5.3 C). Despite the overall water layer thickness increasing slightly for the monovalent salts (Figure 5.3 B), the number of free waters do remain constant (Figure 5.4 D), i.e., being mostly unaffected by the salt concentration. As ever, $MgCl_2$ exhibits vastly different behaviour compared to the monovalent salts. All its waters consistently decrease in each of the distinguished layers. Indeed, at 1 M salt concentration the free layer is so constrained that the number of waters has reduced by over 50% compared to the lowest salt concentration, and roughly only 60% of the overall waters are left, when compared to pure DPPC system. As mentioned above, the reduced number of waters at higher $MgCl_2$ concentration does confirm our interpretation, that likely both the VdW force increase and Helfrich force decrease lead to the mechanical stabilisation of the MLVs, similarly to the salt-induced membrane rigidification as observed in the presence of $CaCl_2$ (203).

Table 5.1 Number of salts per lipid under the assumption that the salt concentration of interlamellar water and the excess water regions is the same.

x_c (M)	NaCl	KCl	$MgCl_2$
0.05	0.026	0.025	0.062
0.15	0.078	0.079	0.128
0.3	0.156	0.160	0.160
0.6	0.318	0.338	0.270
1	0.562	0.588	0.428

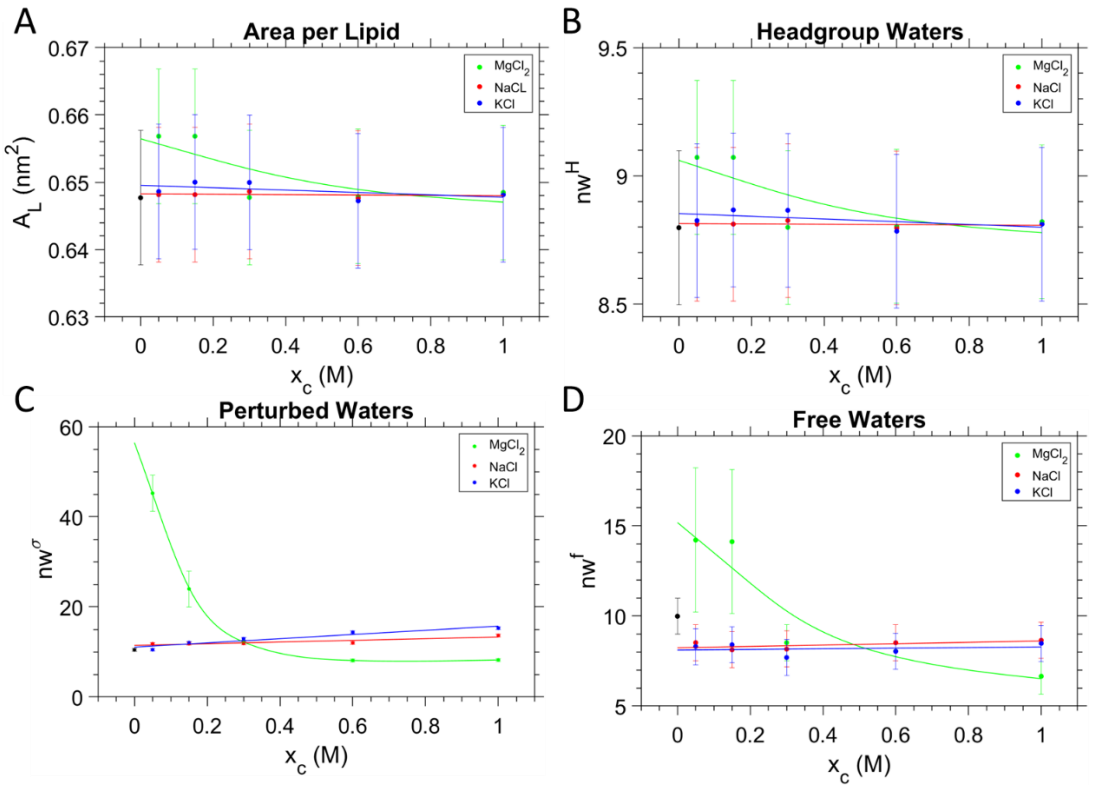

Figure 5.4 Hydration properties of DPPC at 50 °C under the influence of NaCl, KCl and $MgCl_2$. (A) Area per lipid (B) Number of waters in the headgroup region (C) Number of waters within the perturbed water region (D) number of free waters.

In Figure 5.5 we are comparing the four DPPC systems at 0 and 1 M salt concentration, respectively. As observed in the electron density profiles (EDPs; Figure 5.5 A), the overall water layer decreases under the influence of the strong kosmotrope Mg^{2+} and slightly increased in the presence of the neutral Na^+ and even more so under the influence of the weak chaotrope, K^+. The latter vesicle swelling is primarily driven by a reduction of the dielectric constant of the water (decrease in VdW force). As clearly shown in the comparison of the structural layer thicknesses d_{LZ}, d_W, $d_W{}^\sigma$, $d_W{}^f$ (Figure 5.5 B), the main contribution to changes in the *d*-spacing arises from the overall water layer thickness and is hereby mostly dominated by changes in the perturbed water layer thickness. Although hardly any change is observed in number of headgroup waters (figure 5.4), it must be remarked that in its calculation no replacement of headgroup water by cations has been taken into account. Thus the given water numbers are likely too high, in particular for the $MgCl_2$, with the Mg^{2+} having a strong binding constant towards DPPC. The binding constant, *K,* for Mg^{2+} is; K_{Mg} = [lipid Mg2+]/([lipid] [Mg2+]) was experimentally found to be 2.5

± 0.7 M^{-1} (232). In Table 5.1 the number salt ions per lipid are listed for all salt concentrations. For the 1 M solution of $MgCl_2$, for each lipid 0.428 cations are found in total water volume per lipid. That is, we can estimate the [lipid Mg2+]/[lipid] ratio is about 1:1. Hence the number of waters per headgroup reduces at least by one or even greater, depending the coordination number of Mg^{2+} within the headgroup region (cp. Figure 5.4 B). The reduction of n_W^H is expected to be roughly twofold lower for Na^+ (note, the a binding constant K_{Na} = 1.25 M^{-1} has been reported (235)), i.e., having roughly half the potential to replace water at the interface, and for K^+ we expect n_W^H to be nearly unchanged, since K^+ hardly binds to the headgroup (214).

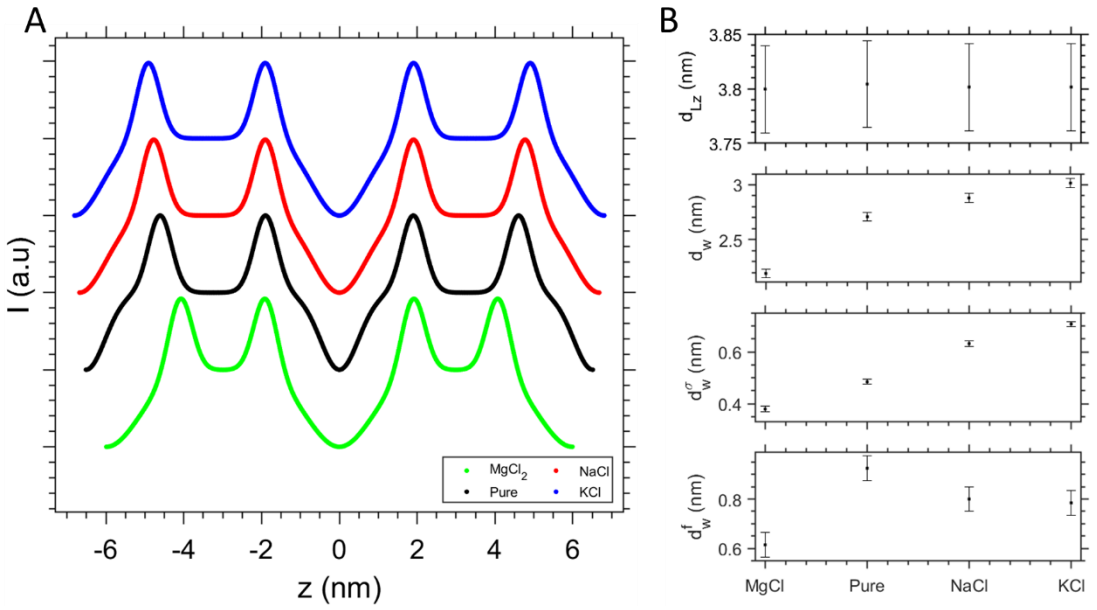

Figure 5.5 Structural comparison of DPPC with 0 M salt and 1M of MgCl2, NaCl and KCl. (A) Electron density profiles from bottom to top: 1 M $MgCl_2$, 0 M salt, 1 M NaCl and 1 M KCl. (B) Structural parameters of d_{LZ}, d_W, d_W^σ, d_W^f and for 1 M $MgCl_2$, 0 M salt, 1 M NaCl and 1 M KCl.

5.4 Conclusion

DPPC was investigated with SAXS in the fluid lamellar phase of multilamellar vesicles at 50 °C. Hereby the influence of two monovalent salts (NaCl and KCl) and one divalent salt ($MgCl_2$) on the hydrational state and structure of the PC bilayer stacks has been studied with salt concentrations varying from 0 to 1 M. It was found that the influence of the monovalent salts onto the bilayer rigidity is not significant over the studied salt range. This is slightly different for divalent salts, where the influence

of $MgCl_2$ is onto the bilayer rigidity is subtle, displaying a slight membrane fluidisation at low salt concentrations (0.05 and 0.15 M). The strong vesicle swelling at low $MgCl_2$ concentrations is due to unscreened electrostatic repulsion forces, whereas the vesicle stabilisation at high salt concentration (0.6 and 1 M) is interpreted as an increase in both the membrane bending and bulk compression moduli. The swelling effect at low salt concentrations is interpreted as an impurity effect given at low [lipid Mg^{2+}]/[lipid] ratios. The stabilisation of the MLVs at high salt concentration is most likely a combination of increased VdW forces and decreased Helfrich forces.

The swelling of vesicle upon increased monovalent salt concentration is understood throughout the reduction of dielectric constant of the solution in the presence of salt. That is, the dielectric contrast between lipid and aqueous solution decreases, leading to a decrease in VdW forces coinciding with an increased bulk compressibility of the MLVs.

The Hofmeister series is reflected in the membrane binding affinity of the three salts studied. The key structural parameter reflecting this trend is the perturbed water layer thickness. Under the influence of the kosmotropic Mg^{2+} ions the membrane perturbation decreases, while the water structuring neutral Na^{+} and slightly chaotropic K+ ions induce an increase in the perturbed water layer thickness. The studied cations are more dominantly influencing the bulk compressibility of the vesicles, and less so the membrane rigidity. None the less, these findings do suggest that membrane fluctuation does somewhat follow the cationic Hofmeister series.

Chapter 6 General Conclusion and Outlook

6.1 General Conclusion

The interaction of lipids with water, in particular interfacial water, is of great interest because of its prevalence in various biological scenarios, but also in several industrial applications. A deeper understanding of this interaction will aid in the improvement of models which simulate biological processes. The extent of hydration at the membrane interface plays an important role in cell dynamics, and cell fusion (101). Therefore, the main objective of this research was to establish a methodology to define the water confined between lipid bilayers as given in lyotropic liquid crystals. Two such liquid crystals were analysed, namely the lamellar and inverse hexagonal phase. We have primarily focused on the most biologically relevant lamellar phase. The novelty of the this project at large is the introduction of the *three-water-layer* model, which has been applied to each system studied in chapters 3-5, primarily using small angle x-ray scattering for the nanostructural characterisation of the systems.

Chapter 3 derives this model and defines its parameters all of which can be obtained using SAXS. Volumetric data may be used to supplement the SAXS data; in the case of chapter 3, volumetric data was used to estimate to position of the Gibbs diving surface through the newly introduced parameter D_{H2}. The method outlined in appendix A shows that this distance can be calculated without the need for time consuming gravimetric measurements. The three-water-layer model categorises the inter-lamellar water into three distinct layers associated with each lipid. These layers tend to increase with the swelling of vesicles, with the notable exception of DMPE, which apparently constricts as a function temperature. Applying the three-water-layer model, it was found that the free layer is absent in DMPE, suggesting a diminished hydration compared to the PC lipids studied. This lack of inter-lamellar waters likely has an influence on the dynamics of the DMPE membrane which was seen to fluctuate to smaller distances as a function of temperature. The smaller headgroup volume of PEs is also reflected in the lower number of waters in the headgroup regions, which diminishes the dielectric constant significantly in the lipid headgroup region, leading to an enhanced attractive VdW force due to an overall

enhanced dielectric contrast between lipid and the water phase. However, the overall interplay with repulsive hydration force is still not entirely understood. Nevertheless, our observation also suggest a more significant role water plays in inter-membrane interactions but also in membrane dynamics at large.

Also in chapter 3, it was demonstrated how the three-water-layer model might be used to better estimate membrane structure. Here, the model was used to estimate headgroup tilt, which was calculated to decrease relative to the bilayer normal as a function of temperature. Whilst this result is unsurprising, this is the first instance of the behaviour being observed using purely SAXS data.

Chapter 5 progresses in a similar manner, from studying pure lipid/water systems to studying lipid/ion solution systems. The effect of water on membrane dynamics is best observed for the divalent $MgCl_2$. Being a strong kosmotrope, having high affinity for membrane binding, the Mg^{2+} ions replace interfacial water at the lipid headgroups. Incidentally, the perturbed water region decrease to the smallest value of all salts studied at the highest salt concentration (1M). Again, alluding to the role water plays on lipid dynamics. However, the effect of ions on the VdW attractive force cannot be excluded as having a significant influence also. The increase in VdW force (observed by the water layer shrinking) apparently goes hand in hand with a diminishing fluctuation distance. This interpretation applies to both a pure DMPE/water system and DPPC with the addition of $MgCl_2$. Potassium ions on the other hand, are weakly chaotropic and as discussed in Chapter 5, do not have as strong an affinity for the membrane interface. They therefore will be dispersed in the water phase, leaving a surplus of waters at the interface. This may cause a slight increase in membrane fluidity, which is somewhat apparent for KCl at low salt concentrations, although the experimental errors in this case are too large for this interpretation to be conclusive. It is likely a more detailed investigation of the lipid volume under the influence of specific ions is needed.

What was most interesting about the results in Chapter 5 was the comparative behaviour of all salts in the higher concentration range (> 0.3 M). This regime proceeded the effects of enhanced fluidity and swelling observed for $MgCl_2$. Here we observe a pattern for membrane fluctuation which coincides with a cationic

Hofmeister series. Whilst is already established that ion binding does also follow a Hofmeister series, the implication that this also influences membrane dynamics is interesting. Similarly to what was observed in Chapter 3, the incorporation of ions into the water phase is clearly having an effect on intermembrane forces. What is unique in the case of ions is the apparently unchanging membrane thickness, yet with an apparent increase in the Helfrich undulation force, observed from the membranes fluctuating to larger distances. This is in contrast to the pure lipid/water systems in Chapter 3, where an increase in Helfrich undulation forces occurs accordingly with a thinning of the membrane thickness (the main influence arising from the bending modulus). Whereas in chapter 5, the main influence is given by changes in the bulk compressibility, which increases under the influence of chaotropic cations. This influence on membrane dynamics with the addition of ions may also relate to the number of lipids a single ion binds to (see Table 5.1).

Chapters 3 and 5 were the application of the three-water-layer model to lamellar systems with and without the presence of ions. Chapter 4 is an investigation into the water core shape and stability in the inverse hexagonal phase. In particular, how the shape is related to membrane dynamics, according to the three-water-layer model. Remarkably, the hexagonal crystal lattice apparently fluctuates to greater distances the more circular the confined water core is (this may also be interpreted as a higher membrane fluidity when the water core is most circular; at the same time, the error margins are too big to ascertain this finding conclusively). The addition of longer chain DPPE to the POPE host lipid maximised the circularity of the water core at a concentration of 9 mol% DPPE. At higher or lower concentrations, the value of circularity deviated from being perfect circular. This value of 9 mol% also conveniently matched the 9% excess surface area coverage of a circle inscribed onto a hexagon. Volumetrically, it is plausible that 9 mol% DPPE accounts for the area excess in the packing frustration.

What is of key interest in Chapter 4 is the relationship between confined water geometry and its influence on membrane dynamics and stability. Concerning the waters confined to each classified sub-layer, there is little change to be seen across the concentration range, although the 9 mol% does display a very slight increase in

its perturbed waters. This behaviour in the hexagonal phase is remarkably different to what is observed in the lamellar phase, where the interplay of volumetric changes between the perturbed and free layers are inversely proportional to each other. Further, we observed the shape of the apparent free water region resembling a smaller hexagon rotated 30° relative to the Wigner-Seitz unit cell. This observation is apparent in the electron density distribution (see Figure 5.7 and Appendix B). Here, we see a broadening of the phosphate distribution orientated to the direction of the corner of the unit cell, which does constrain the distribution in the water region to a shape resembling a well-rounded hexagon. Naturally, this observation goes hand in hand with the calculated fluctuation distances in that direction. Although the representation of the inverse hexagonal phase as an EDP contour map has been quite common, there has seldom been an interpretation of water core pattern in this profound manner.

These results from Chapters 3-5 can be useful for industrial formulations which employ lipid membranes and water, such as those self-assemblies used in cosmetics, pharmaceuticals and the food industry. These investigation have scrutinised lipid membranes under different environmental conditions, but also with additives in the water phase. In particular, ions which are frequently found in human biology were studied. Special attention was given to the understanding and behaviour of the membrane dynamics and stability in each case. For this reason, the information garnered from this thesis would be useful in product formulations which incorporate water and emphasise the membrane or vesicle stability in conjunction with it. From Chapter 4, we have also developed a novel and interesting way to probe the size and shape of the cylindrical water core. This may be of particular interest to pharmaceuticals, because of the role the inverse hexagonal phase plays in the therapeutic delivery of, for instance, mRNA applied in COVID vaccines (236).

6.2 Outlook

For future research there are several interesting areas to investigate. The first concerns more ionic studies, but with an emphasis on ions which will have an affinity to the water as opposed to the membrane. As is well known, the anionic Hofmeister series is better resolved than the cationic series (237). Cations also have a preference for binding to the lipid headgroup leaving the anion to be dispersed in the water phase (217). Currently, we have conducted a study of altering the membrane interface and observing the effect this has on the water layer. For this reason, it would be interesting to observe how specifically altering the water structure will influence the membrane dynamics, if at all.

Concerning the behaviour of water in confinement, differential scanning calorimetry (DSC) is a useful method to measure the freezing behaviour of water confined between membranes (238). In particular, DSC studies have observed distinct water freezing events (239) relating to the intra and extra-vesicle water. In one particular study three classes of water (240), including a regime of water that never froze, has been observed for water confined between membranes. The design of an experiment to observe different freezing regimes could support the hypothesis in this study about distinct water species. It is likely that these measurements would need to be performed at minimum water hydration for the specific lipid. This would negate as much as possible, the influence of bulk water freezing, focusing more on the confined water. A slow cooling ramp (< 1 °C min^{-1}) would also be beneficial to allow subtle signals from waters of different dynamics to be recorded.

Finally, in order to form a fuller picture of water dynamics, nuclear magnetic resonance (NRM) experiments may be performed to further support the SAXS experiments. NMR studies are able to investigate water dynamics near the membrane interface (196). Combining SAXS with NMR would form a model of the membrane structure and dynamics (from SAXS) as well as the dynamics of the water (from NMR).

In addition to the real world industrial applications discussed above, the studies conducted within this thesis would be a useful tool in studying models which mimic

biological processes. Molecular dynamics simulations of the phospholipid membrane is an exciting field of research and a deeper understanding of the confined water layer region would better inform simulation studies. In particular, studies which measure intermembrane forces may be improved by detailed descriptions of the water sub-layers, according to the three-water-layer model. Since water is the key propagation medium for all intermembrane forces, consideration of the differences in water density, structure and its relationship with the membrane will improve our understanding and replication of biological processes, involving the cell membrane.

Appendix A: Supporting Information for Chapter 3

Content

- **Figure A1**: Common bilayer electron density profile (EDP) models.
- **Figure A2**: Examples of global fitting of SAXS data of DMPC, egg-PC and DOPC.
- **Table A1**: Lattice spacings and form factor values of DMPE.
- **Table A2**: Structural parameters of DMPC, egg-PC and DOPC (30 °C) and DMPE (60 °C).
- Derivation of the parameter D_{H2}.
- **Figure A3**: Refined membrane hydration.

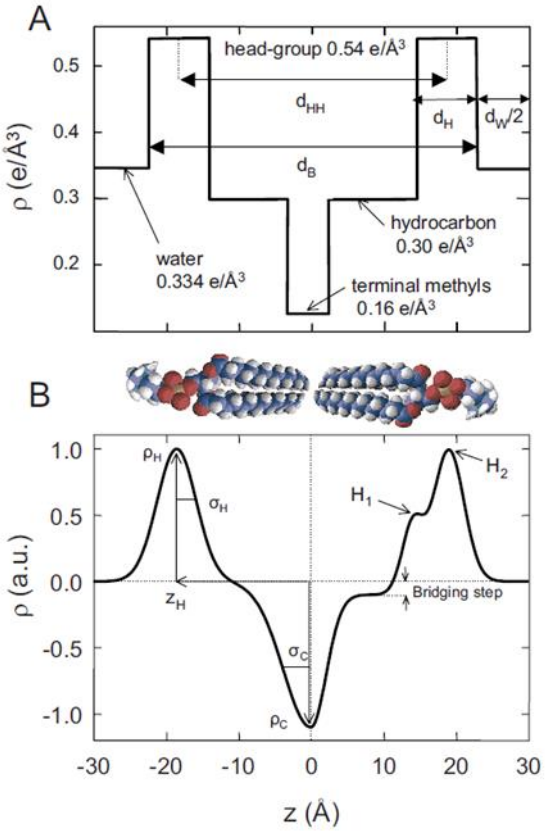

Figure A1 Common bilayer electron density profile (EDP) models. (A) A strip model and (B) two different Gaussian component models. The figure has been taken with permission from reference (57).

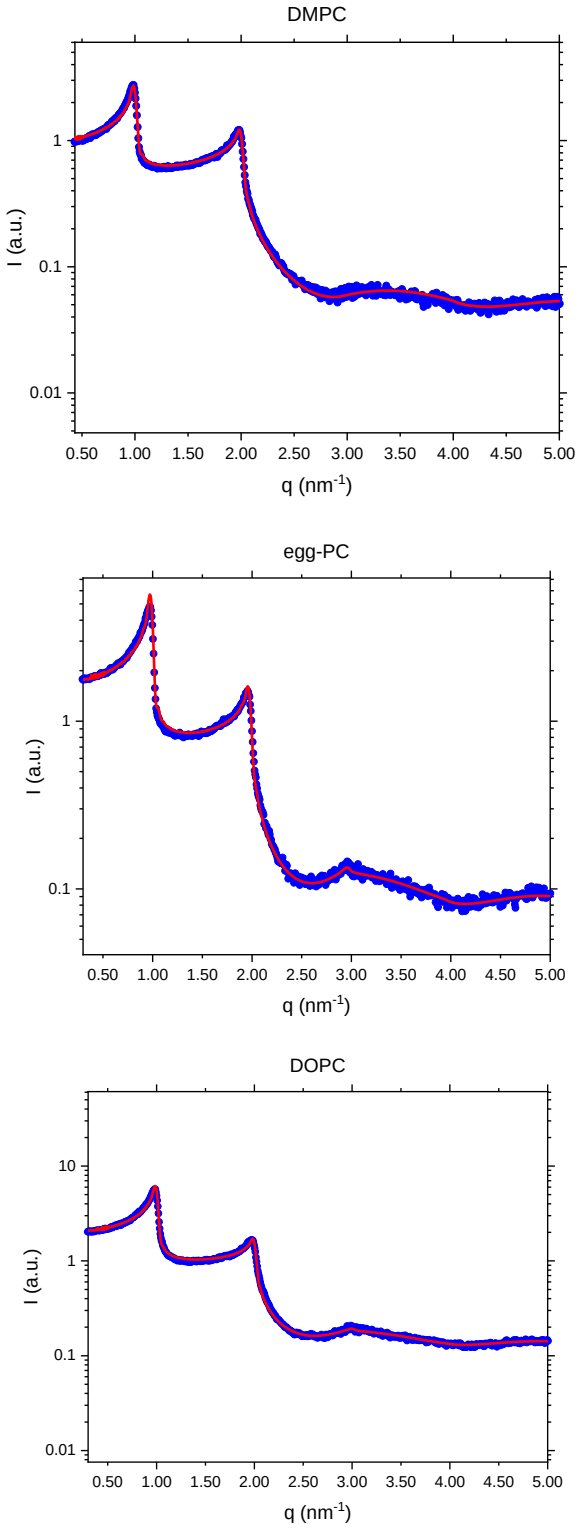

Figure A2 Global fitting of SAXS data of DMPC, egg-PC and DOPC at 30 °C (shown from top to bottom). Solid red lines give best fits.

Table A1: Lattice spacing and form factor values of DMPE.

		Fourier Coefficients F(h)/F(1)			
Temperature (°C)	**d-spacing (nm)**	**F(1)/F(1)**	**F(2)/F(1)**	**F(3)/F(3)**	**F(4)/F(1)**
57	4.935	-1.000	-0.227	+0.220	-0.276
60	4.902	-1.000	-0.231	+0.217	-0.268
62	4.87	-1.000	-0.244	+0.222	-0.259
65	4.839	-1.000	-0.243	+0.223	-0.255
67	4.815	-1.000	-0.234	+0.223	-0.262
70	4.785	-1.000	-0.240	+0.221	-0.261
72	4.765	-1.000	-0.237	+0.221	-0.254
75	4.736	-1.000	-0.232	+0.211	-0.230
80	4.69	-1.000	-0.240	+0.211	-0.248

Table A2: Structural parameters of DMPC, egg-PC and DOPC (30 °C) and DMPE (60 °C). Parameters are compared to literature values given in brackets.

Parameter	**DMPC (30 °C)**	**DOPC (30 °C)**	**Egg-PC (30 °C)**	**DMPE (60 °C)**
***d*-spacing (nm)**	6.27 (6.27 [37])	6.27 (6.31 [2])	6.35 (6.63 [2])	4.90 (4.83 [3])
d_{HH} **(nm)** (head to head)	3.44 (3.60 [2])	3.63 (3.69 [2])	3.66 (3.69 [2])	3.61 (3.39 [3])
d_{LZ} **(nm)** (bilayer thickness by Luzzati)	3.49 (3.69 [2])	3.53 (3.59 [2])	3.56 (3.63 [2])	3.49 (3.41 (40))
A_L **(nm²)**	0.619 (0.596 [2])	0.723 (0.725 [2])	0.694 (0.694 [2])	0.582 (0.596 (40))
n_w **total** (per lipid)	24.1 (25.6 [2])	33.0 (32.8 [2])	31.8 (34.7 [2])	12.2 (11 (143))

Derivation of the parameter D_{H2}

D_{H2} can be derived from setting the **water volume in the headgroup regions** equal, using the excluded headgroup volume expression and Luzzati ansatz (27), respectively:

$$A_L = \frac{2V_L}{d_{Lz}} = \frac{2V_L}{d_{HH}+2(D_{H2}- D_{H1})} \quad \text{(A1)}$$

$$D_H A_L - V_H = A_L(D_H - D_{H2}) \quad \text{(A2)}$$

Inserting (A1) in (A2):

$$\Rightarrow \frac{2D_H V_L}{d_{HH}+2(D_{H2}- D_{H1})} - V_H = \frac{2V_L(D_H- D_{H2})}{d_{HH}+2(D_{H2}- D_{H1})}$$

$$\Rightarrow V_H = \frac{D_{H2}2V_L}{d_{HH}+2(D_{H2}- D_{H1})}$$

$$\Rightarrow V_H d_{HH} + 2V_H D_{H2} - 2V_H D_{H1} = 2D_{H2}V_L$$

$$\Rightarrow V_H(d_{HH} - 2D_{H1}) = 2D_{H2}(V_L - V_H)$$

$$\Rightarrow \boldsymbol{D_{H2} = \frac{V_H(d_{HH}- 2D_{H1})}{2(V_L-V_H)}}$$

Alternatively, one may set the **area per lipid expressions** equal that derive from McIntosh (43) and Luzzati (27) ideas, respectively:

$$A_L = \frac{2(V_L- V_H)}{d_{HH}-2D_{H1}} = \frac{2V_L}{d_{HH}+2(D_{H2}- D_{H1})}) \quad \text{(A3)}$$

$$\Rightarrow 2V_L d_{HH} + 4V_L D_{H2} - 4V_L D_{H1} - 2V_H d_{HH} - 4V_H D_{H2} + 4V_H D_{H1} = 2V_L d_{HH} - 4V_L D_{H1}$$

$$\Rightarrow 4V_L D_{H2} - 4V_H D_{H2} = 2V_H d_{HH} - 4V_H D_{H1}$$

$$\Rightarrow 2D_{H2}(V_L - V_H) = V_H(d_{HH} - 2D_{H1})$$

$$\Rightarrow \boldsymbol{D_{H2} = \frac{V_H(d_{HH}- 2D_{H1})}{2(V_L-V_H)}}$$

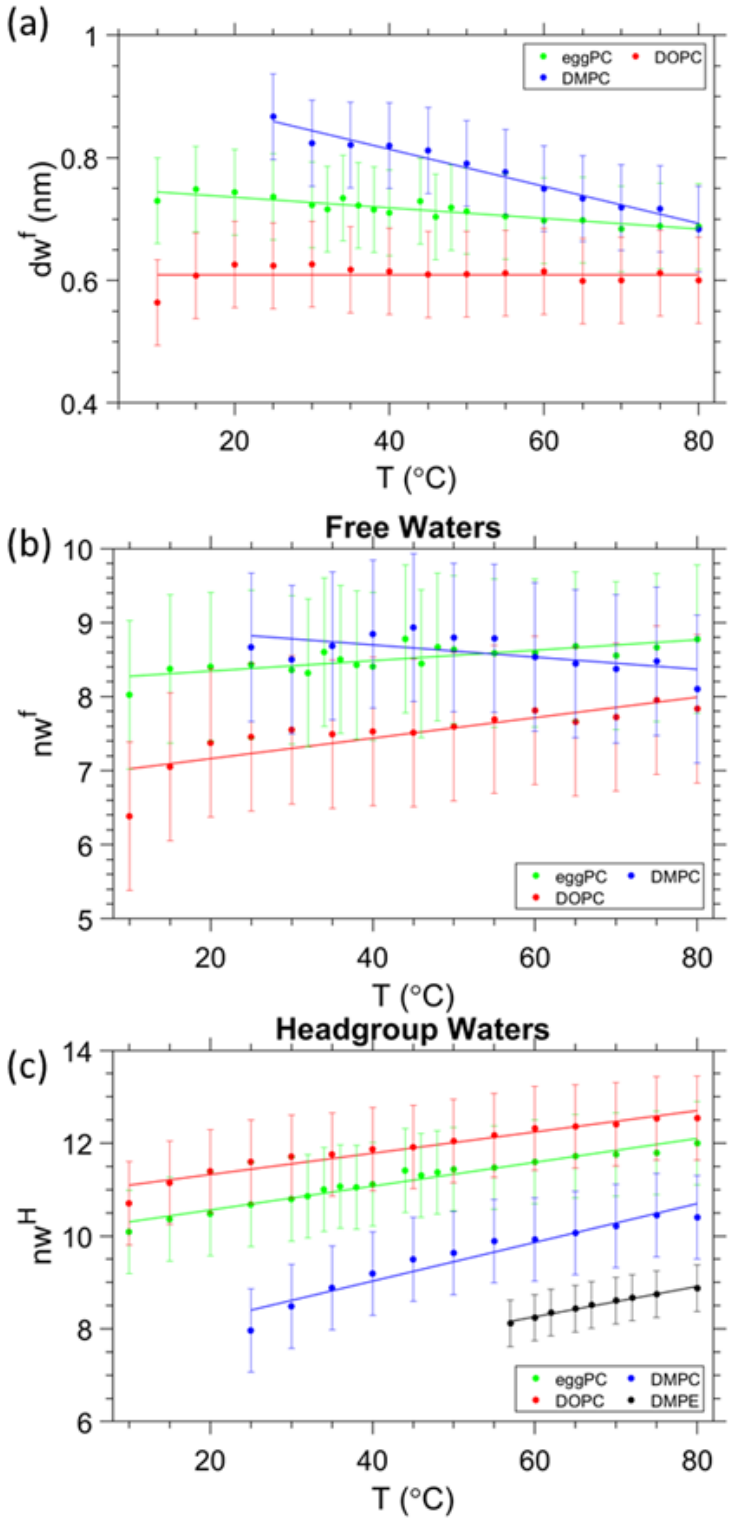

Figure A3 Refined membrane hydration. a) The refined free water layer thickness for the PCs is presented, using the linear regression of $D_H\,(T)$ obtained from DOPC and DMPE data, respectively. b) Refined number of waters in the headgroup region, and c) the refined number of water molecules in the free water layer are shown. Note, the perturbed water layer remains unchanged, when applying $D_H\,(T)$ instead of D_H = constant.

Appendix B: Supporting Information for Chapter 4

Contents

Fitting of the diffraction pattern

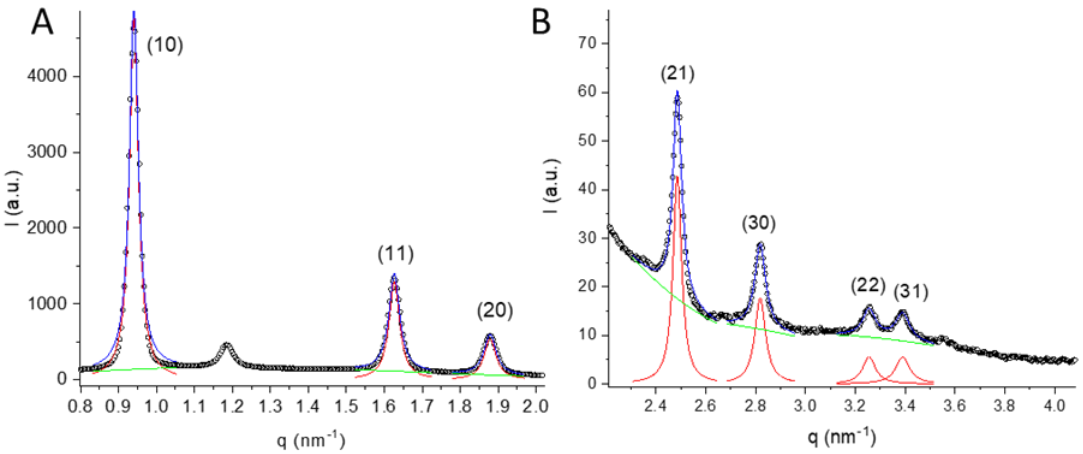

Figure B1 SAXS diffraction pattern of POPE with 12 mol% of DPPE. (A) Higher intensity peaks (10), (11) and (20) are shown, and in (B), the lower intensity peaks (21), (30), (22) and (31) are displayed. All peaks are fitted by Lorentzian distributions (red-lines), the diffuse background was fitted with a polynomial of second order (green lines) and the overall resulting fits are shown with blue lines. All experimental results are summarized Table B1.

Best phase choices for F(21), F(22) and F(31)

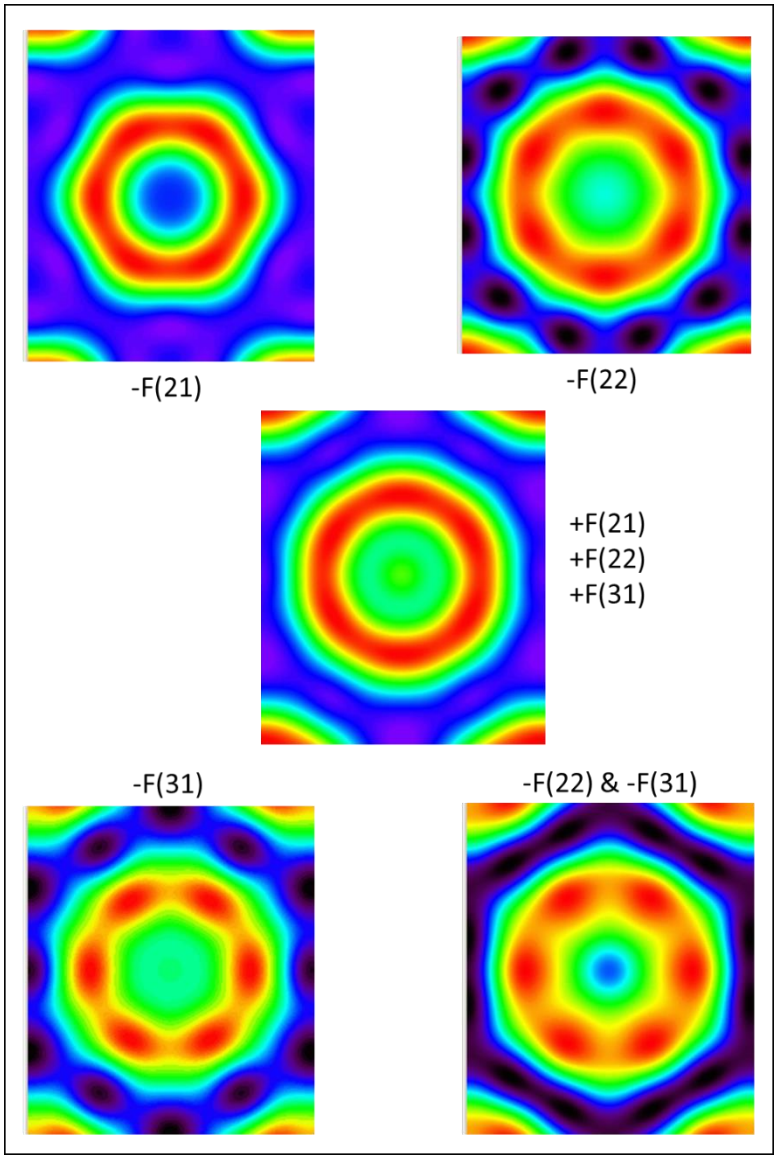

Figure B2 Demonstration of best phase combination for the POPE sample with 9 mol% of DPPE. Due to experimentally reported zero-crossing of the form factor near the (21) reflection (63), its best phase choice has been checked for all electron density map calculations. Additionally, the two weakest reflections (22) and (31) reflections were checked for their best phase choices. All these alternative phase choices led to an enhanced kurtosis (peakedness) within the unit cell and hence have been excluded. This phase choice method has been originally developed by Luzzati and co-workers (241), and follows the idea to identify electron density map, displaying the smoothest interfaces. Moreover, the best phase choice for F(21), F(22) and F(31) (all positive), leads also to the lipid/water interface with the highest circularity.

Schematic of the encasing triangle used in circumference and area calculation

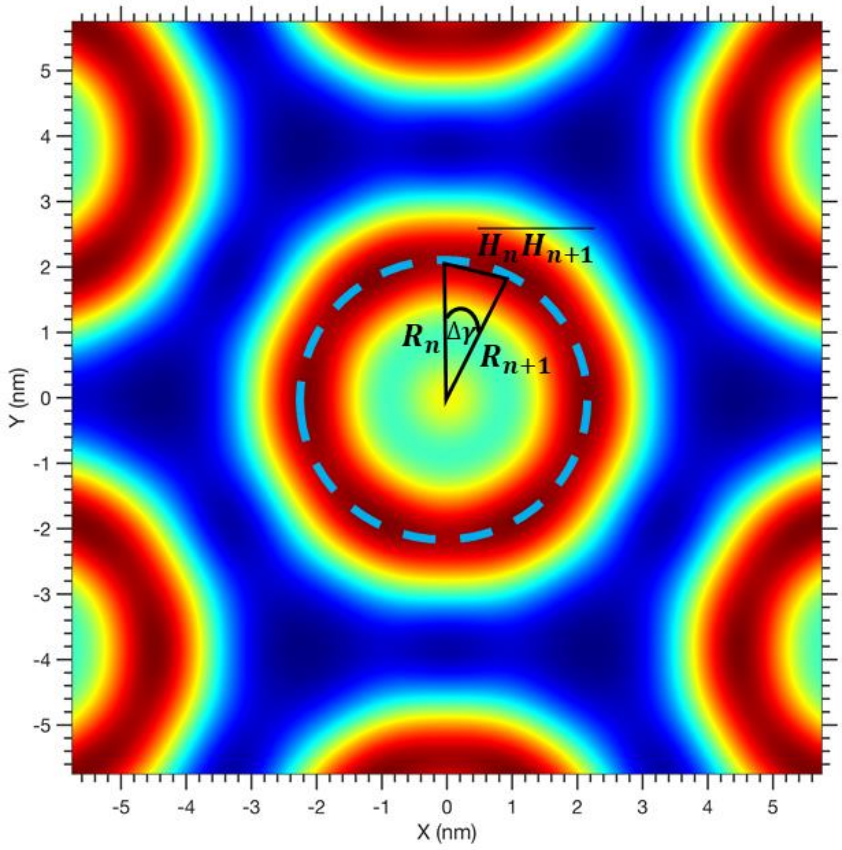

Figure B3 Schematic representation method used to calculate the circumference and area of the water core, with the phosphate position denoted by the light blue dotted line. $\Delta\gamma$ was set at 1°. The summation $\sum_{n=0}^{n=30} \overline{H_nH_{n+1}}$ produces the approximate arch length of a 30° segment with the area of the encasing triangle used to calculate the total area of the water core (note, $\Delta\gamma$ is not to scale).

Peak-shape progression in <10> and <11> direction and MCT fits

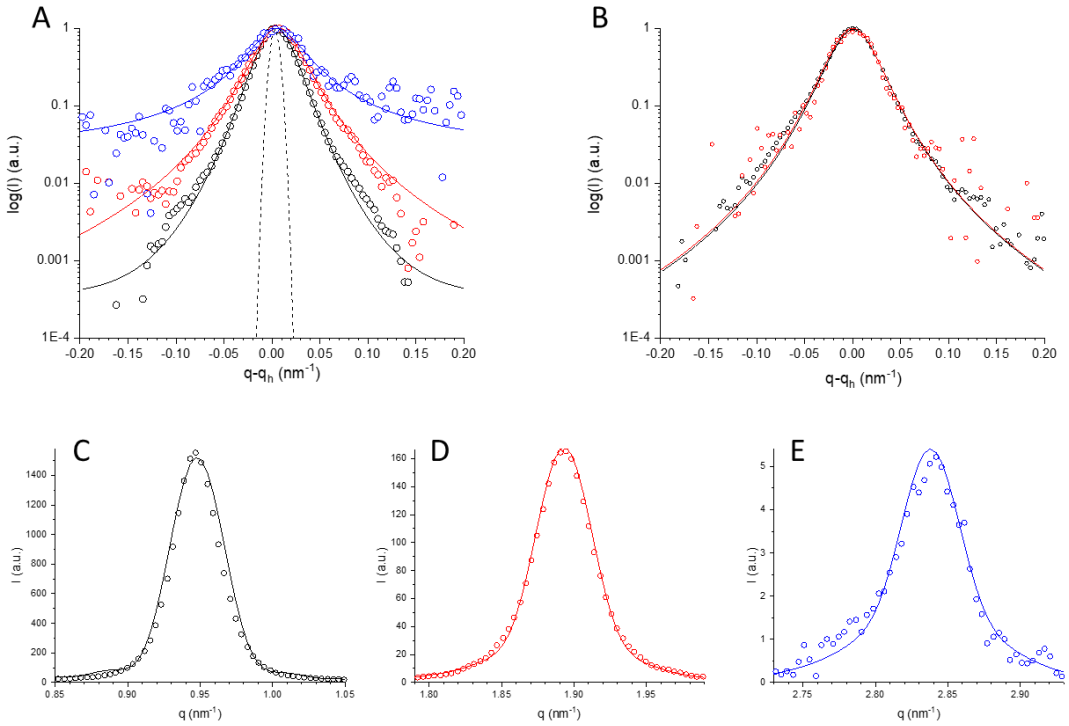

Figure B4 (A) The peak shape progression in the <10> direction shows an increase in width as function of the order (peak (10) – black, (20) – red, (30) – blue, instrumental width – dashed line), which demonstrates disorder of 2nd kind with strong undulations within this set of planes. (B) The peak shape progression in the <11> direction displays a constant width as function of the order (peak (11) – black, (11) – red), which demonstrates dominating thermal disorder instead (all lines in panel A and B display Pearson VII fits, helping to guide the eye). (C-D) Modified Caillé Theory based fits in the <10> direction: from left to right the (10), (20) and (30) peaks were fitted, resulting mean square fluctuations σ = 0.3 nm. As an example, the sample POPE with 9 mol% DPPE is presented.

Turnover curves: L_α to H_{II} phase transition

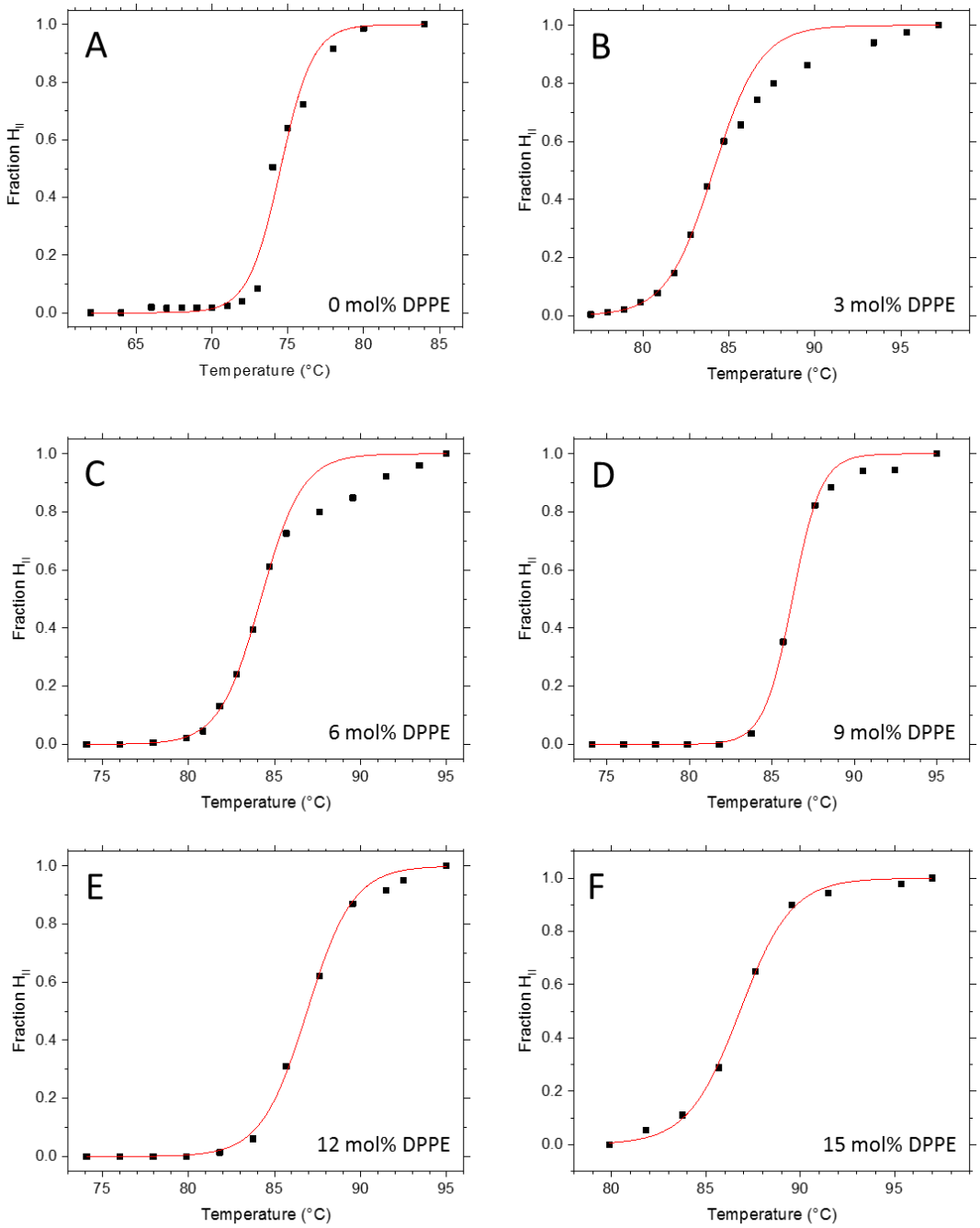

Figure B5 Fraction of the inverse hexagonal phase as function of the DPPE concentration. Mixtures of POPE/DPPE ranging from 0 to 15 mol% DPPE were heated from L_α to H_{II} phase. The intensity of the first order peaks was used to calculate the fraction of the inverse hexagonal phase according to *Fraction* $H_{II} = I(H_{II})/[I(H_{II}) + I(L_\alpha)]$. Best fits using the logistic function with setting the minimum and maximum values to 0 and 1, respectively, are shown in red. Panel A data is taken from Rappolt et al. (156).

Table B1 Structural parameters for the calculation of the electron density maps in Figure B5.

Sample	Temperature (°C)	Lattice spacing, *a* (nm)	Miller indexes: *h, k*	I_{hk}/I_{10} [a]	$F_{h,k}/F_{10}$ [b]
0 mol% DPPE	80.0	7.12	1, 0	1.0000	+1.00
			1, 1	0.3608	-1.04
			2, 0	0.1752	-0.84
			2, 1	0.0069	+0.22
			3, 0	0.0058	+0.23
			2, 2	0.0036	+0.21
			3, 1	0.0019	+0.16
3 mol% DPPE	89.5	7.66	1, 0	1.0000	+1.00
			1, 1	0.3168	-0.97
			2, 0	0.1457	-0.76
			2, 1	0.0054	+0.19
			3, 0	0.0058	+0.23
			2, 2	0.0028	+0.18
			3, 1	0.0015	+0.14
6 mol% DPPE	89.5	7.73	1, 0	1.0000	+1.00
			1, 1	0.3376	-1.01
			2, 0	0.1540	-0.78
			2, 1	0.0066	+0.22
			3, 0	0.0072	+0.26
			2, 2	0.0018	+0.15
			3, 1	0.0011	+0.12
9 mol% DPPE	90.5	7.66	1, 0	1.0000	+1.00
			1, 1	0.3265	-0.99
			2, 0	0.1544	-0.79
			2, 1	0.0060	+0.20
			3, 0	0.0070	+0.25
			2, 2	0.0020	+0.15
			3, 1	0.0013	+0.13
12 mol% DPPE	91.5	7.72	1, 0	1.0000	+1.00
			1, 1	0.3319	-1.00
			2, 0	0.1548	-0.79
			2, 1	0.0068	+0.22
			3, 0	0.0061	+0.23
			2, 2	0.0029	+0.19
			3, 1	0.0012	+0.12
15 mol% DPPE	91.5	7.70	1, 0	1.0000	+1.00
			1, 1	0.3201	-0.98
			2, 0	0.1521	-0.78
			2, 1	0.0063	+0.21
			3, 0	0.0059	+0.23
			2, 2	0.0027	+0.18
			3, 1	0.0011	+0.12

[a] All I_{21} and I_{31} intensities were divided by 2 due to their 2-fold higher multiplicity.

[b] Amplitudes $F_{hk}/F_{10} = \sqrt{(I_{hk}/I_{10})}\ Lor_c$, i.e., the Lorentz correction (Lor_c) was 1, √3, 2, √7, 3, √12 and √13 applied.

Electron density maps of POPE/DPPE mixtures

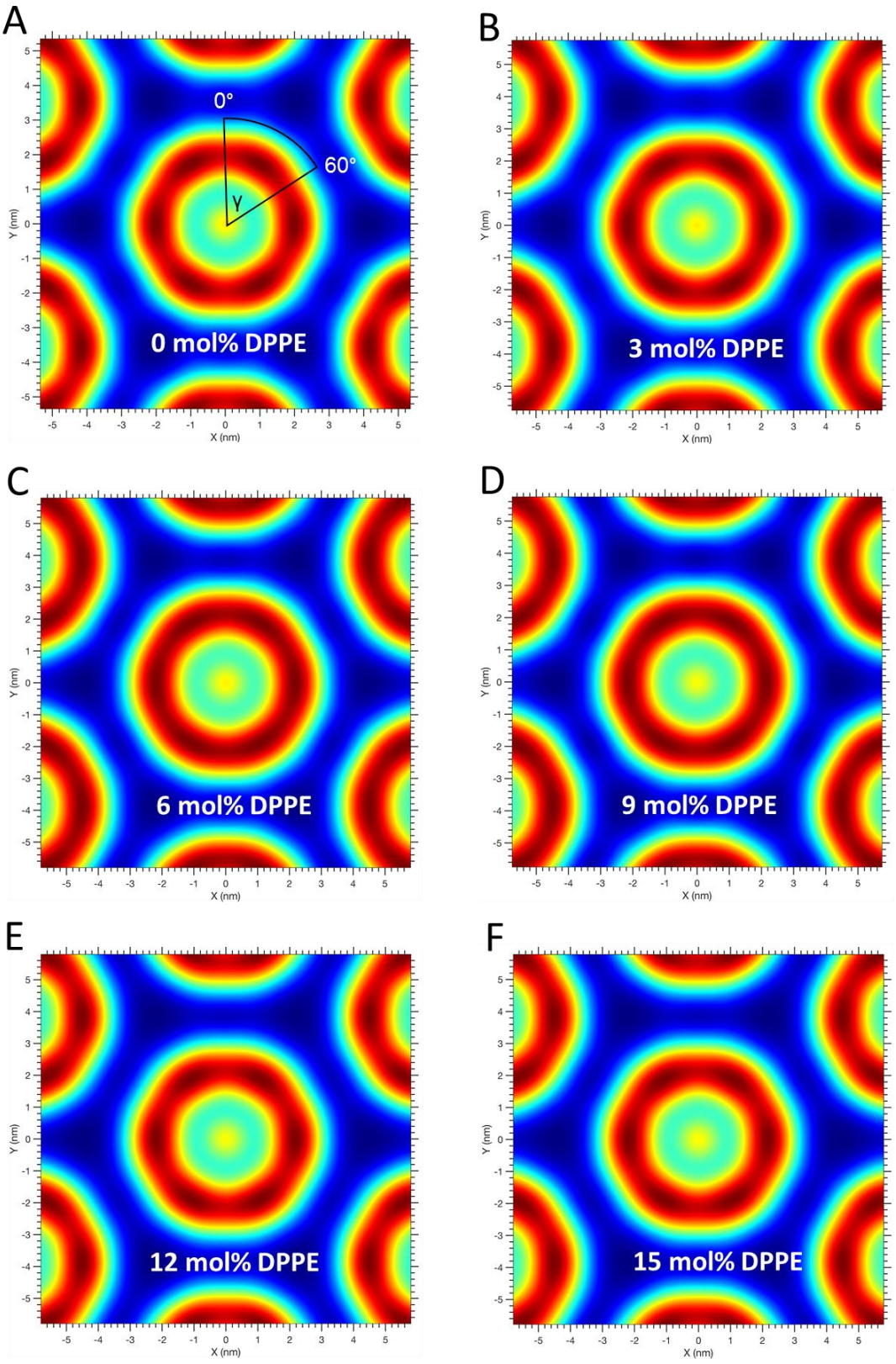

Figure B6 Electron density maps of all POPE/DPPE mixtures as function of mol% DPPE. All experimental conditions and parameters are summarized in Table B1.

Interfacial electron density fluctuation

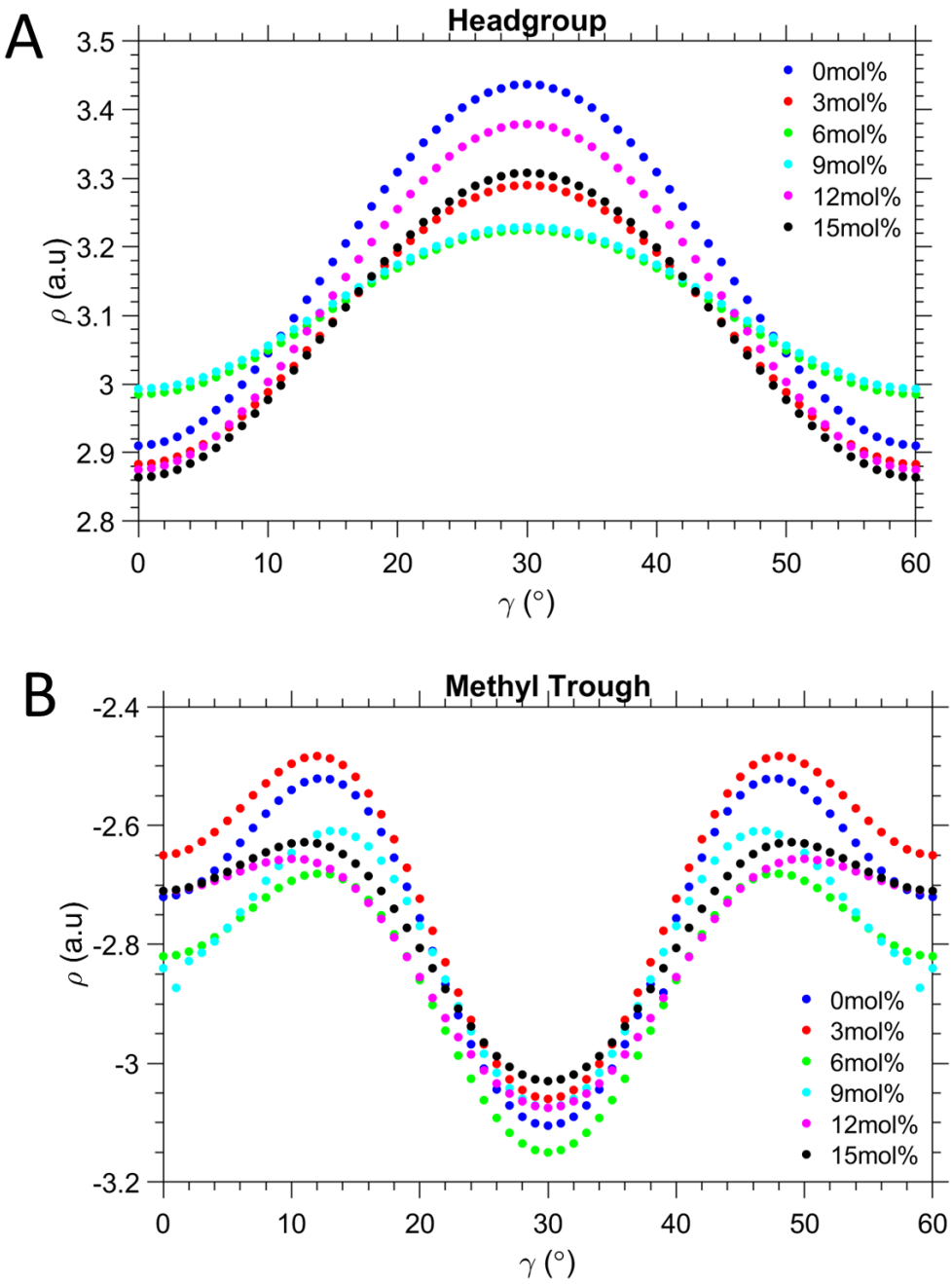

Figure B7 Electron density fluctuation along the head-group (A) and methyl trough interfaces (B). Note, these interfaces are defined in Figure 4.3A.

Radial electron density profiles

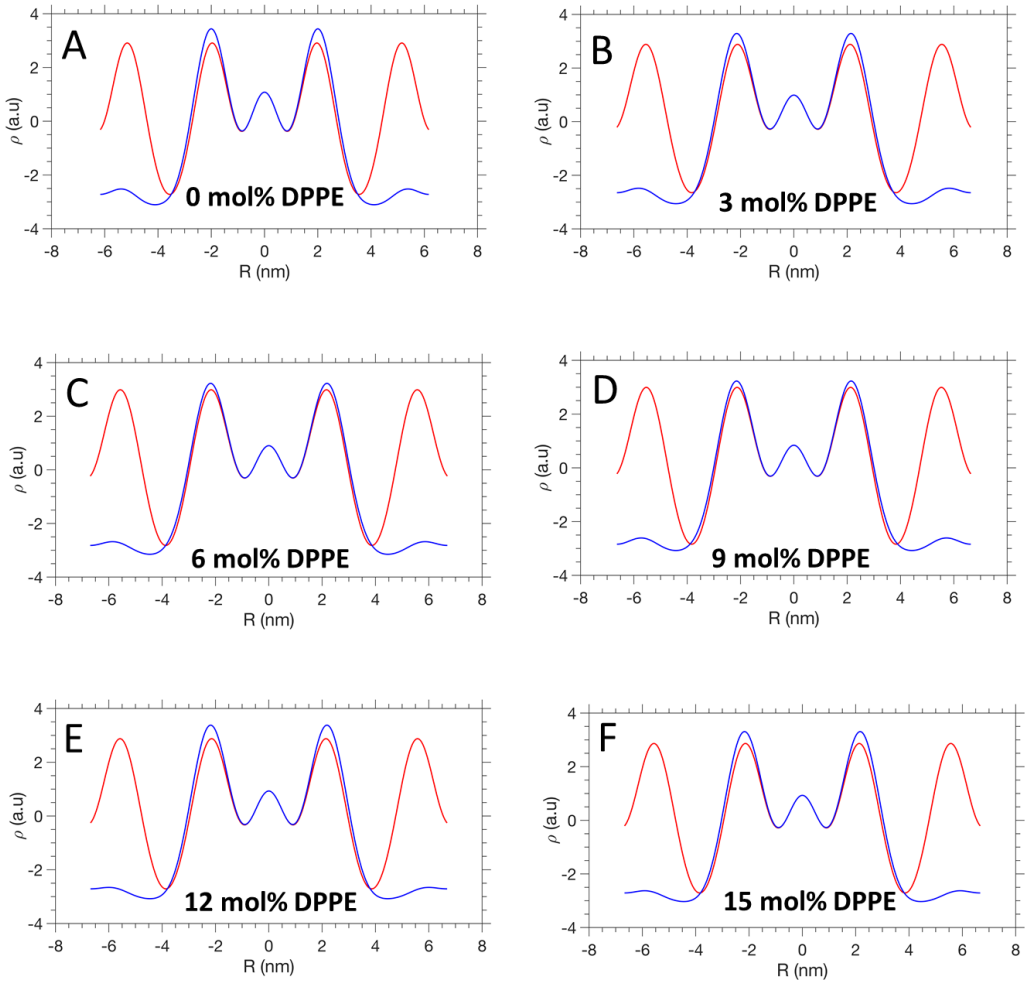

Figure B8 Radial electron density profiles with orientation of γ = 0° (red) and γ = 30° (blue). Note, γ orientations are defined in Figure B3A.

Free energy, bending energy and stretching energy per lipid

In the derivation of the free energy of lipid monolayers, Iglič and colleagues (71) assume that lipid molecules are ***anisotropic in shape*** in the inverse hexagonal phase (see molecular wedge model in Figure 1B) with respect to the axis perpendicular to the membrane plane. In their model for the lipid monolayer free energy two energy contributions are considered: the bending energy, which involves also a ***deviatoric curvature term***, D, which is an additional term to the mean curvature, H, and second, the interstitial energy, which describes the deformation energy due to stretching of the phospholipid molecule chains. Note, that the classic description of the bending energy of monolayers assumes only molecular shapes with axis rotational symmetry, which has been shown to oversimplify the description of bending energies in the inverse hexagonal phase (see also references (179, 184)). On the basis of the derived expression for the lipid monolayer free energy (equation 58 in reference (71)), the authors predict optimal geometry and physical conditions for the stability of the inverted hexagonal phase.

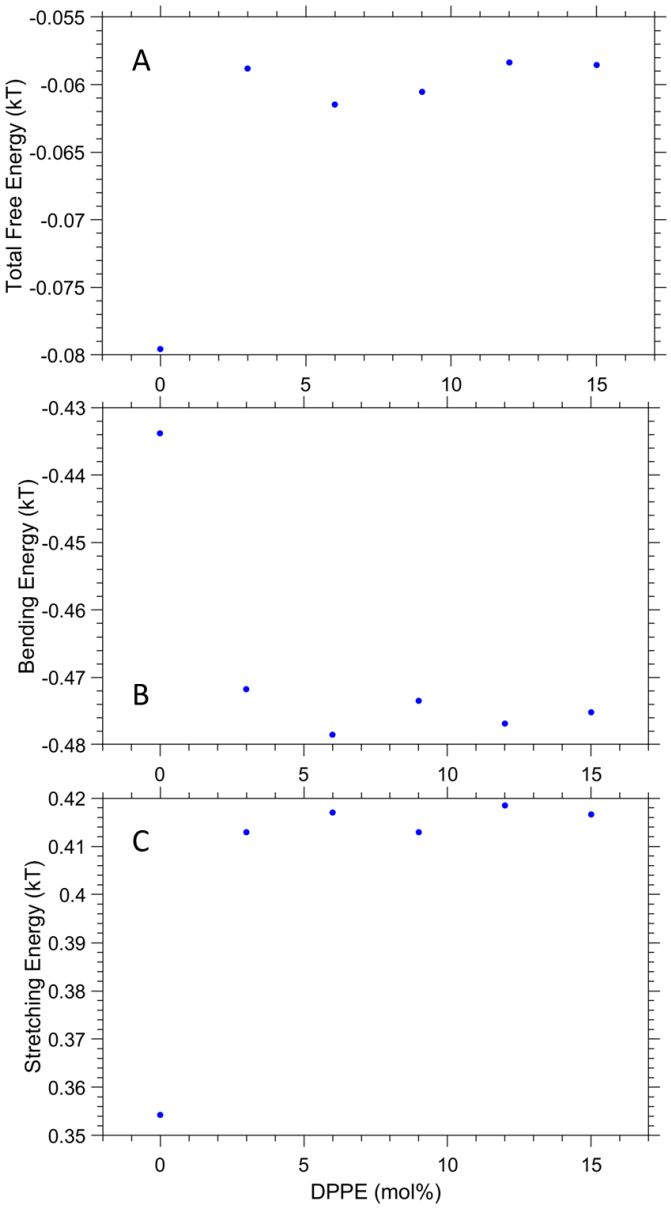

Figure B9 Free energy, bending energy and stretching energy per lipid following the theory of Aleš Iglič and colleagues (71) with the stretching modulus $\boldsymbol{\tau}$ **= 13.5 kT**, the bending modulus $\boldsymbol{K_C}$ **= 11 kT**, the mean curvature $H = -1/(R_{p\,ave}+0.5\ D_H)$ nm^{-1} with the headgroup extension $\mathbf{D_H}$ **= 1.1 nm**, the deviatoric curvature $D = |H|$, the intrinsic mean curvature $\boldsymbol{H_m}$ **= 0.1 nm^{-1}**, the intrinsic deviatoric curvature $D_m = |H_m|$, the chain length, $d_C = l_{ave}-D_H/2$ and the area per lipid at the polar/apolar interface, $A_N = A_P (R_{P\ ave}+0.5\ D_H)/R_{P\ ave}$. Best estimations of the model constants for POPE (given in bold above) were taken literature (71), all other parameters were derived from $R_{P\ ave}$ and A_P values from this study (see Table 4.1).

Appendix C: Supporting Information for Chapter 5

Table 1C Global fitting parameter results, displaying the *d*-spacing, the number of lamellae *N*, the fluctuation parameter η, the headgroup position z_H, the headgroup standard deviation σ_H, the membrane core standard deviation σ_C, the relative electron density ρ_R, the weighing factor for uncorrelated bilayer scattering N_{diff}, the scale and offset. The table refers to the fits given in Figure 5.1.

NaCl (M)	*d (nm)*	*N*	η	z_H (nm)	σ_H (nm)	σ_C (nm)	ρ_R (a.u.)	N_{diff}	Scale	Offset
0	6.513	20	0.055	1.90	0.30	0.49	1.00	1E-05	1.21E-12	3.91E-12
0.05	6.497	20	0.070	1.90	0.30	0.49	1.00	1E-05	1.26E-12	3.33E-12
0.15	6.462	20	0.071	1.90	0.30	0.58	1.00	1E-05	1.94E-12	3.37E-12
0.3	6.469	20	0.071	1.90	0.30	0.58	1.00	1E-05	1.67E-12	3.39E-12
0.6	6.520	20	0.072	1.90	0.30	0.60	1.00	1E-05	1.70E-12	3.40E-12
1	6.681	20	0.088	1.90	0.30	0.67	1.00	1E-05	1.98E-12	3.28E-12

KCl (M)	*d (nm)*	*N*	η	z_H (nm)	σ_H (nm)	σ_C (nm)	ρ_R (a.u.)	N_{diff}	Scale	Offset
0.05	6.353	20	0.058	1.90	0.3	0.59	1.00	1E-06	1.50E-12	4.62E-12
0.15	6.498	20	0.072	1.90	0.3	0.59	1.00	1E-06	1.66E-12	4.78E-12
0.3	6.512	20	0.082	1.90	0.3	0.56	1.00	1E-06	2.51E-12	3.50E-12
0.6	6.698	20	0.098	1.90	0.3	0.60	1.00	1E-06	1.78E-12	4.35E-12
1	6.816	20	0.106	1.90	0.3	0.69	1.00	1E-06	1.98E-12	3.45E-12

$MgCl_2$ (M)	*d (nm)*	*N*	η	z_H (nm)	σ_H (nm)	σ_C (nm)	ρ_R (a.u.)	N_{diff}	Scale	Offset
0.05	10.00	2	0.420	1.88	0.32	0.59	1.00	0.30	3.10E-06	7.29E-07
0.15	8.06	3	0.182	1.88	0.30	0.66	1.00	1E-05	2.47E-06	7.89E-07
0.3	6.545	20	0.075	1.90	0.30	0.68	1.00	1E-05	1.83E-12	5.40E-12
0.6	6.113	20	0.037	1.90	0.30	0.87	1.00	1E-06	7.01E-12	9.00E-12
1	5.990	20	0.039	1.90	0.30	0.85	1.00	1E-06	5.01E-12	5.01E-12

Note, fitting errors are given by the last digit displayed, e.g., d = 6.513 ± 0.005.

References

1. Vancuylenberg, G., Sadeghpour, A., Tyler, A.I.I. and Rappolt, M. Planar confined water organisation in lipid bilayer stacks of phosphatidylcholine and phosphatidylethanolamine. *Soft Matter.* 2023, **19**(27), pp.5179-5192.
2. Vancuylenberg, G., Sadeghpour, A., Tyler, A.I.I. and Rappolt, M. From angular to round: in depth interfacial analysis of binary phosphatidylethanolamine mixtures in the inverse hexagonal phase. *Soft Matter.* 2023.
3. Mittlefehldt, P.J. Writing the Waves, Sounding the Depths: Water as Metaphor and Muse. *Interdisciplinary Studies in Literature and Environment.* 2003, **10**(1), pp.137-142.
4. Witzel, M. Water in Mythology. *Daedalus.* 2015, **144**(3), pp.18-26.
5. Stanley, H.E. Mysteries of water. In: *HYDRATION PROCESSES IN BIOLOGY: THEORETICAL AND EXPERIMENTAL APPROACHES*. 1999, pp.3-31.
6. Nilsson, A. and Pettersson, L.G.M. Perspective on the structure of liquid water. *Chemical Physics.* 2011, **389**(1), pp.1-34.
7. Chaplin, M. Opinion - Do we underestimate the importance of water in cell biology? *Nature Reviews Molecular Cell Biology.* 2006, **7**(11), pp.861-866.
8. Israelachvili, J. *Intermolecular and Surface Forces.* 3rd Edition ed. London: Academic Press, 2011.
9. Rappolt, M. The Biologically Relevant Lipid Mesophases as "Seen'' by X-Rays. In: Leitmannova-Liu, A. ed. *Advances in Planar Lipid Bilayers and Liposomes*. Amsterdam: Elsevier, 2006, pp.253-283.
10. Israelachvili, J.N., Marcelja, S., Horn, R.G. and Israelachvili, J.N. Physical principles of membrane organization. *Quarterly Reviews Of Biophysics.* 1980, **13**(2), pp.121-200.
11. Storck, E.M., Özbalci, C. and Eggert, U.S. Lipid Cell Biology: A Focus on Lipids in Cell Division. *Annual Review of Biochemistry.* 2018, **87**(1), pp.839-869.
12. Joardar, A., Pattnaik, G.P. and Chakraborty, H. Mechanism of Membrane Fusion: Interplay of Lipid and Peptide. *The Journal of Membrane Biology.* 2022, **255**(2), pp.211-224.
13. Dowhan, W.B., M. Chapter 1 Functional Roles of Lipdids in Membranes *New Comprehensive Biochemistry* 2002, **36**, pp.1-35.
14. Clarke, S. The hydrophobic effect: Formation of micelles and biological membranes, 2nd edition (Tanford, Charles). *Journal Of Chemical Education.* 1981, **58**(8), p.A264.
15. Intermolecular and Surface Forces. In: Israelachvili, J.N. ed. *Intermolecular and Surface Forces (Third Edition)*. Boston: Academic Press, 2011, p.iii.
16. de Freitas, C.F., Calori, I.R., Tessaro, A.L., Caetano, W. and Hioka, N. Rapid formation of Small Unilamellar Vesicles (SUV) through low-frequency sonication: An innovative approach. *Colloids and Surfaces B: Biointerfaces.* 2019, **181**, pp.837-844.
17. Singer, S.J. and Nicholson, G.L. The fluid mosaic model of the structure of cell membranes. *Science.* 1972, **175**, pp.720-731.
18. Crowe, J.H., Crowe, L.M., Carpenter, J.F., Rudolph, A.S., Wistrom, C.A., Spargo, B.J. and Anchordoguy, T.J. Interactions of sugars with membranes. *Biochimica*

et Biophysica Acta (BBA) - Reviews on Biomembranes. 1988, **947**(2), pp.367-384.

19. Branca, C., Magazu, S., Migliardo, F. and Migliardo, P. Destructuring effect of trehalose on the tetrahedral network of water: a Raman and neutron diffraction comparison. *Physica A-Statistical Mechanics And Its Applications.* 2002, **304**(1-2), pp.314-318.
20. Coste, B., Mathur, J., Schmidt, M., Earley, T.J., Ranade, S., Petrus, M.J., Dubin, A.E. and Patapoutian, A. Piezo1 and Piezo2 Are Essential Components of Distinct Mechanically Activated Cation Channels. *Science.* 2010, **330**(6000), pp.55-60.
21. Pomorski, T.G., Nylander, T. and Cárdenas, M. Model cell membranes: Discerning lipid and protein contributions in shaping the cell. *Advances In Colloid And Interface Science.* 2014, **205**, pp.207-220.
22. Lucent, D., Vishal, V. and Pande, V.S. Protein folding under confinement: A role for solvent. *Proceedings of the National Academy of Sciences of the United States of America.* 2007, **104**(25), pp.10430-10434.
23. Aeffner, S., Reusch, T., Weinhausen, B. and Salditt, T. Energetics of stalk intermediates in membrane fusion are controlled by lipid composition. *Proc.Natl.Acad.Sci.U.S.A.* 2012, **109**(25), pp.E1609-E1618.
24. Project, L. *Boundless General Biology.* [Online]. 2024. [Accessed]. Available from: https://LibreTexts.org
25. Gorter, E. and Grendel, F. On bimolecular layers of lipoids on the chromocytes of the blood. *Proceedings of the Koninklijke Akademie Van Wetenschappen Te Amsterdam.* 1926, **29**(1/5), pp.314-317.
26. Luzzati, V., Reiss‐Husson, F., Rivas, E. and Gulik‐Krzywicki, T. *Structure and Polymorphism in Lipid-Water Systems, and their possible biological implications.* Annals of the New York Academy of Sciences. 1966, 137, pp.409-413.
27. Luzzati, V. and Husson, F. The structure of the liquid-crystalline phases of lipid-water systems. *J.Cell Biol.* 1962, **12**, pp.207-219.
28. Luzzati, V. X-ray diffraction studies of lipid-water systems. In: Chapman, D. ed. *Biological membranes.* New York: Academic Press, 1968, pp.71-123.
29. De Gennes, P.G. and Prost, J. *The physics of liquid crystals.* 2nd edition ed. Oxford: Oxford University Press, 1993.
30. Luzzati, V. Biological significance of lipid polymorphism: The cubic phases. *Current Opinion in Structural Biology.* 1997, **7**(5), pp.661-668.
31. Rappolt, M., Hodzic, A., Sartori, B., Ollivon, M. and Laggner, P. Conformational and hydrational properties during the Lβ- to Lα- and Lα- to HII-phase transition in phosphatidylethanolamine. *Chemistry and Physics of Lipids.* 2008, **154**(1), pp.46-55.
32. Perutková, S., Daniel, M., Dolinar, G., Rappolt, M., Kralj-Iglič, V. and Iglič, A. *Chapter 9 Stability of the Inverted Hexagonal Phase*. Advances in Planar Lipid Bilayers and Liposomes. 2009, 9, pp.237-278.
33. Schamberger, B., Ziege, R., Anselme, K., Ben Amar, M., Bykowski, M., Castro, A.P.G., Cipitria, A., Coles, R.A., Dimova, R., Eder, M., Ehrig, S., Escudero, L.M., Evans, M.E., Fernandes, P.R., Fratzl, P., Geris, L., Gierlinger, N., Hannezo, E., Iglič, A., Kirkensgaard, J.J.K., Kollmannsberger, P., Kowalewska, Ł., Kurniawan,

N.A., Papantoniou, I., Pieuchot, L., Pires, T.H.V., Renner, L.D., Sageman-Furnas, A.O., Schröder-Turk, G.E., Sengupta, A., Sharma, V.R., Tagua, A., Tomba, C., Trepat, X., Waters, S.L., Yeo, E.F., Roschger, A., Bidan, C.M. and Dunlop, J.W.C. Curvature in Biological Systems: Its Quantification, Emergence, and Implications across the Scales. *Adv Mater.* 2023, **35**(13), p.e2206110.

34. Mares, T., Daniel, M., Perutkova, S., Perne, A., Dolinar, G., Iglic, A., Rappolt, M. and Kralj-Iglic, V. Role of phospholipid asymmetry in stability of inverted hexagonal mesoscopic phases. *J.Phys.Chem.B.* 2008, **112**, pp.16575-16584.
35. Doktorova, M., LeVine, M.V., Khelashvili, G. and Weinstein, H. A New Computational Method for Membrane Compressibility: Bilayer Mechanical Thickness Revisited. *Biophysical Journal.* 2019, **116**(3), pp.487-502.
36. Petrache, H.I., Tristram-Nagle, S., Gawrisch, K., Harries, D., Parsegian, V.A. and Nagle, J.F. Structure and Fluctuations of Charged Phosphatidylserine Bilayers in the Absence of Salt. *Biophysical Journal.* 2004, **86**(3), pp.1574-1586.
37. Nagle, J.F. and Tristram-Nagle, S. Structure of lipid bilayers. *Biochimica Et Biophysica Acta-Reviews on Biomembranes.* 2000, **1469**(3), pp.159-195.
38. Seddon, J.M., Cevc, G., Kaye, R.D. and Marsh, D. X-ray diffraction study of the polymorphism of hydrated diacyl- and dialkylphosphatidylethanolamines. *Biochemistry.* 1984, **23**(12), pp.2634-2644.
39. Harper, P.E., Mannock, D.A., Lewis, R.N., McElhaney, R.N. and Gruner, S.M. X-ray diffraction structures of some phosphatidylethanolamine lamellar and inverted hexagonal phases. *Biophysical Journal.* 2001, **81**(5), pp.2693-2706.
40. Rappolt, M., Laggner, P. and Pabst, G. Structure and elasticity of phospholipid bilayers in the La phase: A comparison of phosphatidylcholine and phosphatidylethanolamine membranes. In: Pandalai, S.G. ed. *Recent Research Developments in Biophysics*. Trivandrum: Transworld Research Network, 2004, pp.365-394.
41. Cockcroft, S. Mammalian lipids: structure, synthesis and function. *Essays in Biochemistry.* 2021, **65**(5), pp.813-845.
42. Panizza, P., Archambault, P. and Roux, D. Effects of shear on the smectic A-phase of thermotropic liquid crystals. *Journal de Physique II.* 1995, **5**(2), pp.303-311.
43. McIntosh, T.J. and Simon, S.A. Area per molecule and distribution of water in fully hydrated dilauroylphosphatidylethanolamine bilayers. *Biochemistry.* 1986, **25**(17), pp.4948-4952.
44. Nagle, J.F., Zhang, R., Tristram-Nagle, S., Sun, W., Petrache, H.I. and Suter, R.M. X-ray structure determination of fully hydrated L alpha phase dipalmitoylphosphatidylcholine bilayers. *Biophysical Journal.* 1996, **70**(3), pp.1419-1431.
45. McIntosh, T.J. and Simon, S.A. Adhesion between phophatidylethanolmaine bilayers. *Langmuir.* 1996, **12**, pp.1622-1630.
46. Helfrich, W. and Servuss, R.M. Undulations, steric interaction and cohesion of fluid membranes. *Il Nuovo Cimento D.* 1984, **3**(1), pp.137-151.
47. Pozo-Navas, B., Raghunathan, V.A., Katsaras, J., Rappolt, M., Lohner, K. and Pabst, G. Discontinuous Unbinding of Lipid Multibilayers. *Physical Review Letters.* 2003, **91**(2).

48. Disalvo, E.A., Lairion, F., Martini, F., Tymczyszyn, E., Frías, M., Almaleck, H. and Gordillo, G.J. Structural and functional properties of hydration and confined water in membrane interfaces. *Biochimica et Biophysica Acta (BBA) - Biomembranes.* 2008, **1778**(12), pp.2655-2670.
49. Nickels, J.D., Smith, J.C. and Cheng, X.L. Lateral organization, bilayer asymmetry, and inter-leaflet coupling of biological membranes. *Chemistry and Physics of Lipids.* 2015, **192**, pp.87-99.
50. Kittel, C. *Introduction to Solid State Physics.* 7th ed. New York: John Wiley & Sons, Inc., 1996.
51. Pabst, G. Global properties of biomimetic membranes: perspectives on molecular features. *Biophys.Rev.Letters.* 2006, **1**, pp.57-84.
52. Warren, B.E. *X-ray Diffraction.* Reading: Addison-Wesley, 1969.
53. Rappolt, M. and Pabst, G. Flexibility and structure of fluid bilayer interfaces. In: Nag, K. ed. *Structure and dynamics of membranous interfaces*. Hoboken: John Wiley & Sons, 2008, pp.45-81.
54. Amenitsch, H., Rappolt, M., Teixeira, C.V., Majerowicz, M. and Laggner, P. In Situ Sensing of Salinity in Oriented Lipid Multilayers by Surface X-ray Scattering. *Langmuir.* 2004, **20**(11), pp.4621-4628.
55. Pauw, B.R., Smith, A.J., Snow, T., Terrill, N.J. and Thunemann, A.F. The modular small-angle X-ray scattering data correction sequence. *Journal of Applied Crystallography.* 2017, **50**(6), pp.1800-1811.
56. Heftberger, P., Kollmitzer, B., Heberle, F.A., Pan, J., Rappolt, M., Amenitsch, H., Kučerka, N., Katsaras, J. and Pabst, G. Global small-angle X-ray scattering data analysis for multilamellar vesicles: the evolution of the scattering density profile model. *Journal of Applied Crystallography.* 2014, **47**(1), pp.173-180.
57. Rappolt, M. Bilayer thickness estimations with "poor" diffraction data. *Journal of Applied Physics.* 2010, **107**(8).
58. Rappolt, M. 50 Years of structural lipid bilayer modelling. In: Iglic, A. et al. eds. *Advances in Biomembranes and Lipid Self-Assembly*. Elsevier B.V., 2019, pp.1-21.
59. Li, N.Y.D., Perutková, Š., Iglič, A. and Rappolt, M. My first electron density map: A beginner's guide to small angle X-ray diffraction. *Elektrotehniski Vestnik/Electrotechnical Review.* 2017, **84**(3), pp.69-75.
60. Levine, Y.K. X-ray diffraction studies of membranes. *Progr.Surf.Sci.* 1973, **3**, pp.279-352.
61. Luzzati, V., Mariani, P. and Delacroix, H. X-ray Crystallography at Macromolecular Resolution: A Solution of the Phase Problem. *Makromol.Chem.Macromol.Symp.* 1988, **15**, pp.1-17.
62. McIntosh, T.J. and Simon, S.A. Hydration force and bilayer deformation: a reevaluation. *Biophys.J.* 1986, **25**, pp.4058-4066.
63. Turner, D.C. and Gruner, S.M. X-ray diffraction reconstruction of the inverted hexagonal (HII) phase in lipid-water systems. *Biochemistry.* 1992, **31**, pp.1340-1355.
64. Hosemann, R. and Bagchi, S.N. *Direct analysis of diffraction by matter.* Amsterdam: North-Holland Publ. Co., 1962.

65. Blaurock, A.E. Evidence of bilayer structure and of membrane interactions from X-ray diffraction analysis. *Biochimica et Biophysica Acta (BBA) - Reviews on Biomembranes.* 1982, **650**(4), pp.167-207.
66. Caillé, A. Remarques sur la diffusion des rayons X dans les smectiques A. *C.R.Acad.Sc.Paris B.* 1972, **274**, pp.891-893.
67. Zhang, R., Tristram-Nagle, S., Sun, W., Headrick, R.L., Irving, T.C., Suter, R.M. and Nagle, J.F. Small-angle x-ray scattering from lipid bilayers is well described by modified Caillé theory but not by paracrystalline theory. *Biophys.J.* 1996, **70**, pp.349-357.
68. Zhang, R., Suter, R.M. and Nagle, J.F. Theory of the structure factor of lipid bilayers. *Physical Review E.* 1994, **50**(6), pp.5047-5060.
69. Petrache, H.I., Tristram-Nagle, S. and Nagle, J.F. Fluid phase structure of EPC and DMPC bilayers. *Chem.Phys.Lipids.* 1998, **95**(1), pp.83-94.
70. Pabst, G., Rappolt, M., Amenitsch, H. and Laggner, P. Structural information from multilamellar liposomes at full hydration: Full q-range fitting with high quality X-ray data. *Physical Review E - Statistical Physics, Plasmas, Fluids, and Related Interdisciplinary Topics.* 2000, **62**(3 B), pp.4000-4009.
71. Perutkova, S., Daniel, M., Dolinar, G., Rappolt, M., Kralj-Iglic, V. and Iglic, A. Stabilty of the inverted hexagonal phase. In: Leitmannova-Liu, A. and Tien, H.T. eds. *Advances in Planar Lipid Bilayers and Liposomes*. Burlington: Elsvier, Academic Press, 2009, pp.238-278.
72. Sackmann, E. Biological membranes architecture and function. In: Lipowsky, R. and Sackmann, E. eds. *Structure and dynamics of membranes*. Amsterdam: Elsevier, 1995, pp.1-63.
73. Zimmerberg, J. and Kozlov, M.M. How proteins produce cellular membrane curvature. *Nature Rev.* 2006, **7**, pp.9-19.
74. Lipowsky, R. and Sackmann, E. *Structure and dynamics of membranes. From cells to vesicles.* Amsterdam: Elsevier, 1995.
75. McIntosh, T.J. Differences in hydrocarbon chain tilt between hydrated phosphatidylethanolamine and phosphatidylcholine bilayers. A molecular packing model. *Biophysical Journal.* 1980, **29**(2), pp.237-245.
76. Papahadjopoulos, D. and Miller, N. Phospholipid model membranes. I. Structural characteristics of hydrated liquid crystals. *Biochimica et Biophysica Acta (BBA) - Biomembranes.* 1967, **135**(4), pp.624-638.
77. Hodzic, A., Zoumpoulakis, P., Pabst, G., Mavromoustakos, T. and Rappolt, M. Losartan's affinity to fluid bilayers modulates lipid-cholesterol interactions. *Physical Chemistry Chemical Physics.* 2012, **14**(14), pp.4780-4788.
78. Walde, P., Cosentino, K., Engel, H. and Stano, P. Giant Vesicles: Preparations and Applications. *Chembiochem.* 2010, **11**(7), pp.848-865.
79. Chen, C., Zhu, S., Huang, T., Wang, S. and Yan, X. Analytical techniques for single-liposome characterization. *Analytical Methods.* 2013, **5**(9), pp.2150-2157.
80. Sciolla, F., Truzzolillo, D., Chauveau, E., Trabalzini, S., Di Marzio, L., Carafa, M., Marianecci, C., Sarra, A., Bordi, F. and Sennato, S. Influence of drug/lipid interaction on the entrapment efficiency of isoniazid in liposomes for antitubercular therapy: a multi-faced investigation. *Colloids and Surfaces B: Biointerfaces.* 2021, **208**, p.112054.

81. Xu, Z., Seddon, J.M., Beales, P.A., Rappolt, M. and Tyler, A.I.I. Breaking Isolation to Form New Networks: pH-Triggered Changes in Connectivity inside Lipid Nanoparticles. *Journal Of The American Chemical Society.* 2021, **143**(40), pp.16556-16565.
82. Schwille, P., Spatz, J., Landfester, K., Bodenschatz, E., Herminghaus, S., Sourjik, V., Erb, T.J., Bastiaens, P., Lipowsky, R., Hyman, A., Dabrock, P., Baret, J.-C., Vidakovic-Koch, T., Bieling, P., Dimova, R., Mutschler, H., Robinson, T., Tang, T.Y.D., Wegner, S. and Sundmacher, K. MaxSynBio: Avenues Towards Creating Cells from the Bottom Up. *Angewandte Chemie International Edition.* 2018, **57**(41), pp.13382-13392.
83. Seneviratne, R., Coates, G., Xu, Z., Cornell, C.E., Thompson, R.F., Sadeghpour, A., Maskell, D.P., Jeuken, L.J.C., Rappolt, M. and Beales, P.A. High Resolution Membrane Structures within Hybrid Lipid-Polymer Vesicles Revealed by Combining X-Ray Scattering and Electron Microscopy. *Small.* 2023, **n/a**(n/a), p.2206267.
84. Noireaux, V. and Libchaber, A. A vesicle bioreactor as a step toward an artificial cell assembly. *Proceedings Of The National Academy Of Sciences Of The United States Of America.* 2004, **101**(51), pp.17669-17674.
85. Jendrasiak, G.L. The hydration of phospholipids and its biological significance. *The Journal of Nutritional Biochemistry.* 1996, **7**(11), pp.599-609.
86. Shearman, G.C., Ces, O., Templer, R.H. and Seddon, J.M. Inverse lyotropic phases of lipids and membrane curvature. *J.Phys.Condens.Matter.* 2006, **18**, pp.S1105-S1124.
87. Tristram-Nagle, S. Use of X-ray and neutron scattering methods with volume measurements to determine lipid bilayer structure and number of water molecules/lipid. In: Disalvo, E.A. ed. *Membrane Hydration*. Springer, 2015, pp.17-43.
88. Rappolt, M. and Rapp, G. Simultaneous small- and wide-angle x-ray diffraction during the main transition of dimyristoylphosphatidylethanolamine. *Ber.Bunsenges.Phys.Chem.* 1996, **100**(7), pp.1153-1162.
89. Lopez, C.F., Nielsen, S.O., Klein, M.L. and Moore, P.B. Hydrogen Bonding Structure and Dynamics of Water at the Dimyristoylphosphatidylcholine Lipid Bilayer Surface from a Molecular Dynamics Simulation. *The Journal of Physical Chemistry B.* 2004, **108**(21), pp.6603-6610.
90. Alper, H.E., Bassolino‐Klimas, D. and Stouch, T.R. The limiting behavior of water hydrating a phospholipid monolayer: A computer simulation study. *The Journal of Chemical Physics.* 1993, **99**(7), pp.5547-5559.
91. Lee, E., Kundu, A., Jeon, J. and Cho, M. Water hydrogen-bonding structure and dynamics near lipid multibilayer surface: Molecular dynamics simulation study with direct experimental comparison. *The Journal of Chemical Physics.* 2019, **151**(11), p.114705.
92. Martelli, F., Ko, H.-Y., Borallo, C.C. and Franzese, G. Structural properties of water confined by phospholipid membranes. *Frontiers of Physics.* 2017, **13**(1), p.136801.
93. Pasenkiewicz-Gierula, M., Takaoka, Y., Miyagawa, H., Kitamura, K. and Kusumi, A. Hydrogen Bonding of Water to Phosphatidylcholine in the Membrane As Studied by a Molecular Dynamics Simulation: Location,

Geometry, and Lipid−Lipid Bridging via Hydrogen-Bonded Water. *The Journal of Physical Chemistry A.* 1997, **101**(20), pp.3677-3691.

94. McIntosh, T.J. Hydration properties of lamellar and non-lamellar phases of phosphatidylcholine and phosphatidylethanolamine. *Chem.Phys.Lipids.* 1996, **81**(2), pp.117-131.
95. Tanford, C. The hydrophobic effect and the organization of living matter. *Science.* 1978, **200**, pp.1012-1018.
96. Parsegian, V.A. and Rand, R.P. Chapter 13 - Interaction in Membrane Assemblies. In: Lipowsky, R. and Sackmann, E. eds. *Handbook of Biological Physics*. North-Holland, 1995, pp.643-690.
97. Wiener, M.C., Suter, R.M. and Nagle, J.F. Structure of the fully hydrated gel phase of dipalmitoylphosphatidylcholine. *Biophys.J.* 1989, **55**, pp.315-325.
98. Heftberger, P., Kollmitzer, B., Heberle, F.A., Pan, J.J., Rappolt, M., Amenitsch, H., Kucerka, N., Katsaras, J. and Pabst, G. Global small-angle X-ray scattering data analysis for multilamellar vesicles: the evolution of the scattering density profile model. *Journal of Applied Crystallography.* 2014, **47**, pp.173-180.
99. Salvati Manni, L., Assenza, S., Duss, M., Vallooran, J.J., Juranyi, F., Jurt, S., Zerbe, O., Landau, E.M. and Mezzenga, R. Soft biomimetic nanoconfinement promotes amorphous water over ice. *Nature Nanotechnology.* 2019, **14**(6), pp.609-615.
100. Frewein, M.P.K., Doktorova, M., Heberle, F.A., Scott, H.L., Semeraro, E.F., Porcar, L. and Pabst, G. Structure and interdigitation of chain-asymmetric phosphatidylcholines and milk sphingomyelin in the fluid phase. *Symmetry.* 2021, **13**(8).
101. Kasson, P.M., Lindahl, E. and Pande, V.S. Water ordering at membrane interfaces controls fusion dynamics. *Journal Of The American Chemical Society.* 2011, **133**(11), pp.3812-3815.
102. McIntosh, T.J. and Simon, S.A. Hydration and steric pressures between phospholipid bilayers. *Annu.Rev.Biophys.Biomol.Struct.* 1994, **23**, pp.27-51.
103. Simon, S.A. and McIntosh, T.J. Depth of water penetration into lipid bilayers. *Methods Enzymol.* 1986, **127**, pp.511-521.
104. Wurpel, G.W.H. and Müller, M. Water confined by lipid bilayers: A multiplex CARS study. *Chemical Physics Letters.* 2006, **425**(4), pp.336-341.
105. Arsov, Z., Rappolt, M. and Grdadolnik, J. Weakened hydrogen bonds in water confined between lipid bilayers: The existence of a long-range attractive hydration force. *ChemPhysChem.* 2009, **10**(9-10), pp.1438-1441.
106. Zhang, R., Cross, T.A., Peng, X. and Fu, R. Surprising Rigidity of Functionally Important Water Molecules Buried in the Lipid Headgroup Region. *Journal of the American Chemical Society.* 2022, **144**(17), pp.7881-7888.
107. Pérez, H.A., Alarcón, L.M., Verde, A.R., Appignanesi, G.A., Giménez, R.E., Disalvo, E.A. and Frías, M.A. Effect of cholesterol on the hydration properties of ester and ether lipid membrane interphases. *Biochimica et Biophysica Acta (BBA) - Biomembranes.* 2021, **1863**(1), p.183489.
108. Heftberger, P., Kollmitzer, B., Rieder, Alexander A., Amenitsch, H. and Pabst, G. In Situ Determination of Structure and Fluctuations of Coexisting Fluid Membrane Domains. *Biophysical Journal.* 2015, **108**(4), pp.854-862.

109. Putzel, G.G., Uline, M.J., Szleifer, I. and Schick, M. Interleaflet Coupling and Domain Registry in Phase-Separated Lipid Bilayers. *Biophysical Journal.* 2011, **100**(4), pp.996-1004.
110. Kratky, O., Leopold, H. and Stabinger, H. [5] The determination of the partial specific volume of proteins by the mechanical oscillator technique. In: *Methods in Enzymology*. Academic Press, 1973, pp.98-110.
111. Hodzic, A., Rappolt, M., Amenitsch, H., Laggner, P. and Pabst, G. Differential modulation of membrane structure and fluctuations by plant sterols and cholesterol. *Biophysical Journal.* 2008, **94**(10), pp.3935-3944.
112. Koynova, R. and Hinz, H.-J. Metastable behaviour of saturated phosphatidylethanolamines: a densitometric study. *Chemistry and Physics of Lipids.* 1990, **54**(1), pp.67-72.
113. Koch, M.H.J., Vachette, P. and Svergun, D.I. Small-angle scattering: a view on the properties, structures and structural changes of biological macromolecules in solution. *Quarterly Reviews Of Biophysics.* 2003, **36**(2), pp.147-227.
114. Torbet, J. and Wilkins, M.H.F. X-ray diffraction studies of lecithin bilayers. *J.Theor.Biol.* 1976, **62**, pp.447-458.
115. Gerstein, M. and Chothia, C. Packing at the protein-water interface. *Proc Natl Acad Sci U S A.* 1996, **93**(19), pp.10167-10172.
116. Silvius, D.J.R. *Thermotropic Phase Transitions of Pure Lipids in Model Membranes and Their Modifications by Membrane Proteins.* New York: John Wiley & Sons, Inc, 1982.
117. Caffrey, M. and Hogan, J. LIPIDAT: a database of lipid phase transition temperatures and enthalpy changes. DMPC data subset analysis. *Chem Phys Lipids.* 1992, **61**(1), pp.1-109.
118. Rappolt, M. and Rapp, G. Simultaneous Small- And Wide-Angle X-Ray Diffraction during the Transition of Dimyristoylphosphatidylethanolamine. *Berichte der Bunsengesellschaft/Physical Chemistry Chemical Physics.* 1996, **100**(7), pp.1153-1162.
119. White, S.H., Jacobs, R.E. and King, G.I. PARTIAL SPECIFIC VOLUMES OF LIPID AND WATER IN MIXTURES OF EGG LECITHIN AND WATER. *Biophysical Journal.* 1987, **52**(4), pp.663-665.
120. Tristram-Nagle, S., Petrache, H.I. and Nagle, J.F. Structure and Interactions of Fully Hydrated Dioleoylphosphatidylcholine Bilayers. *Biophysical Journal.* 1998, **75**(2), pp.917-925.
121. Nagle, J.F. and Wilkinson, D.A. Lecithin bilayers. Density measurements and molecular interactions. *Biophys.J.* 1978, **23**, pp.159-175.
122. Pechhold, W. Molekülbewegung in Polymeren. *Kolloid-Zeitschrift und Zeitschrift für Polymere.* 1968, **228**(1), pp.1-38.
123. Seelig, A. and Seelig, J. The dynamic structure of fatty acyl chains in a phospholipid bilayer measured by deuterium magnetic resonance. *Biochemistry.* 1974, **13**(23), pp.4839-4845.
124. Ge, M. and Freed, J.H. Hydration, Structure, and Molecular Interactions in the Headgroup Region of Dioleoylphosphatidylcholine Bilayers: An Electron Spin Resonance Study. *Biophysical Journal.* 2003, **85**(6), pp.4023-4040.

125. Rand, R.P. and Parsegian, V.A. Hydration forces between phospholipid bilayers. *Biochim.Biophys.Acta.* 1989, **988**, pp.351-376.
126. Rawicz, W., Olbrich, K.C., McIntosh, T., Needham, D. and Evans, E. Effect of chain length and unsaturation on elasticity of lipid bilayers. *Biophys.J.* 2000, **79**(1), pp.328-339.
127. Fosnaric, M., Iglic, A. and May, S. Influence of rigid inclusions on the bending elasticity of a lipid membrane. *Phys Rev E Stat Nonlin Soft Matter Phys.* 2006, **74**(5 Pt 1), p.051503.
128. Chu, N., Kucerka, N., Liu, Y., Tristram-Nagle, S. and Nagle, J.F. Anomalous swelling of lipid bilayer stacks is caused by softening of the bending modulus. *Phys.Rev.E.* 2005, **71**, pp.041904-041901-041904-041908.
129. Pabst, G., Katsaras, J., Raghunathan, V.A. and Rappolt, M. Structure and interactions in the anomalous swelling regime of phospholipid bilayers. *Langmuir.* 2003, **19**(5), pp.1716-1722.
130. Nagle, J.F. Experimentally determined tilt and bending moduli of single-component lipid bilayers. *Chemistry and Physics of Lipids.* 2017, **205**, pp.18-24.
131. Mutz, M. and Helfrich, W. Bending rigidities of some biological model membranes as obtained from the Fourier analysis of contour sections. *J. Phys. France.* 1990, **51**(10), pp.991-1001.
132. Chng, C.-P., Sadovsky, Y., Hsia, K.J. and Huang, C. Curvature-regulated lipid membrane softening of nano-vesicles. *Extreme Mechanics Letters.* 2021, **43**, p.101174.
133. McIntosh, T.J. Short-range interactions between lipid bilayers measured by X-ray diffraction. *Curr.Opin.Struct.Biol.* 2000, **10**(4), pp.481-485.
134. Petrache, H.I., Gouliaev, N., Tristram-Nagle, S., Zhang, R.T., Suter, R.M. and Nagle, J.F. Interbilayer interactions from high-resolution x-ray scattering. *Phys.Rev.E.* 1998, **57**(6), pp.7014-7024.
135. Israelachvili, J.N. Chapter 13 - Van der Waals Forces between Particles and Surfaces. In: Israelachvili, J.N. ed. *Intermolecular and Surface Forces (Third Edition)*. Boston: Academic Press, 2011, pp.253-289.
136. Gongadze, E., Mesarec, L., Kralj-Iglič, V. and Iglič, A. Asymmetric finite size of ions and orientational ordering of water in electric double layer theory within lattice model. *Mini-Reviews in Medicinal Chemistry.* 2018, **18**(18), pp.1559-1566.
137. Gongadze, E., Velikonja, A., Perutkova, Š., Kramar, P., Maček-Lebar, A., Kralj-Iglič, V. and Iglič, A. Ions and water molecules in an electrolyte solution in contact with charged and dipolar surfaces. *Electrochimica Acta.* 2014, **126**, pp.42-60.
138. Li, N.Y.D., Moore, D.J., Thompson, M.A., Welfare, E. and Rappolt, M. Influence of humectants on the thermotropic behaviour and nanostructure of fully hydrated lecithin bilayers. *Chemistry and Physics of Lipids.* 2022, **243**.
139. Iglič, A., Gongadze, E. and Kralj-Iglič, V. Differential Capacitance of Electric Double Layer - Influence of Asymmetric Size of Ions, Thickness of Stern Layer and Orientational Ordering of Water Dipoles. *Acta Chim Slov.* 2019, **66**(3), pp.534-541.

140. McIntosh, T.J., Magid, A.D. and Simon, S.A. Repulsive interactions between uncharged bilayers. Hydration and fluctuation pressures for monoglycerides. *Biophysical Journal.* 1989, **55**(5), pp.897-904.
141. Blesso, C.N. Egg phospholipids and cardiovascular health. *Nutrients.* 2015, **7**(4), pp.2731-2747.
142. Pabst, G., Amenitsch, H., Kharakoz, D.P., Laggner, P. and Rappolt, M. Structure and fluctuations of phosphatidylcholines in the vicinity of the main phase transition. *Physical Review E - Statistical Physics, Plasmas, Fluids, and Related Interdisciplinary Topics.* 2004, **70**(2), p.9.
143. Wilkinson, D.A. and Nagle, J.F. Dilatometry and calorimetry of saturated phosphatidylethanolamine dispersions. *Biochemistry.* 1981, **20**(1), pp.187-192.
144. Kucerka, N., Kiselev, M.A. and Balgavy, P. Determination of bilayer thickness and lipid surface area in unilamellar dimyristoylphosphatidylcholine vesicles from small-angle neutron scattering curves: a comparison of evaluation methods. *Eur.Biophys.J.* 2004, **33**(4), pp.328-334.
145. Kucerka, N., Liu, Y., Chu, N., Petrache, H.I., Tristram-Nagle, S. and Nagle, J.F. Structure of fully hydrated fluid phase DMPC and DLPC lipid bilayers using X-ray scattering from oriented multilamellar arrays and from unilamellar vesicles. *Biophys.J.* 2005, **88**, pp.2626-2637.
146. Kucerka, N., Nagle, J.F., Sachs, J.N., Feller, S.E., Pencer, J., Jackson, A. and Katsaras, J. Lipid bilayer structure determined by the simultaneous analysis of neutron and x-ray scattering data. *Biophys.J.* 2008, **95**, pp.2356-2367.
147. Kucerka, N., Tristram-Nagle, S. and Nagle, J.F. Structure of fully hydrated fluid phase lipid bilayers with monounsaturated chains. *J.Membrane Biol.* 2005, **208**, pp.193-202.
148. Seelig, J., Gally, H.-U. and Wohlgemuth, R. Orientation and flexibility of the choline head group in phosphatidylcholine bilayers. *Biochimica et Biophysica Acta (BBA) - Biomembranes.* 1977, **467**(2), pp.109-119.
149. Ferreira, T.M., Coreta-Gomes, F., Samuli Ollila, O.H., Moreno, M.J., Vaz, W.L.C. and Topgaard, D. Cholesterol and POPC segmental order parameters in lipid membranes: Solid state 1H-13C NMR and MD simulation studies. *Physical Chemistry Chemical Physics.* 2013, **15**(6), pp.1976-1989.
150. Lebar, A.M., Velikonja, A., Kramar, P. and Iglič, A. Internal configuration and electric potential in planar negatively charged lipid head group region in contact with ionic solution. *Bioelectrochemistry.* 2016, **111**, pp.49-56.
151. Tu, K., Tobias, D.J., Blasie, J.K. and Klein, M.L. Molecular dynamics investigation of the structure of a fully hydrated gel-phase dipalmitoylphosphatidylcholine bilayer. *Biophys J.* 1996, **70**(2), pp.595-608.
152. Herzberg, G. Molecular Spectra and Molecular Structure. I. Spectra of Diatomic Molecules. *American Journal of Physics.* 1951, **19**(6), pp.390-391.
153. Buck, I., Callomon, J.H., Hellwege, K.H., Starck, B., Hirota, E., Hellwege, A.M., Kuchitsu, K., Lafferty, W.J., Maki, A.G. and Pote, C.S. *Structure Data of Free Polyatomic Molecules / Strukturdaten freier mehratomiger Molekeln.* Springer Berlin Heidelberg, 1976.
154. Greenwood, N.N. and Earnshaw, A. *Chemistry of the Elements.* Elsevier, 1997.

155. Yaghmur, A., Paasonen, L., Yliperttula, M., Urtti, A. and Rappolt, M. Structural elucidation of light activated vesicles. *Journal Of Physical Chemistry Letters.* 2010, **1**(6), pp.962-966.
156. Rappolt, M., Hickel, A., Bringezu, F. and Lohner, K. Mechanism of the lamellar/inverse hexagonal phase transition examined by high resolution x-ray diffraction. *Biophysical Journal.* 2003, **84**(5), pp.3111-3122.
157. Rappolt, M. Chapter Two - Formation of Curved Membranes and Membrane Fusion Processes Studied by Synchrotron X-ray-Scattering Techniques. In: Aleš, I. and Julia, G. eds. *Advances in Planar Lipid Bilayers and Liposomes*. Academic Press, 2013, pp.29-54.
158. Sánchez-Lavega, A., García-Muñoz, A., del Río-Gaztelurrutia, T., Pérez-Hoyos, S., Sanz-Requena, J.F., Hueso, R., Guerlet, S. and Peralta, J. Multilayer hazes over Saturn's hexagon from Cassini ISS limb images. *Nature Communications.* 2020, **11**(1).
159. Godfrey, D.A. A hexagonal feature around Saturn's north pole. *Icarus.* 1988, **76**(2), pp.335-356.
160. Hales, T.C. The honeycomb conjecture. *Discrete and Computational Geometry.* 2001, **25**(1), pp.1-22.
161. Almsherqi, Z.A., Kohlwein, S.D. and Deng, Y. Cubic membranes: A legend beyond the Flatland* of cell membrane organization. *Journal of Cell Biology.* 2006, **173**(6), pp.839-844.
162. Deng, Y. and Angelova, A. Coronavirus-Induced Host Cubic Membranes and Lipid-Related Antiviral Therapies: A Focus on Bioactive Plasmalogens. *Frontiers in Cell and Developmental Biology.* 2021, **9**.
163. Rappolt, M. *Formation of Curved Membranes and Membrane Fusion Processes Studied by Synchrotron X-ray-Scattering Techniques*. Advances in Planar Lipid Bilayers and Liposomes. Elsevier B.V. 2013, 17, pp.29-54.
164. Seddon, J.M. Structure of the inverted hexagonal (HII) phase, and non-lamellar phase transitions of lipids. *Biochim.Biophys.Acta.* 1990, **1031**(1), pp.1-69.
165. Rappolt, M., Hodzic, A., Sartori, B., Ollivon, M. and Laggner, P. Conformational and hydrational properties during the L(beta)- to L(alpha)- and L alpha- to H(II)-phase transition in phosphatidylethanolamine. *Chemistry and Physics of Lipids.* 2008, **154**(1), pp.46-55.
166. Van Venetie, R. and Verkleij, A.J. Analysis of the hexagonal II phase and its relations to lipidic particles and the lamellar phase: A freeze-fracture study. *BBA - Biomembranes.* 1981, **645**(2), pp.262-269.
167. Siegel, D.P. Inverted micellar intermediates and the transitions between lamellar, cubic, and inverted hexagonal lipid phases. *Biophys.J.* 1986, **49**, pp.1155-1170.
168. Veranic, P., Lokar, M., Schütz, G.J., Weghuber, J., Wieser, S., Hägerstrand, H., Kralj-Iglic, V. and Iglic, A. Different types of cell-to-cell connections mediated by nanotubular structures. *Biophysical Journal.* 2008, **95**(9), pp.4416-4425.
169. Dong, Y.D., Tilley, A.J., Larson, I., Jayne Lawrence, M., Amenitsch, H., Rappolt, M., Hanley, T. and Boyd, B.J. Nonequilibrium effects in self-assembled mesophase materials: Unexpected supercooling effects for cubosomes and hexosomes. *Langmuir.* 2010, **26**(11), pp.9000-9010.

170. Yaghmur, A., Laggner, P., Sartori, B. and Rappolt, M. Calcium triggered Lα-H2 phase transition monitored by combined rapid mixing and time-resolved synchrotron SAXS. *PLoS ONE.* 2008, **3**(4).
171. Yaghmur, A., Laggner, P., Zhang, S. and Rappolt, M. Tuning curvature and stability of monoolein bilayers by designer lipid-like peptide surfactants. *PLoS ONE.* 2007, **2**(5).
172. Shearman, G.C., Tyler, A.I.I., Brooks, N.J., Templer, R.H., Ces, O., Law, R.V. and Seddon, J.M. Ordered micellar and inverse micellar lyotropic phases. *Liquid Crystals.* 2010, **37**(6-7), pp.679-694.
173. Fong, W.K., Sánchez-Ferrer, A., Rappolt, M., Boyd, B.J. and Mezzenga, R. Structural Transformation in Vesicles upon Hydrolysis of Phosphatidylethanolamine and Phosphatidylcholine with Phospholipase C. *Langmuir.* 2019, **35**(46), pp.14949-14958.
174. Hickel, A., Danner-Pongratz, S., Amenitsch, H., Degovics, G., Rappolt, M., Lohner, K. and Pabst, G. Influence of antimicrobial peptides on the formation of nonlamellar lipid mesophases. *Biochimica et Biophysica Acta - Biomembranes.* 2008, **1778**(10), pp.2325-2333.
175. Kollmitzer, B., Heftberger, P., Rappolt, M. and Pabst, G. Monolayer spontaneous curvature of raft-forming membrane lipids. *Soft Matter.* 2013, **9**(45), pp.10877-10884.
176. Frewein, M.P.K., Rumetshofer, M. and Pabst, G. Global small-angle scattering data analysis of inverted hexagonal phases. *Journal of Applied Crystallography.* 2019, **52**(2), pp.403-414.
177. Harper, P.E. and Gruner, S.M. Electron density modeling and reconstruction of infinite periodic minimal surfaces (IPMS) based phases in lipid-water systems. I. Modeling IPMS-based phases. *Eur.Phys.J.E.* 2000, **2**, pp.217-228.
178. Tate, M.W. and Gruner, S.M. Temperature dependence of the structural dimensions of the inverted hexagonal (HII) phase of phosphatidylethanolamine-containing membranes. *Biochemistry.* 1989, **28**, pp.4245-4253.
179. Perutkova, S., Daniel, M., Rappolt, M., Pabst, G., Dolinar, G., Kralj-Iglic, V. and Iglic, A. Elastic deformations in hexagonal phases studied by small-angle X-ray diffraction and simulations. *Phys.Chem.Chem.Phys.* 2011, **13**, pp.3100-3107.
180. Rappolt, M., Cacho-Nerin, F., Morello, C. and Yaghmur, A. How the chain configuration governs the packing of inverted micelles in the cubic Fd3m-phase. *Soft Matter.* 2013, **9**(27), pp.6291-6300.
181. Kozlov, M.M., Leikin, S. and Rand, R.P. Bending, hydration and interstitial energies quantitatively account for the hexagonal-lamellar-hexagonal reentrant phase transition in dioleoylphosphatidylethanolamine. *Biophys.J.* 1994, **67**(4), pp.1603-1611.
182. Duesing, P.M., Templer, R.H. and Seddon, J.M. Quantifying packing frustration energy in inverse lyotropic mesophases. *Langmuir.* 1997, **13**(2), pp.351-359.
183. Shearman, G.C., Ces, O. and Templer, R.H. Towards an understanding of phase transitions between inverse bicontinuous cubic lyotropic liquid crystalline phases. *Soft Matter.* 2010, **6**(2), pp.256-262.
184. Mareš, T., Daniel, M., Perutkova, Š., Perne, A., Dolinar, G., Iglič, A., Rappolt, M. and Kralj-Iglič, V. Role of phospholipid asymmetry in the stability of

inverted haxagonal mesoscopic phases. *Journal of Physical Chemistry B.* 2008, **112**(51), pp.16575-16584.

185. Perutková, A., Daniel, M., Rappolt, M., Pabst, G., Dolinar, G., Kralj-Igli, V. and Igli, A. Elastic deformations in hexagonal phases studied by small-angle X-ray diffraction and simulations. *Physical Chemistry Chemical Physics.* 2011, **13**(8), pp.3100-3107.
186. Yaghmur, A., Kriechbaum, M., Amenitsch, H., Steinhart, M., Laggner, P. and Rappolt, M. Effects of pressure and temperature on the self-assembled fully hydrated nanostructures of monoolein-oil systems. *Langmuir.* 2010, **26**(2), pp.1177-1185.
187. Turner, D.C., Huang, J.S. and Gruner, S.M. Distribution of Decane within the Unit Cell of the Inverted Hexagonal (HII) Phase of Lipid-Water-Decane Systems Determined by Neutron Diffraction. *Biochemistry.* 1992, **31**(5), pp.1356-1363.
188. Harper, P.E., Cavazos, A.T., Kinnun, J.J., Petrache, H.I. and Wassall, S.R. Vitamin E Promotes the Inverse Hexagonal Phase via a Novel Mechanism: Implications for Antioxidant Role. *Langmuir.* 2020, **36**(18), pp.4908-4916.
189. Amenitsch, H., Bernstorff, S., Kriechbaum, M., Lombardo, D., Mio, H., Pabst, G., Rappolt, M. and Laggner, P. The small-angle X-ray scattering beamline at ELETTRA: A new powerful station for fast structural investigations on complex fluids with synchrotron radiation. *Il Nuovo Cimento D.* 1998, **20**, p.9.
190. Bernstorff, S., Amenitsch, H. and Laggner, P. High-throughput asymmetric double-crystal monochromator of the SAXS beamline at ELETTRA. *Journal of Synchrotron Radiation.* 1998, **5**, pp.1215-1221.
191. Petrascu, A.M., Koch, M.H.J. and Gabriel, A. A beginners' guide to gas-filled proportional detectors with delay line readout. *Journal of Macromolecular Science-Physics.* 1998, **B37**(4), pp.463-483.
192. Huang, T.C., Toraya, H., Blanton, T.N. and Wu, Y. X-ray powder diffraction analysis of silver behenate, a possible low-angle diffraction standard. *Journal of Applied Crystallography.* 1993, **26**, pp.180-184.
193. Tenchov, B., Rappolt, M., Koynova, R. and Rapp, G. New phases induced by sucrose in saturated phosphatidylethanolamines: An expanded lamellar gel phase and a cubic phase. *Biochimica et Biophysica Acta - Biomembranes.* 1996, **1285**(1), pp.109-122.
194. Zhang, R.T., Suter, R.M. and Nagle, J.F. Theory of the structure factor of lipid bilayers. *Physical Review E.* 1994, **50**(6), pp.5047-5060.
195. *Planar Confined Water Organisation in Lipid Bilayer Stacks of Phosphatidylcholine and Phosphatidylethanolamine.* [Online database]. ChemRxiv, 2023.
196. Yamada, T., Takahashi, N., Tominaga, T., Takata, S.-i. and Seto, H. Dynamical Behavior of Hydration Water Molecules between Phospholipid Membranes. *The Journal of Physical Chemistry B.* 2017, **121**(35), pp.8322-8329.
197. McIntosh, T.J. and Simon, S.A. Hydration and steric pressures between phospholipid bilayers. *Annu.Rev.Biophys.Biomol.Struct.* 1994, **23**, pp.27-51.
198. Marra, J. and Israelachvili, J. Direct measurements of forces between phosphatidylcholine and phosphatidylethanolamine bilayers in aqueous electrolyte solutions. *Biochemistry.* 1985, **24**(17), pp.4608-4618.

199. Parsegian, V.A. and Rand, R.P. Interaction in Membrane Assemblies. In: Lipowsky, R. and Sackmann, E. eds. *Structure and Dynamics of Membranes*. Amsterdam: North-Holland, 1995, pp.643-690.
200. Parsegian, V.A., Rand, R.P., Fuller, N.L. and Rau, D.C. Osmotic stress for the direct measurement of intermolecular forces. *Methods Enzymol.* 1986, **127**, pp.400-416.
201. Petrache, H.I., Tristram-Nagle, S., Harries, D., Kucerka, N., Nagle, J.F. and Parsegian, V.A. Swelling of phospholipids by monovalent salt. *Journal Of Lipid Research.* 2006, **47**(2), pp.302-309.
202. Petrache, H.I., Zemb, T., Belloni, L. and Parsegian, V.A. Salt screening and specific ion adsorption determine neutral-lipid membrane interactions. *Proceedings Of The National Academy Of Sciences Of The United States Of America.* 2006, **103**(21), pp.7982-7987.
203. Pabst, G., Hodzic, A., S¦îtrancar, J., Danner, S., Rappolt, M. and Laggner, P. Rigidification of neutral lipid bilayers in the presence of salts. *Biophys.J.* 2007, **93**(8), pp.2688-2696.
204. Krzywoszyńska, K., Witkowska, D., Świątek-Kozłowska, J., Szebesczyk, A. and Kozłowski, H. General Aspects of Metal Ions as Signaling Agents in Health and Disease. *Biomolecules.* 2020, **10**(10), p.1417.
205. Lucy, J.A. Calcium Ions, Enzymes, and Cell Fusion. In: Martonosi, A.N. ed. *The Enzymes of Biological Membranes: Volume 1 Membrane Structure and Dynamics*. Boston, MA: Springer US, 1985, pp.371-391.
206. Williams, R.J.P. Cation and Proton Interactions with Proteins and Membranes. *Biochemical Society Transactions.* 1979, **7**, pp.481-509.
207. Kang, B.B., Tang, H.C., Zhao, Z.D. and Song, S.S. Hofmeister Series: Insights of Ion Specificity from Amphiphilic Assembly and Interface Property. *ACS OMEGA.* 2020, **5**(12), pp.6229-6239.
208. Hofmeister, F. Zur Lehre von der Wirkung der Salze. *Archiv für experimentelle Pathologie und Pharmakologie.* 1888, **24**(4), pp.247-260.
209. Zhang, Y. and Cremer, P.S. Interactions between macromolecules and ions: the Hofmeister series. *Current Opinion in Chemical Biology.* 2006, **10**(6), pp.658-663.
210. Sanderson, P.W., Lis, L.J., Quinn, P.J. and Williams, W.P. The Hofmeister effect in relation to membrane lipid phase stability. *Biochimica et Biophysica Acta (BBA) - Biomembranes.* 1991, **1067**(1), pp.43-50.
211. Rodriguez, J.R. and García, A.E. Concentration dependence of NaCl ion distributions around DPPC lipid bilayers. *Interdisciplinary Sciences: Computational Life Sciences.* 2011, **3**(4), pp.272-282.
212. Aroti, A., Leontidis, E., Dubois, M. and Zemb, T. Effects of Monovalent Anions of the Hofmeister Series on DPPC Lipid Bilayers Part I: Swelling and In-Plane Equations of State. *Biophysical Journal.* 2007, **93**(5), pp.1580-1590.
213. Vácha, R., Jurkiewicz, P., Petrov, M., Berkowitz, M.L., Böckmann, R.A., Barucha-Kraszewska, J., Hof, M. and Jungwirth, P. Mechanism of Interaction of Monovalent Ions with Phosphatidylcholine Lipid Membranes. *The Journal of Physical Chemistry B.* 2010, **114**(29), pp.9504-9509.
214. Vácha, R., Jurkiewicz, P., Petrov, M., Berkowitz, M.L., Böckmann, R.A., Barucha-Kraszewska, J., Hof, M. and Jungwirth, P. Mechanism of interaction

of monovalent ions with phosphatidylcholine lipid membranes. *Journal Of Physical Chemistry B.* 2010, **114**(29), pp.9504-9509.

215. Alsop, R.J., Maria Schober, R. and Rheinstädter, M.C. Swelling of phospholipid membranes by divalent metal ions depends on the location of the ions in the bilayers. *Soft Matter.* 2016, **12**(32), pp.6737-6748.
216. Zhong, C., Deng, Y., Hu, W., Qiao, J., Zhang, L. and Zhang, J. A review of electrolyte materials and compositions for electrochemical supercapacitors. *Chemical Society Reviews.* 2015, **44**(21), pp.7484-7539.
217. Friedman, R. Membrane–Ion Interactions. *The Journal of Membrane Biology.* 2018, **251**(3), pp.453-460.
218. Choi, D.-H., Son, H., Jeong, J.-Y. and Park, G.-S. Correlation between salt-induced change in water structure and lipid structure of multi-lamellar vesicles observed by terahertz time-domain spectroscopy. *Chemical Physics Letters.* 2016, **659**, pp.164-168.
219. Korreman, S.S. and Posselt, D. Modification of anomalous swelling in multilamellar vesicles induced by alkali halide salts. *Eur.Biophys.J.* 2001, **30**(2), pp.121-128.
220. Rappolt, M., Pabst, G., Amenitsch, H. and Laggner, P. Salt-induced phase separation in the liquid crystalline phase of phosphatidylcholines. *Colloids and Surfaces A: Physicochemical and Engineering Aspects.* 2001, **183-185**, pp.171-181.
221. Rappolt, M., Pressl, K., Pabst, G. and Laggner, P. L(α)-phase separation in phosphatidylcholine-water systems induced by alkali chlorides. *Biochimica et Biophysica Acta - Biomembranes.* 1998, **1372**(2), pp.389-393.
222. Sharma, V.K. and Mamontov, E. Reduction of nanoscopic dynamics in the zwitterionic membrane by salt. *Journal of Applied Physics.* 2022, **132**(7).
223. Kurakin, S., Ivankov, O., Skoi, V., Kuklin, A., Uhríková, D. and Kučerka, N. Cations Do Not Alter the Membrane Structure of POPC—A Lipid With an Intermediate Area. *Frontiers in Molecular Biosciences.* 2022, **9**.
224. Papahadjopoulos, D., Jacobson, K., Nir, S. and Isac, T. Phase transitions in phospholipid vesicles. Fluorescence polarization and permeability measurements concerning the effect of temperature and cholesterol. *Biochim.Biophys.Acta.* 1973, **311**(3), pp.330-348.
225. Hishida, M. and Seto, H. Lamellar-lamellar phase separation of phospholipid bilayers induced by salting-in/-out effects. *Journal of Physics: Conference Series.* 2011, **272**(1), p.012008.
226. Lis, L.J., Lis, W.T., Parsegian, V.A. and Rand, R.P. Adsorption of Divalent Cations to a Variety of Phosphatidylcholine Bilayers. *Biochemistry.* 1981, **20**(7), pp.1771-1777.
227. Lis, L.J., Rand, R.P. and Parsegian, V.A. Measurement of the Adsorption of Ca2+ and Mg2+ to Phosphatidyl Choline Bilayers. In: Blank, M. ed. *Bioelectrochemistry: Ions, Surfaces, Membranes*. Washington: ACS Publications, 1980, p.527.
228. Cordomí, A., Edholm, O. and Perez, J.J. Effect of ions on a dipalmitoyl phosphatidylcholine bilayer. A molecular dynamics simulation study. *Journal Of Physical Chemistry B.* 2008, **112**(5), pp.1397-1408.

229. Das, G., Hlushak, S., dos Ramos, M.C. and McCabe, C. Predicting the thermodynamic properties and dielectric behavior of electrolyte solutions using the SAFT-VR+DE equation of state. *Aiche Journal.* 2015, **61**(9), pp.3053-3072.
230. Subramaniam, R., Lynch, S., Cen, Y. and Balaz, S. Polarity of hydrated phosphatidylcholine headgroups. *Langmuir.* 2019, **35**(25), pp.8460-8471.
231. Tatulian, S.A. Binding of alkaline-earth metal cations and some anions to hosphatidylcholine liposomes. *European Journal of Biochemistry.* 1987, **170**(1-2), pp.413-420.
232. Oshima, H., Inoko, Y. and Mitsui, T. Hamaker constant and binding constants of Ca2+ and Mg2+ in dipalmitoyl phosphatidylcholine/water system. *Journal Of Colloid And Interface Science.* 1982, **86**(1), pp.57-72.
233. Yamada, N.L., Seto, H., Takeda, T., Nagao, M., Kawabata, Y. and Inoue, K. SAXS, SANS and NSE studies on "unbound state" in DPPC/water/CaCl2 system. *Journal of the Physical Society of Japan.* 2005, **74**(10), pp.2853-2859.
234. Rappolt, M., Vidal, M.F., Kriechbaum, M., Steinhart, M., Amenitsch, H., Bernstorff, S. and Laggner, P. Structural, dynamic and mechanical properties of POPC at low cholesterol concentration studied in pressure/temperature space. *European Biophysics Journal with Biophysics Letters.* 2003, **31**(8), pp.575-585.
235. Klasczyk, B., Knecht, V., Lipowsky, R. and Dimova, R. Interactions of alkali metal chlorides with phosphatidylcholine vesicles. *Langmuir.* 2010, **26**(24), pp.18951-18958.
236. Philipp, J., Dabkowska, A., Reiser, A., Frank, K., Krzysztoń, R., Brummer, C., Nickel, B., Blanchet, C.E., Sudarsan, A., Ibrahim, M., Johansson, S., Skantze, P., Skantze, U., Östman, S., Johansson, M., Henderson, N., Elvevold, K., Smedsrød, B., Schwierz, N., Lindfors, L. and Rädler, J.O. pH-dependent structural transitions in cationic ionizable lipid mesophases are critical for lipid nanoparticle function. *Proceedings of the National Academy of Sciences.* 2023, **120**(50), p.e2310491120.
237. Garcia-Celma, J.J., Hatahet, L., Kunz, W. and Fendler, K. Specific anion and cation binding to lipid membranes investigated on a solid supported membrane. *Langmuir.* 2007, **23**(20), pp.10074-10080.
238. Kodama, M., Inoue, H. and Tsuchida, Y. The behavior of water molecules associated with structural changes in phosphatidylethanolamine assembly as studied by DSC. *Thermochimica Acta.* 1995, **266**, pp.373-384.
239. Bronshteyn, V.L. and Steponkus, P.L. Calorimetric studies of freeze-induced dehydration of phospholipids. *Biophys J.* 1993, **65**(5), pp.1853-1865.
240. Grabielle-Madelmont, C. and Perron, R. Calorimetric studies on phospholipid—water systems: II. Study of water behavior. *Journal of Colloid and Interface Science.* 1983, **95**(2), pp.483-493.
241. Mariani, P., Luzzati, V. and Delacroix, H. Cubic phases of lipid-containing systems. Structure analysis and biological implications. *J.Mol.Biol.* 1988, **204**(1), pp.165-189.